NASA CONTRACTOR REPORT

NASA CR-2094

METEOROLOGICAL AND ECOLOGICAL MONITORING OF THE STRATOSPHERE AND MESOSPHERE

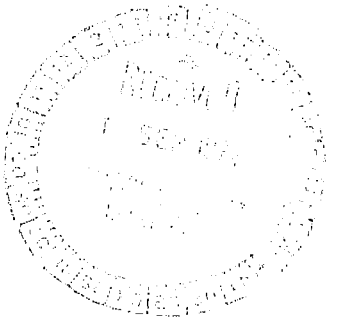

by Reginald E. Newell and Carlton R. Gray

Prepared by
MASSACHUSETTS INSTITUTE OF TECHNOLOGY
Cambridge, Mass. 02139
for Langley Research Center

NATIONAL AERONAUTICS AND SPACE ADMINISTRATION • WASHINGTON, D. C. • AUGUST 1972

1. Report No.	2. Government Accession No.	3. Recipient's Catalog No.
NASA CR-2094		

4. Title and Subtitle	5. Report Date
METEOROLOGICAL AND ECOLOGICAL MONITORING OF THE STRATOSPHERE AND MESOSPHERE	August 1972
	6. Performing Organization Code: DSR 72514
7. Author(s): Reginald E. Newell and Carlton R. Gray	8. Performing Organization Report No.: AER 12-F
	10. Work Unit No.
9. Performing Organization Name and Address: Massachusetts Institute of Technology, Cambridge, Mass. 02139	11. Contract or Grant No.: NAS1-9884
	13. Type of Report and Period Covered: Contractor Report
12. Sponsoring Agency Name and Address: National Aeronautics and Space Administration, Washington, D.C. 20546	14. Sponsoring Agency Code

15. Supplementary Notes M.I.T. aeronomy personnel participating in the preparation and documentation of this Interim Final Report: Prof. Reginald E. Newell, Principal Investigator; Carlton R. Gray, Director; Dr. Derek M. Cunnold; Harvey L. Malchow; Dr. Terrence P. McGarty; Dennis C. Merritt; Joseph E. Salah; Katherine L. Tompkins; Robert E. Var; Peter C. Vernam; Dr. Cynthia K. Whitney; Dr. Mao-Fou Wu.

16. Abstract

A concept for determining the constituent densities of ozone, atomic oxygen, aerosols, and neutral density in the 20 to 100 km region of the atmosphere from a satellite was developed. The concept includes the daytime measurement of solar scattering at the earth's limb in selected narrow spectral bands of the ultraviolet and visible regions, and the measurement of selected (dayglow) emissions. Nighttime measurements of the atmospheric extinction of stellar energy in selected bands are also considered as are simultaneous measurements of the 5577 Å airglow and molecular oxygen emissions in the Herzberg band. Radiative-transfer models and recursive inversion algorithms are developed for the measurements, and the accuracy of the concept is assessed.

17. Key Words (Suggested by Author(s))	18. Distribution Statement
Ozone, Atomic Oxygen, Aerosols, Scattering, Remote Sensing, Ultraviolet, Occultation, Horizon Inversion	Unclassified - Unlimited

19. Security Classif. (of this report)	20. Security Classif. (of this page)	21. No. of Pages	22. Price*
Unclassified	Unclassified	165	$3.00

*For sale by the National Technical Information Service, Springfield, Virginia 22151

Table of Contents

Meteorological and Ecological Monitoring of the Stratosphere and Mesosphere

by

Prof. Reginald E. Newell, Department of Meteorology
Carlton R. Gray, Charles Stark Draper Laboratory
MIT Aeronomy Program

1.0 BACKGROUND

To place the MIT Aeronomy Program in historical perspective, it is necessary to go back fifty years. In 1921, Lindemann and Dobson observed that meteors became incandescent and burned up in the atmosphere at altitudes different from those expected on the basis of theory and an assumed standard-temperature profile, then taken as 220°K above the tropopause. They suggested that their observations implied a much higher temperature in the vicinity of 50 km than previously assumed, and, in addition, they suggested a mechanism for maintaining such a temperature profile through the absorption of solar ultraviolet radiation and the subsequent reemission of infrared radiation by ozone. Their estimate of a temperature of 280°K at 60 km is remarkably close to the stratopause temperature given by current measurements.

Since this pioneering work, impressive progress has been made in understanding the role of ozone in upper-atmospheric processes. Dobson and his colleagues at Oxford went on to develop techniques to measure the total ozone in a column and studied its daily and seasonal variation throughout the world. Since 1957, the development by Brewer and Regener of ozone-measuring devices which could be flown on balloons has given a picture of the vertical distribution of ozone up to 25-30 km. Recently, satellite measurements reported by Prabhakara have yielded information about total ozone amounts on a global basis (see Conrath et al, 1970).

Above 30 km, our understanding of the temperature, density, and velocity structure of the region has also been greatly extended since Lindemann and Dobson's 1921 report. Their results led Whipple to write a one-page letter to Nature suggesting that anomalous-sound propagation might represent sound waves sent back to earth in the warm region near 50 km. Whipple also suggested that Professor Goddard's rockets could be used to send up small explosive charges so that sound waves observed at the ground could give information on the wind and temperature structure aloft. This is now a standard technique used by NASA for measurement in the 30-80 km region.

The measurements of the atmospheric structure above 30 km, mainly by rocket soundings, have revealed the overall pattern in terms of winds, temperature and densities and has allowed the construction of "standard atmospheres" for the region. The expense and difficulty of rocket measurements

—together with the restricted latitudinal and longitudinal applicability of the results—nevertheless leave much to be desired.

Observation of the basic structure of the atmosphere has been accompanied by an improved understanding of the physical processes which occur there. The photochemical theory of ozone formation first developed by Chapman in the early 1930's has been refined and extended by numerous workers. In 1958, Murgatroyd and Goody calculated the radiative-heating rates in the region assuming photochemical equilibrium concentrations of ozone. Figure 1-1—a heating profile for the equator—is based mainly on this work. As Dobson earlier suggested, ozone is of paramount importance in determining heating rates.

A further step in our understanding of the processes of this atmospheric region can be made in terms of the generation of available potential energy (Newell, 1963). Apparently, net radiative heating occurs where it is warm—the summer stratosphere; and net cooling occurs where it is cold—the winter polar stratosphere in the 30-50 km region. This configuration implies a generation of zonal available potential energy and suggests that energy to maintain the motion in this region is generated within the region. By contrast, the 50-80 km region has cooling in warm regions and heating in cold regions, indicating that available potential energy is destroyed. According to these calculations, therefore, the motions in this region must be maintained by energy transmitted from some other region. It should be remembered, however, that these conclusions, which are of a fundamental nature, depend on heating-rate computations which in turn are dependent upon an assumed—rather than measured—ozone distribution.

Apart from a handful of rocket flights, little is currently known about the distribution of ozone above 30 km. Even though 50 years have elapsed since its importance was first suggested by Lindemann and Dobson, ozone still remains to be adequately studied. It has become clear that dynamic interactions between different atmospheric levels will be critically important in any energy calculations, as shown theoretically by Charney and Drazin in 1961. Observational studies (Newell and Richards, 1969; Dopplick, 1971) give vertical energy flux values which are comparable to the estimates of generation in situ. Dopplick's results suggest that, on some occasions, energy is transferred into the lower stratosphere from above. The atmosphere apparently cannot easily be separated into regions which have little or no effect on one another. Our understanding of the interaction between various levels of the atmosphere is quite unsatisfactory at present.

Another item of unfinished business is our general understanding of stratospheric aerosols. The presence of aerosols which act to absorb and scatter solar radiation will affect the local temperature and hence the behavior of the atmosphere where they occur. We have at present only a very crude idea of the nature and distribution of aerosols.

In summary, there remain numerous terms in the momentum, heat and energy-balance equations which cannot be estimated with the data at hand. Delineation of global values of ozone density, as well as neutral density and

temperature, atomic oxygen, and aerosol concentration, would be an important step in refining available values and in estimating those as yet unknown.

In 1964 the National Academy of Sciences/National Research Council (NAS/NRC) convened a panel on ozone which recommended more observations and research (Atmospheric Ozone Studies, An Outline for an International Observations Program, Pub. 1348, 1966). Extracts from the conclusions follow:

> The primary focal point for extended observations and research in atmospheric ozone, requiring worldwide cooperation and planning, involves the study of its formation in the stratosphere, transport downward to the troposphere, and ultimate destruction at the earth's surface. Also requiring careful consideration are studies of the physical processes (including photochemistry) in the stratosphere and mesosphere involving interactions with the dynamics of this region of the atmosphere, and those involving possible upper-atmosphere reactions to anomalous solar radiation.
>
> The most likely techniques for continuous ozone measurements, particularly above 30 km, would probably involve satellite observations. However, until satellite ozone observations can be made routinely, it is necessary that a program of rocket ozone observations (optical and/or dropsondes) be carefully planned.

The problem of ozone is no less pressing now than when this NAS/NRC report was written. In fact, there are under current debate several suggestions about possible man-made modifications of the earth's ozone layer—with vital ramifications for life on earth. Chemists (Johnston, 1971) have suggested that when the oxides of nitrogen are introduced directly into the stratosphere by the SST aircraft, the ozone will be depleted. This is but the most recent case in which it would be valuable to say that we had already measured and understood the global ozone distribution.

Lest it be felt that prejudice governs our arguments in favor of a more precise observational look at the region above 30 km, we quote below from the Federal Plan for Upper Air Observations above 30 Kilometers, U.S. Department of Commerce, Washington, D. C., OFCM 69-7, July 1969:

OPERATIONAL AND RESEARCH NEEDS

Federal Needs

> "Agency needs for meteorological information above 30 km are synthesized into a set of three Federal needs as follows:
>
> • Establishment of an observational program (above 30 km).
>
> To gain in support of research, a better understanding and description of the circulation, heating, density, and ozone patterns in the upper atmosphere and their interactions with the lower atmospheric processes.

To provide a climatology of the upper atmosphere.

To provide a data base for developing and verifying forecasting techniques.

- Provision of special observations of wind, temperature, and density (or pressure) above 30 km from a certain selected station (or set of stations) for mission support of missile and aerospace systems.

  To define the normal or standard condition of the atmosphere and the variations from this standard for planning, designing, test scheduling, and routine operations.

  To provide data to engineers for analysis of atmospheric influences on a system being tested.

- Establishment of an operational global forecasting service for wind, temperature, and density (or pressure) above 30 km."

Discussions between groups at the MIT Draper Laboratory and Department of Meteorology concerning the possibilities of measuring the basic parameters of the upper atmosphere from a satellite began in February 1966. Scientists at the Draper Laboratory had developed limb-scanning techniques for navigation purposes in the Apollo program. The possibilities of using these techniques for meteorological measurements looked promising (Wolff, 1967), and the necessary apparatus for a pilot model was actually being flown up to 82 km on the X-15-1 aircraft (Gray, 1969).

The MIT Aeronomy Program was conceived to supply the information required for a fuller understanding of atmospheric structure and energetics. It is a comprehensive experiment which has been designed to include the important aspects of the energy budget in the observational plan, rather than be caught later with an unmonitored prime variable. In the long run, this seems the most efficient and most economical approach, and it certainly assists interpretation. The horizon-inversion instrument (a single-line-of-sight design) remains the same no matter what is being observed—ozone, neutral atmospheric density, aerosols and airglow emissions. The MIT Aeronomy concept of horizon inversion is an adaptation of Dobson's use of ultraviolet wavelengths, long paths and differential absorption as the most promising technique, differing only in using the tangent ray, rather than the zenith ray. As noted, we had also worried, as has Dobson over the years, about the effects of aerosols. Recently, however, it has been determined that the global distribution of stratospheric aerosols can be measured, in addition to other constituents, thus establishing a baseline against which to compare further ecological measurements. Our technique may therefore be amenable to the solution of certain problems of the upper troposphere and lower stratosphere.

A joint proposal to measure these parameters was prepared and informal approaches were made to various agencies in the summer of 1967. A formal proposal for space on NIMBUS E was submitted to NASA in February 1968 and resubmitted for NIMBUS F review in November 1968. In November 1969,

we were notified that the proposal would be funded under NASA's Advanced Applications Flight Experiments program (AAFE), and a team was assembled. Work commenced in June 1970 and a review of the contractual activities is recorded herein.

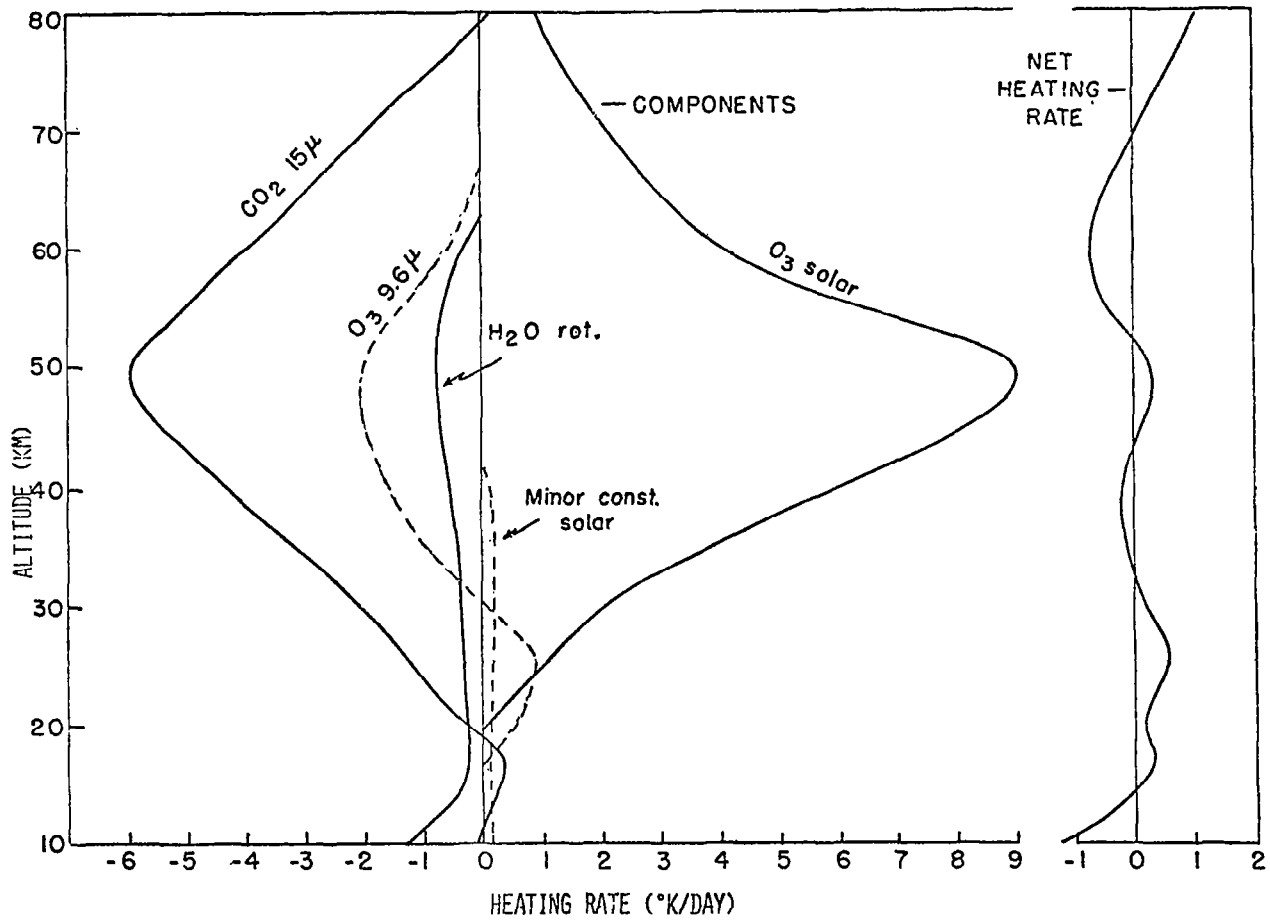

Fig. 1-1 Theoretical Heating Rates (°K/day) at the Equator.

References for Section 1.0

Brewer, A. W., and Milford, J. R., 1960: The Ozone-Kew Ozone Sonde. Proceedings of the Royal Society, Ser. A, 256, 470-495.

Charney, J. G., and Drazin, P. G., 1961: Propagation of Planetary-scale Disturbances from the Lower into the Upper Atmosphere. J. Geophys. Res., 66, 83-110.

Conrath, B. J., Hanel, R. A., Kunde, V. G., and Prabhakara, C., 1970: The Infrared Interferometer Experiment on Nimbus 3. J. Geophys. Res., 75, 5831-5857.

Dopplick, T. G., 1971: The Energetics of the Lower Stratosphere Including Radiative Effects. Quarterly J. R. Meteorological Society, 97, 209-237.

Gray, C. R., 1969: MIT/IL X-15 Horizon Definition Experiment Final Report. Apollo Guidance and Navigation, MIT Instrumentation Laboratory, R-648.

Johnston, H. F., Destruction of Stratospheric Ozone by Nitrogen Oxide Catalysts from SST Exhaust, Science, 173, 517-522, 1971.

Lindemann, F. A., and Dobson, G. M. B., 1921: A Theory of Meteors, and the Density and Temperature of the Outer Atmosphere to which it Leads. Proceedings of the Royal Society, Ser. A 102, 411-437.

Murgatroyd, R. J., and Goody, R. M., 1958: Sources and Sinks of Radiative Energy from 30 to 90 km. Quart. J. R. Meteor. Soc., 84, 87, 125-135.

Newell, R. E., 1963: Preliminary Study of Quasi-Horizontal Eddy Fluxes from Meteorological Rocket Network Data. J. Atmos. Sci., 20, 213-235.

Newell, R. E., and Richards, M. E., 1969: Energy Flux and Convergence Patterns in the Lower and Middle Stratosphere During The IQSY. Quarterly Journal of the Royal Meteorological Society, Vol. 95, No. 404, 310-328.

Regener, V., 1960: On a Sensitive Method for the Recording of Atmospheric Ozone. J. Geophys. Res., 65, 3975-3977.

Whipple, F. J. W., 1923: The High Temperature of the Upper Atmosphere as an Explanation of Zones of Audibility. Nature, Vol. III, No. 2780, 187.

Wolff, M., 1967: Precision Limb Profiles for Navigation and Research. Journal of Spacecraft and Rockets, Vol. 4, No. 8, 978-983.

2.0 AERONOMY REVIEW

2.1 TECHNICAL OVERVIEW

Goals: A comprehensive and systematic examination of the 20-100 km region of the atmosphere is the expressed purpose of the MIT Aeronomy Experiment. From the feasibility studies, it has been demonstrated that constituent densities of neutral atmospheric density, aerosol, ozone, atomic oxygen and nitric oxide can be determined from observations of scattered sunlight, stellar occultation, and airglow emissions. The principal advantage of the horizon inversion technique is that accurate altitude profiles of several atmospheric constituents can be obtained simultaneously over a substantial range of altitudes from a satellite-mounted single line-of-sight multispectral analyzer and star tracker, aligned in the direction of the earth's horizon. From this satellite configuration, complete global coverage can be obtained as the instrument sequentially scans a range of tangent altitudes. Each of the atmospheric constituents to be measured possesses important absorption, scattering or emission characteristics in the ultraviolet or visible region of the spectrum. By the appropriate choice of wavelengths, we can obtain vertical profiles of the atmospheric constituents with an altitude resolution of approximately 1 km.

Importance: The discussion in the background section emphasizes attempts to understand the atmospheric energy budget and, in addition, stresses the importance of systematic observations of atmospheric temperature and ozone. Global distributions of temperature and density will serve as inputs for studying the role of dynamics in the energy balance, and will aid in better understanding of atmospheric processes.

Aerosols are important in the atmospheric energy budget, since they contribute directly to temperature changes both in the stratosphere and at the earth's surface. Of particular interest is the vertical distribution of aerosols as an environmental pollutant of the stratosphere and mesosphere. Aerosols (which are both man-made and natural) contribute directly to temperature change in this region by direct absorption of solar radiation. Changes in the concentrations of stratospheric and mesospheric aerosols also produce changes in the atmospheric transmission; thus, surface temperature changes are possible. Therefore, monitoring aerosol distribution provides further understanding of the stratospheric and mesospheric energy budgets and establishes base-line environmental-pollution measurements.

Ozone is of great practical importance, not only because of the role it plays in the atmospheric energy budget and because it protects mankind from harmful ultraviolet radiation, but also because of its role in atmospheric dynamics. Adequate theoretical description of the upward propagation of planetary waves, the behavior of stratospheric circumpolar-wind systems and the generation of atmospheric tides by solar energy depends upon a knowledge of ozone distribution. Ozone interacts strongly with other minor atmospheric constituents and is of importance, for example, in understanding the ionospheric D-region (between 70 and 100 km). These effects are related not only to the total-ozone concentration in a vertical column of given cross section, but to

the detailed structure of the ozone concentration profile, as well. While observations of the total ozone concentration may be obtained by simple techniques (such as those of Dobson), observations of the altitude profiles may only be obtained by techniques such as ours.

Atomic oxygen is another very important constituent at higher levels of the atmosphere. It is possible that atomic oxygen contributes significantly to the energy budget of the 90-km region and hence may be a significant factor in the circulation patterns of the upper atmosphere. Atomic oxygen is an extremely important constituent of the ionosphere and is the major contributor to atmospheric density between altitudes of 200 and 700 km. The atomic-oxygen concentration at these high altitudes is controlled by the atmospheric temperature distribution and by the atomic-oxygen concentration at the 100-km level. It has been suggested that certain variations occurring in the ionospheric F-region (above 150 km) are produced by changes in the atomic-oxygen-to-molecular-nitrogen ratio at the 100-km level (Wu and Newell, 1971; Chandra et al., 1971). Atomic oxygen is also important in the E-region (roughly 100 to 150 km) (Bowhill, 1969) and in the ionospheric D-region, where it affects the concentration of negative ions (Bowhill, 1969; Newell, 1968; Donahue, 1968).

We also plan to measure nitric oxide, another atmospheric constituent which is important for understanding the D-region. Recently it has been proposed that nitric oxide reacts with ozone and contributes to ozone loss in the stratosphere (e.g., Shimazaki and Laird, 1970). The reaction scheme is of particular current interest (Johnston, 1971) because of the possibility that additional nitric oxide may be introduced into the stratosphere by the SST aircraft.

The five atmospheric constituents discussed—neutral density, aerosols, ozone, atomic oxygen and nitric oxide—will all be monitored by the single line-of-sight instrument envisioned for use in the MIT Aeronomy Program.

References for Section 2.1

Bowhill, S. A., Ion Chemistry of the D- and E- regions—A Survey for Working Group 11 of the Inter-union Commission on Solar-Terrestrial Physics, J. Atmos. Terrest. Phys., 31, 731-742, 1969.

Chandra, S., E. J. Maier, B. E. Troy, Jr., and B. C. Narasinga Rao, Subauroral Red Arcs and Associated Ionospheric Phenomena, J. Geophys. Res., 76, 920-925, 1971.

Donahue, T. M., Ionospheric Composition and Reactions, Science, 159, 489-498, 1968.

Johnston, H. F., Destruction of Stratospheric Ozone by Nitrogen Oxide Catalysts from SST Exhaust, Science, 173, 517-522, 1971.

Newell, R. E., The General Circulation of the Atmosphere Above 60 km, Meteor. Monog., 9, 31, 98-113, 1968.

Shimazaki, T., and A. R. Laird, A Model Calculation of the Diurnal Variation in Minor Neutral Constituents in the Mesosphere and Lower Thermosphere Including Transport Effects, J. Geophys. Res., 75, 3221-3236, 1970.

Wu, M. F., and Newell, R. E., Computer Simulation of the F-Region Seasonal Anomaly, presented at COSPAR meeting on Theoretical Ionospheric Models, Penn. Univ., June, 1971.

2.2 TECHNIQUE AND GEOMETRY

The Aeronomy approach to monitoring atmospheric-constituent distributions in the 20-100 km altitude range is inversion of intensity measurements obtained from scattered sunlight, stellar occultation, and airglow emissions. In particular, the experimental configuration is as shown in Fig. 2.2-1. The satellite-based instrument obtains multispectral intensity measurements as a function of line-of-sight tangent altitude. For the case of scattered sunlight and airglow emissions, a mechanically controlled horizon scan is employed. For the stellar-occultation case, the star is physically tracked into the horizon and as it occults, the line-of-sight intensity is measured as a function of tangent altitude. In either case, multispectral horizon-intensity measurements are fed into a computerized inversion program which outputs the vertical distribution of the atmospheric constituents.

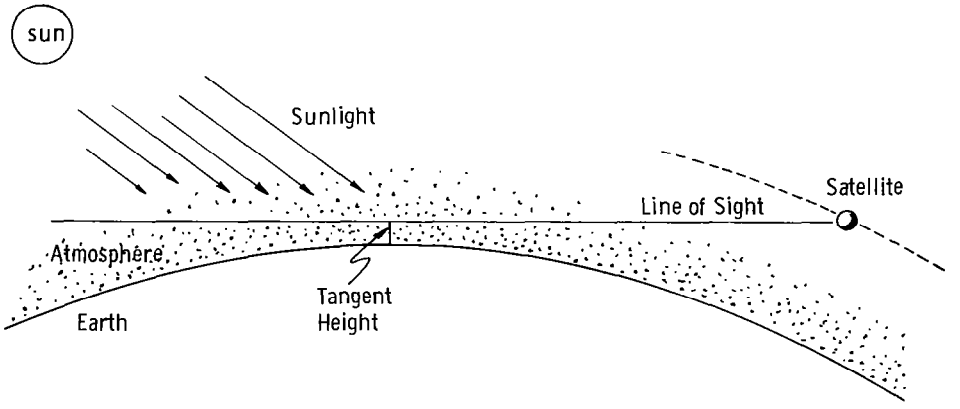

Figure 2.2-1 Scattered Sunlight Horizon Scanning Geometry

This horizon-inversion concept for obtaining the vertical distribution of the atmospheric constituents was chosen based on several considerations: Ground-based techniques are intrinsically insensitive to higher-altitude phenomena, due to the overwhelming interference of the intervening atmosphere. The need arose, therefore, for satellite-borne remote sensors. The earliest ones, such as those carried by the Nimbus satellites, were downward-looking. However, since all remote-sensing experiments have less spatial resolution along the line of sight than in the perpendicular direction, both ground-based vertical and satellite-based downward-looking experiments provide good horizontal resolution but relatively poor vertical resolution. This fact provided the impetus for the experimental configuration chosen here, in which the weakly-resolved direction is tangent to the earth and the strongly-resolved direction (perpendicular to the line of sight) is along a local vertical. Thus, the horizon-inversion concept provides a highly accurate—and at the same time systematic—technique for global monitoring of the vertical distributions of various atmospheric constituents.

Like any remote-sensing experiment, the horizon-inversion concept is not restricted to any particular wavelength region, and therefore the choice of wavelengths depends on the constituents of interest and their wavelength-dependent radiative-transfer properties. For example, wavelengths near the center of the strong absorption bands of ozone (2550 Å) are used to obtain the most accurate determination of the vertical distribution of ozone densities while aerosol extinction properties at 7000 Å provide excellent monitoring characteristics. Thus, in the visible and ultraviolet region of the electromagnetic spectrum, the contributions to the line-of-sight intensity by ozone and aerosols, as well as neutral atmospheric density, are significant, and therefore the experiment also provides significant information about these constituents. Thus, the Aeronomy Program serves more than just a narrow meteorological interest: its end objectives extend into the ecological realm as well. The only price paid for this additional information is the incorporation of selective filters within the detector's spectral response.

2.3 CONSTITUENT IDENTIFICATION

2.3.1 Constituents Derived from Scattered-Sunlight Technique

Altitude profiles of scattered sunlight will be used to obtain daytime vertical distributions of one of the primary atmospheric constituents—neutral atmospheric density. The neutral atmospheric densities thus obtained will be integrated to produce atmospheric temperature profiles on the basis of the hydrostatic equation. This conversion and the errors introduced by it are discussed in Cunnold, 1971. It should thus be possible to make atmospheric temperature measurements between 20 and 80 km to an accuracy of a few degrees K.

Meteorological rocket network (MRN) data obtained during the last decade have yielded considerable information on the density and temperature of the atmospheric region below 50 km. Measurements above this height have, however, been considerably more infrequent and have been obtained principally by NASA (Smith et al, 1960-1968). These measurements form the basis of the CIRA 1970 model of the 50-100 km region of the atmosphere (Groves, 1970). The latest available information on atmospheric density and temperature profiles at different latitudes and seasons may be found therein. Values for the standard deviation of temperature as a function of latitude and season may also be found in that reference (also see Cole, 1970). Several average profiles of neutral density and standard deviations are listed in Table 2.3-I. From our analysis it is felt that the tabulated standard deviations of neutral density are conservative estimates of the true values. The density is relatively seasonally invariant over the equator and, accordingly, only an annual average profile is tabulated for the tropics. Our calculations have shown that densities are correlated over a greater altitude range than are temperatures. For temperature, the correlation distance is roughly a scale height (approximately 7 km). An example of these correlations is shown in Fig. 2.3-1.

Early in our experiment, aerosols were viewed as an atmospheric constituent which—by virtue of scattering—would significantly affect our results, thus restricting our ability to determine neutral atmospheric density and ozone concentrations. Subsequent investigations have, however, demonstrated the importance of our technique in monitoring aerosol particle concentration. It is proposed that the contributions from Rayleigh scatterers and aerosols be separated by virtue of their different wavelengths and phase function dependence of their resultant scattering.

Data on aerosol particle concentrations (Section 3.7) are summarized in Salah, 1971. Few measurements have been made of concentrations above 30 km. A reference profile of the aerosol extinction coefficient as a function of altitude at 5500 Å is shown in Fig. 2.3-2. The extinction coefficient is defined to be the product of the particle concentration and the scattering cross section (integrated over all scattering angles). The scattering cross section possesses a strong wavelength dependence only if large aerosols (i.e., $\nu \sim 3$) such as occur in the stratosphere, are virtually absent (see Fig. 3.7-5). The aerosol concentrations above 35 km have been assumed to be such that the ratio of aerosols to air molecules remains constant above that height.

Scattered sunlight will be observed at wavelengths in the Hartley and Huggins absorption bands of ozone (2100-3400 Å). By using several wavelengths within these bands, altitude profiles of ozone concentration between 20 and 75 km may be derived. The latitudinal and longitudinal variability for three-month averages of the total ozone concentration is depicted in Figure 2.3-3. This variability is accounted for by dynamic processes below 30 km. Above that height, ozone is approximately in photochemical equilibrium, and variations should be relatively minor, although at very high altitudes a substantial diurnal variation is theoretically possible. The presently available limited number of profiles of ozone concentration above 30 km are depicted in Fig. 2.3-4, and based upon these data, we have tabulated an average ozone profile and the standard deviation of the observations in Table 2.3-II. Although one of the original purposes of the past year's investigation was to investigate the effect of dynamic processes on the high altitude ozone distribution, we have unfortunately found this topic to be more extensive than time permitted under this contract.

2.3.2 Constituents Derived from Stellar-Occultation Technique

For stellar occultation observations, we plan to monitor certain bright (relatively young) stars as they are occulted by the earth. In this manner, ozone concentrations may then be obtained using starlight, rather than scattered-sunlight, as the energy source. Neutral atmospheric density may be monitored by observing the attenuation of starlight resulting from scattering in the 20-60 km region. To obtain neutral atmospheric densities at higher altitudes, we plan to observe the starlight at wavelengths within the Schumann-Runge absorption bands of molecular oxygen (1750-2100 Å). Molecular-oxygen concentrations above 50 km may be deduced in this way and, since the atmosphere is well-mixed up to an altitude of 90 km, it is straightforward to deduce neutral atmospheric density and hence temperature.

2.3.3 Constituents Derived from Airglow-Emission Technique

We intend to deduce atomic-oxygen concentration profiles in the neighborhood of 100 km by observing the emission at 5577 Å from the ^1S state of atomic oxygen and by observing the emission from the Herzberg rotation-vibration band of molecular oxygen (2600-3500 Å). The feasibility of yielding nighttime atomic-oxygen concentrations is discussed in detail in Section 3.3 and in Cunnold, 1970 and 1971. It is to be noted that we do not expect to be able to deduce absolute values of the oxygen concentration to better than a factor of two. However, it is changes in the atomic oxygen concentration which are more relevant for interpreting atmospheric processes and we therefore believe that this is not a significant limitation of our experiment. Because the physical processes responsible for emission at the 100-km level during daylight are not clearly understood, we cannot now claim that daytime 5577 Å measurements may be used to deduce atomic-oxygen concentration. We are hopeful that further theoretical and experimental studies of 5577 Å dayglow will render such measurements meaningful.

Atomic oxygen is produced by the photodissociation of oxygen molecules at altitudes above 100 km and is then transported downwards by eddy mixing to lower levels where it is lost via chemical recombination processes. A

concentration peak is thus formed at about the 95-km level. An estimated profile of atomic-oxygen concentration is presented in Fig. 2.3-5. Direct observations of atomic oxygen below 120 km have been difficult, although a new technique (Henderson, 1971) appears promising in this regard. Consequently, present knowledge of the atomic oxygen concentration between 90 and 100 km is based upon indirect measurement and theoretical extrapolation of measurements at higher altitudes. Almost an order of magnitude uncertainty must therefore be assigned to the atomic oxygen concentration.

Another minor constituent which possesses a measurable emission in the wavelength band to be used in the Aeronomy Experiment is nitric oxide. We can measure the daytime nitric oxide concentrations by observing sunlight which has been resonantly scattered in the γ bands (2000-2700 Å) of nitric oxide. In particular, we plan to use the 1-0 band at 2150 Å. While it is anticipated that this technique will permit readily interpretable observations above 70 km, the results may be theoretically extended to lower altitudes if theory is correct that nitric oxide is well-mixed below that altitude (Strobel et al, 1970). At the present time, only limited observations of the nitric oxide concentration have been made. A range of estimated profiles from Strobel et al, is contained in Fig. 2.3-6.

The airglow emission at 1.27μ is conceptually an independent technique of determining daytime ozone concentrations. This emission (referred to as the infrared atmospheric band) is from the $^1\Delta_g$ state of molecular oxygen, which produces the vibration-rotation spectrum of which the 1.27μ emission is the 0-0 band. The emission is discussed in Evans and Llewellyn (1970) and in Cunnold (1971). At the present time, doubt remains about the origin of the emission—particularly at altitudes above 80 km. However, if present concepts (Evans and Llewellyn, 1970) prove to be correct, it is anticipated that measurements of the 1.27μ emission should yield daytime ozone concentrations between 60 and 100 km. In common with most constituent density determinations involving airglow emissions, some uncertainty (approximately 20%) would remain about the absolute value of the ozone concentration—at least until further reaction-rate measurements could be made.

Other important airglow emissions which fall within our anticipated instrument sensitivity are that from $N_2^+[1N]$ at 3914 Å, and that from $N_2[2P]$ at 3371 Å. Both of these emissions are excited by electron impact. Altitude and emission profiles should therefore produce information on the energy spectrum of electrons (both photoelectrons and auroral electrons) entering the atmosphere from above this region. $N_2^+[1N]$ emission is particularly important for directly indicating auroral energetics. Definitive information thus obtained on the presence of aurora establishes the background in which constituent densities must be determined.

TABLE 2.3-I

NEUTRAL DENSITIES (N/CM^3) AND STANDARD DEVIATIONS (%) *†

Alt. (Km)	Tropical	Midlatitude Summer	Midlatitude Winter	Subarctic Summer	Subarctic Winter
0	2.43×10^{19} (3)	2.48×10^{19} (3)	2.71×10^{19} (3)	2.63×10^{19} (3)	2.95×10^{19} (3)
5	1.50×10^{19} (3)	1.50×10^{19} (3)	1.54×10^{19} (3)	1.52×10^{19} (3)	1.56×10^{19} (3)
10	7.24×10^{18} (2)	7.31×10^{18} (3)	7.32×10^{18} (3)	7.42×10^{18} (3)	7.53×10^{18} (3)
15	3.50×10^{18} (2)	3.56×10^{18} (3)	3.48×10^{18} (3)	3.62×10^{18} (3)	3.63×10^{18} (3)
20	1.69×10^{18} (1)	1.74×10^{18} (3)	1.65×10^{18} (3)	1.77×10^{18} (3)	1.75×10^{18} (4)
25	8.32×10^{17} (1)	8.48×10^{17} (3)	7.84×10^{17} (3)	8.59×10^{17} (3)	8.33×10^{17} (4)
30	3.70×10^{17} (1)	3.87×10^{17} (2.5)	3.56×10^{17} (3)	4.03×10^{17} (3)	3.66×10^{17} (5)
35	1.71×10^{17} (2)	1.83×10^{17} (2.5)	1.64×10^{17} (3)	1.91×10^{17} (4)	1.61×10^{17} (7)
40	8.40×10^{16} (2.5)	8.90×10^{16} (2.5)	7.63×10^{16} (3)	9.40×10^{16} (4)	7.03×10^{16} (9)
45	4.30×10^{16} (2.5)	4.51×10^{16} (2.5)	3.74×10^{16} (3)	4.80×10^{16} (5)	3.18×10^{16} (13)
50	2.25×10^{16} (2.5)	2.41×10^{16} (2.5)	1.95×10^{16} (3)	2.60×10^{16} (5)	1.50×10^{16} (17)
55	1.22×10^{16} (2.5)	1.33×10^{16} (7)	1.06×10^{16} (10)	1.46×10^{16} (5)	7.42×10^{15} (16)
60	6.80×10^{15} (3)	7.42×10^{15} (7)	5.76×10^{15} (10)	8.32×10^{15} (6)	3.99×10^{15} (16)
65	3.78×10^{15} (3)	4.05×10^{15} (7)	3.04×10^{15} (10)	4.68×10^{15} (10)	2.08×10^{15} (16)
70	1.98×10^{15} (3)	2.08×10^{15} (8)	1.57×10^{15} (10)	2.54×10^{15} (12)	1.03×10^{15} (15)
75	9.23×10^{14} (5)	9.93×10^{14} (11)	7.59×10^{14} (10)	1.30×10^{15} (15)	5.01×10^{14} (15)
80	4.05×10^{14} (7)	4.22×10^{14} (11)	3.56×10^{14} (10)	6.05×10^{14} (17)	2.29×10^{14} (15)
85	1.77×10^{14} (14)	1.71×10^{14} (15)	1.58×10^{14} (15)	2.35×10^{14} (20)	1.05×10^{14} (20)
90	7.69×10^{13} (40)	6.28×10^{13} (16)	6.92×10^{13} (16)	6.90×10^{13} (24)	4.68×10^{13} (40)
95	3.08×10^{13} (40)	2.12×10^{13} (20)	2.93×10^{13} (20)	1.95×10^{13} (24)	2.14×10^{13} (40)
100	1.21×10^{13} (60)	8.30×10^{12} (40)	1.29×10^{13} (40)	6.34×10^{12} (24)	9.86×10^{12} (40)
105	5.03×10^{12} (60)	3.70×10^{12} (40)	5.64×10^{12} (40)	2.60×10^{12} (24)	4.66×10^{12} (40)
110	2.25×10^{12} (60)	1.79×10^{12} (40)	2.47×10^{12} (40)	1.21×10^{12} (24)	2.10×10^{12} (40)

* Standard deviations are given in parentheses alongside densities.

† Data taken from Groves (1971 COSPAR) and Handbook of Geophysical and Space Environments.

TABLE 2.3-II

NUMBER DENSITY OF OZONE

Altitude (km)	ρ(mean) cm^{-3}	$\rho(+3\sigma)$ cm^{-3}	$\rho(-3\sigma)$ cm^{-3}
20	1.20×10^{12}	3.60×10^{12}	2.20×10^{11}
24	1.70×10^{12}	5.60×10^{12}	3.50×10^{11}
28	2.40×10^{12}	5.60×10^{12}	6.00×10^{11}
30	2.70×10^{12}	5.00×10^{12}	8.00×10^{11}
32	2.60×10^{12}	4.20×10^{12}	1.00×10^{12}
34	2.20×10^{12}	3.50×10^{12}	1.05×10^{12}
36	1.65×10^{12}	2.75×10^{12}	9.00×10^{11}
38	1.20×10^{12}	2.20×10^{12}	7.00×10^{11}
40	8.95×10^{11}	1.50×10^{12}	4.70×10^{11}
42	5.77×10^{11}	1.00×10^{12}	3.00×10^{11}
44	3.72×10^{11}	7.20×10^{11}	1.80×10^{11}
46	2.40×10^{11}	5.00×10^{11}	1.10×10^{11}
48	1.55×10^{11}	3.40×10^{11}	6.00×10^{10}
50	1.00×10^{11}	2.50×10^{11}	3.50×10^{10}
54	4.16×10^{10}	1.30×10^{11}	1.16×10^{10}
56	2.68×10^{10}	9.00×10^{10}	6.60×10^{9}
60	1.12×10^{10}	4.50×10^{10}	2.30×10^{9}
64	4.63×10^{9}	1.92×10^{10}	7.60×10^{8}
66	3.00×10^{9}	1.70×10^{10}	4.50×10^{8}
70	1.20×10^{9}	8.00×10^{9}	1.62×10^{8}
74	5.18×10^{8}	4.00×10^{9}	6.00×10^{7}
76	3.34×10^{8}	2.80×10^{9}	3.70×10^{7}
80	1.40×10^{7}	1.40×10^{9}	1.40×10^{7}

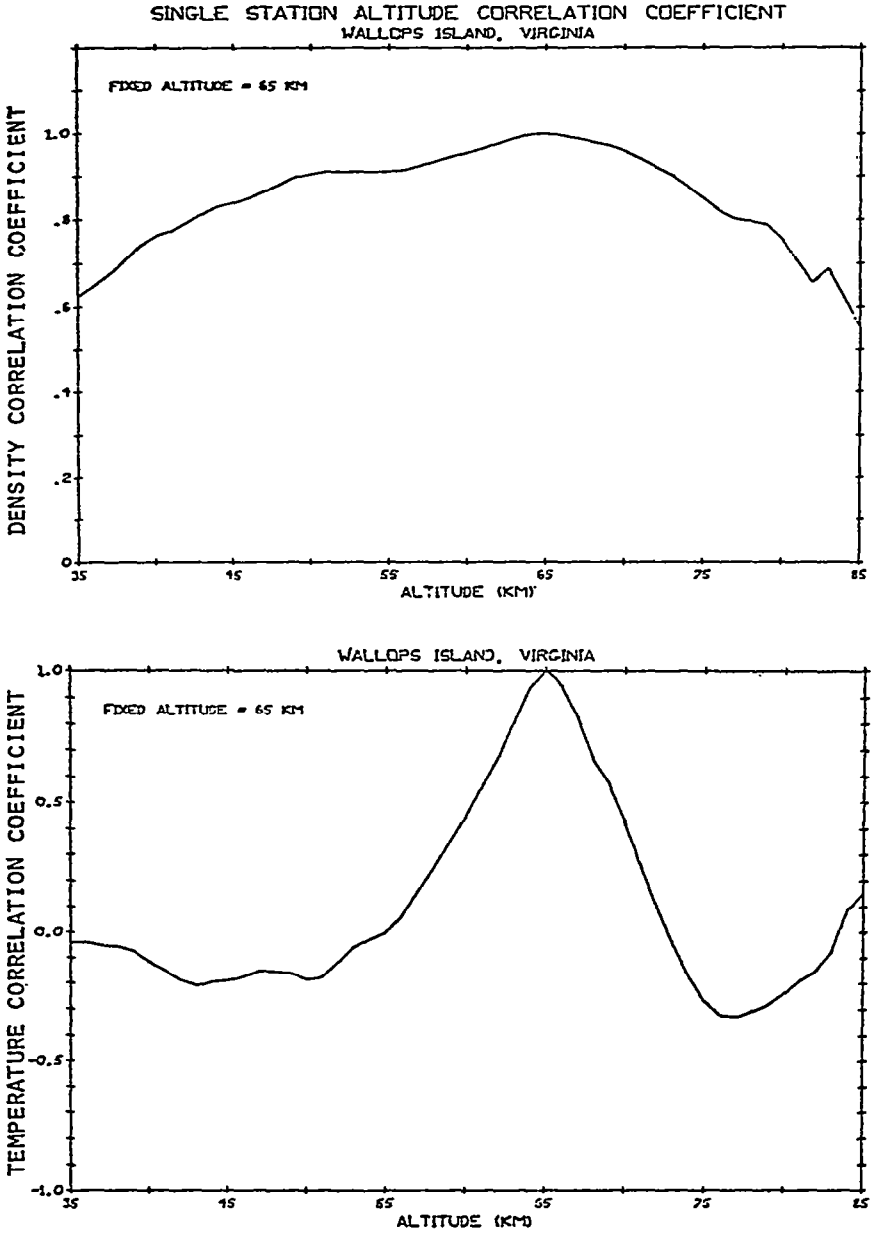

Fig. 2.3-1 Single station density (top) and temperature (bottom) altitude correlation coefficients for 65 km altitude over Wallops Island, Va., based upon density profiles presented by Smith et al (1960-68).

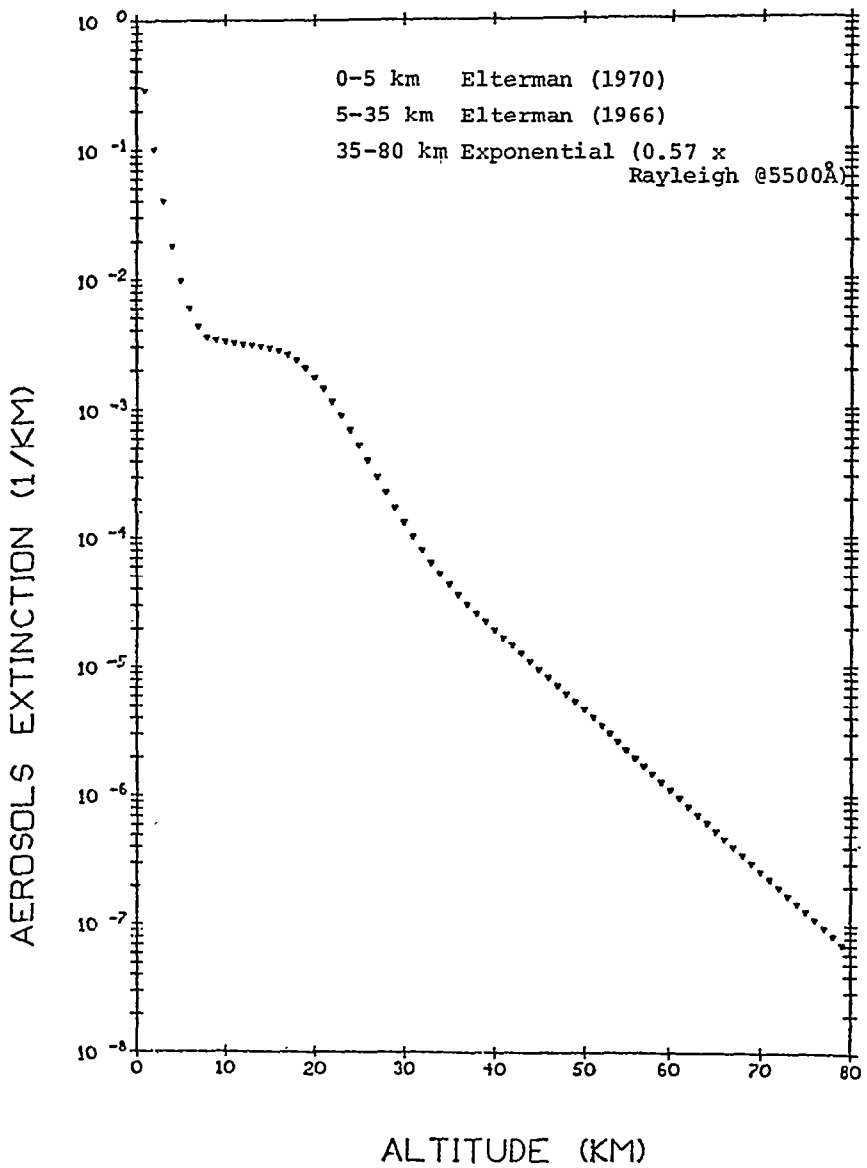

Fig. 2.3-2 Reference Aerosol Extinction Model @ λ=5500 Å

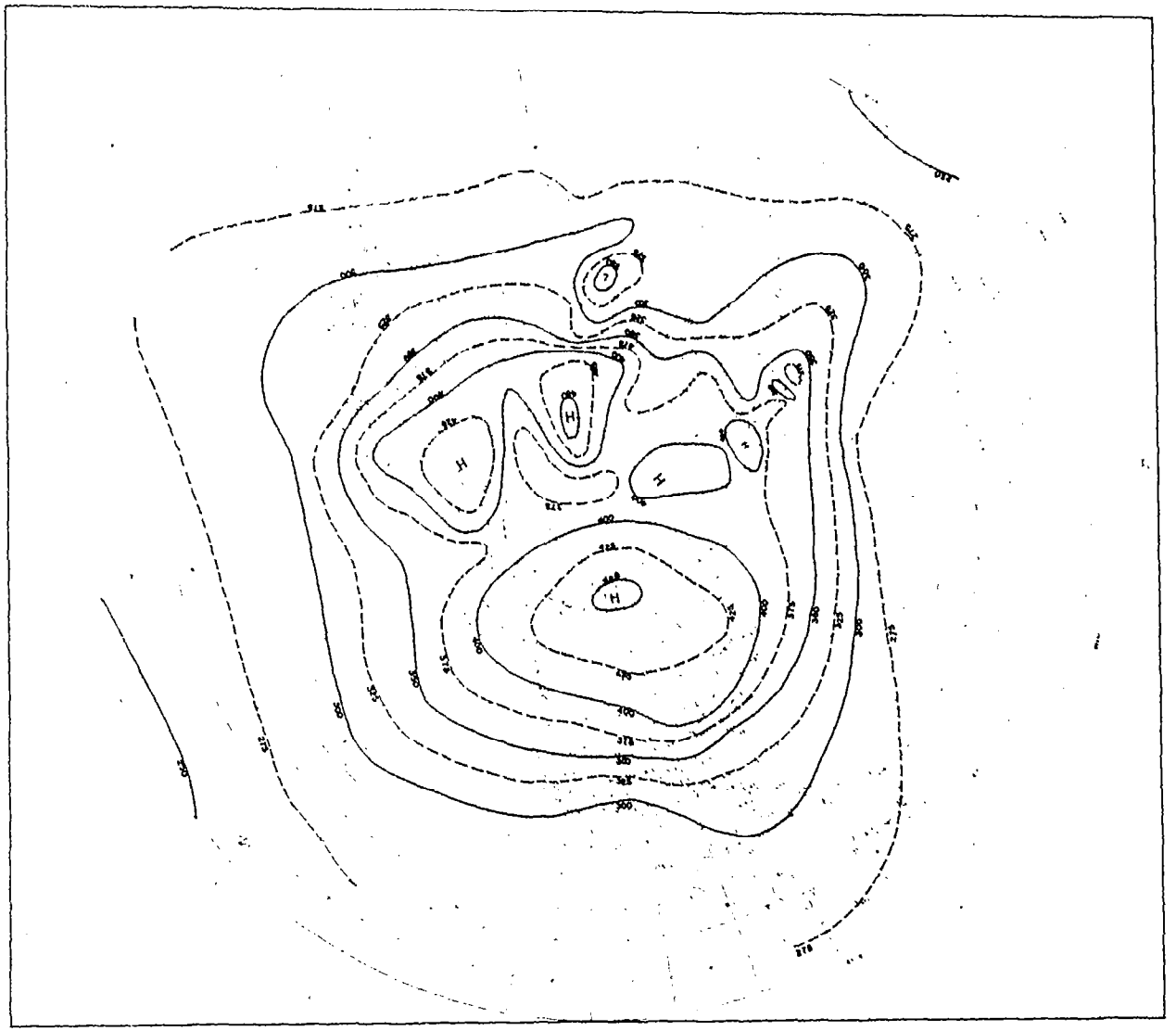

Fig. 2.3-3. World wide distribution of three-month (Mar-May) average of total ozone in northern hemisphere during 1960-1968. (Wu, 1970)

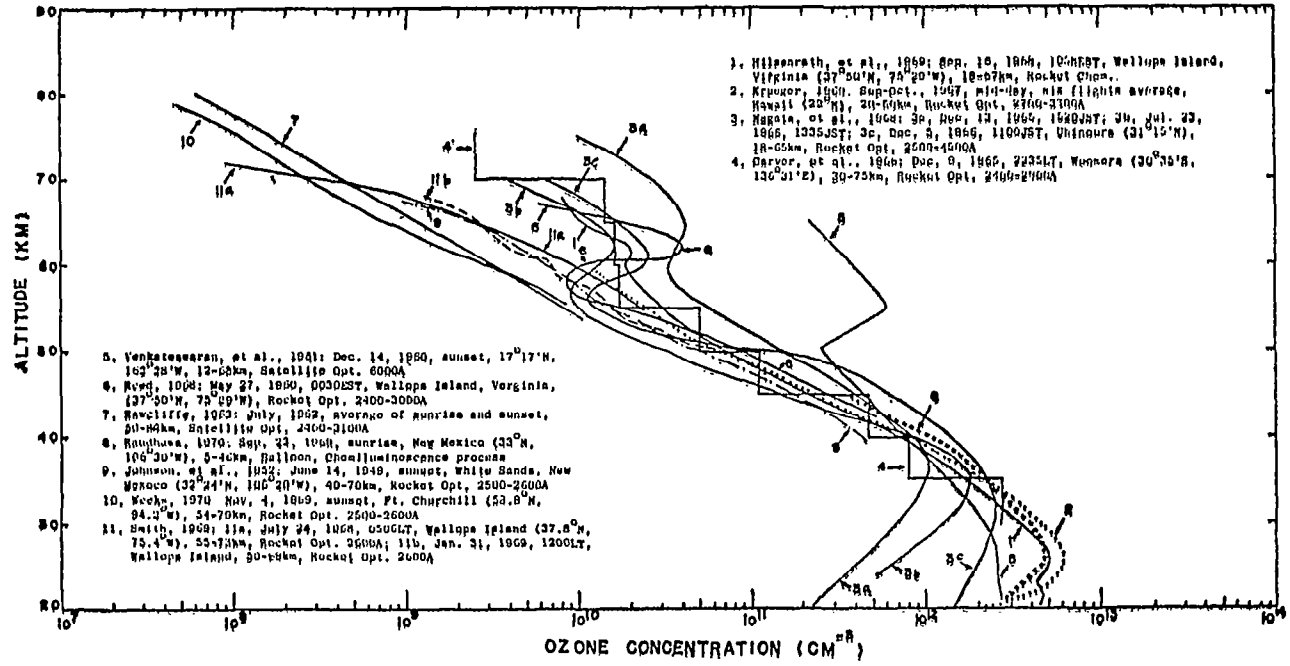

Fig. 2.3-4 Observations on ozone distributions obtained by various workers with rocket and satellite-borne instruments.

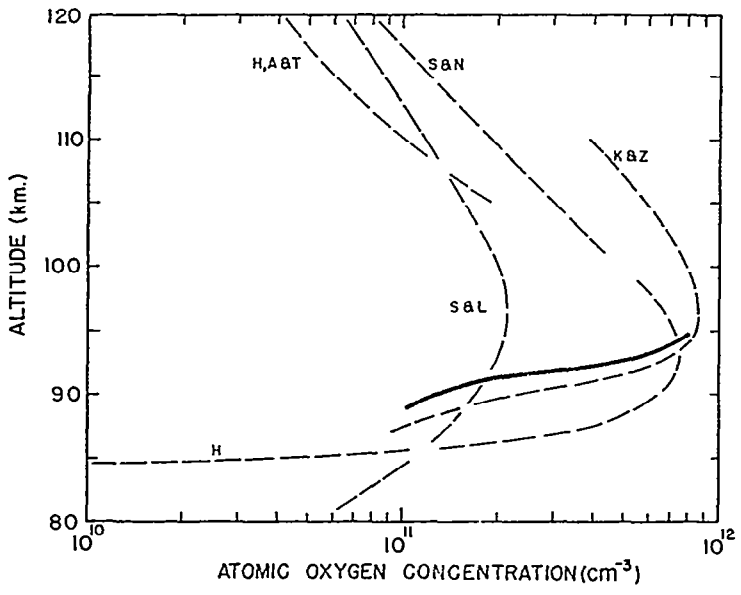

Fig. 2.3-5 Results of silver film measurement of atomic oxygen are presented as a heavy solid line; dotted lines represent calculations of *Shimazaki and Laird* [1970] (S&L); *Hesstvedt* [1968] (H); and *Keneshea and Zimmerman* [1970] (K&Z); and rocket mass spectrometric measurements of *Shaefer and Nichols* [1964] (S&N); and *Hedin et al.*, [1964] (H, A&T); (Henderson, 1971).

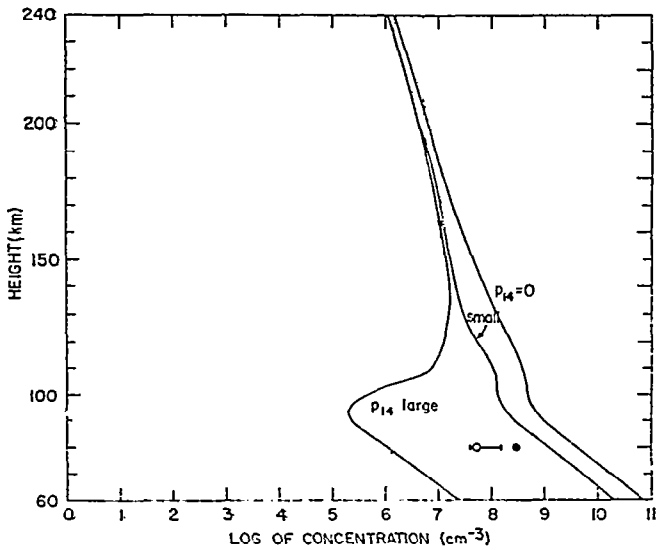

Figure 2.3-6 Theoretical values of nitric oxide concentration for several values of an electron impact parameter p_{14}. The solid circle indicates the NO concentration observed by Pearce, and the bar with a circle indicates that observed by Barth (Strobel et al., 1970).

References for Section 2.3

Cole, A. E., "Extreme Temperature, Pressure, and Density Between 30 and 80 Km," Air Force Environment Research Paper No. 330, August, 1970.

Cunnold, D. M., "The Deduction of Atomic Oxygen Concentrations from Measurements of 5577 Å and Herzberg Emission," Internal Report No. AER 2-4, April, 1971.

_____, "The Deduction of Temperature from Atmospheric Density Measurements," Internal Report No. AER 4-1, February, 1971.

_____, "The Emission from the $^1\Delta_g$ State of O_2 and its Application as a Technique to Measure Ozone Concentration," Internal Report No. AER 2-1, January, 1971.

_____, "The Measurement of 5577 Å Radiation Profiles," Internal Report No. AER 2-1, August, 1970.

Elterman, L., "An Atlas of Aerosol Attenuation and Extinction Profiles for the Troposphere and Stratosphere," Air Force Cambridge Research Laboratories, 66-828, December 1966.

_____, "Vertical-Attenuation Model with Eight Surface Meteorological Ranges 2 to 13 Kilometers," Air Force Cambridge Research Laboratories, 70-0200, March 1970.

Evans, W. F. J., and Llewellyn, E. J., Molecular Oxygen Emissions in the Airglow, Ann. Geophys. 26, 167-178, 1970.

Groves, G. V., "Seasonal and Latitudinal Models of Atmospheric Temperature, Pressure, and Density," Air Force Surveys in Geophysics, No. 218, May 1970.

Henderson, W. R., D-Region Atomic Oxygen Measurements, Journal of Geophysical Research, Vol. 76, No. 13, 3166-67, May 1971.

Salah, J. E., "On the Nature and Distribution of Stratospheric Aerosols," Internal Report No. AER 6-2, February, 1971.

Smith, W. S., J. S. Theon, P. C. Swartz, J. F. Casey, J. J. Horvath, L. B. Katchen, and P. Sacher, "Temperature, Pressure, Density, and Wind Measurements in the Upper Stratosphere and Mesosphere," NASA-TR-R-211, 245, 263, 288, 316, 340, 1960-1968.

Strobel, D. F., Hunten, D. M., McElroy, M. B., Production and Diffusion of Nitric Oxide, Journal of Geophysical Research, Vol. 75, No. 22, 4307-4321, August 1970.

Wu, M. F., "Ozone Distribution and Variability," Internal Report No. AER 1-2, August 1970.

2.4 WAVELENGTH SELECTION

2.4.1 Introduction

Since the light scattering and absorbing properties of the constituent densities are wavelength-dependent, it might be expected that certain wavelengths are better suited than others for estimating particular constituents. For example, it would be expected that wavelengths which are highly attenuated and do not penetrate deeply into the atmosphere will not yield information about constituent densities near the ground.

It is therefore desirable to define a function (based on the radiative transfer characteristics of simulated constituent density profiles and the horizon geometry) which will yield a priori information indicating the optimal wavelength for inverting a particular constituent in a specific altitude region. We call this function peak sensitivity and it is derived formally from the filter equations in section 3.1.4 and 3.2.4. In practice, sensitivities in excess of .05 may be used to obtain constituent densities.

2.4.2 Scattered Sunlight

Inversion sensitivities for the scattered-sunlight constituents (ozone, neutral atmospheric density and aerosols) are illustrated in Fig. 2.4-1. For each of the constituents, the curves plotted are the peak values of the line-of-sight sensitivity envelope for each coplanar tangent-altitude increment. The formal development of the sensitivity definition for the scattered-sunlight inversion is contained in Section 3.1.4 and Merritt and Var, 1971.

Close examination of these inversion sensitivity curves shows that the significance of aerosols as a primary constituent in the stratosphere and mesosphere cannot be overemphasized (Section 3.7). It is therefore important to note that an accurate inversion of aerosol extinction is predicted on the basis of the inversion-sensitivity curves. Ozone sensitivity remains relatively constant with sun angle for the coplanar case. Neutral atmospheric density sensitivities are dominated at the longer wavelengths by the aerosol sensitivities because of the angular-scattering function and distribution characteristics.

Specification of the wavelength bandwidth and related primary constituent for the scattered-sunlight measurements are shown in Table 2.4-I. The maximum expected signals for each spectral region are for a diffraction-limited optical system with a 100-cm^2 entrance aperture and 1.5×10^{-5} steradian field of view. These maximum expected intensities are based on X-15-1 data (Gray, 1969) and Nimbus-BUV data (Heath, 1970). The range in expected maximum intensities will be approximately a factor of two in the ultraviolet region and visible region to 5800 Å. At 7000 Å, however, the variability in observed conditions indicates that the maximum intensity could be an order of magnitude less than that tabulated.

2.4.3 Stellar Occultation

For the stellar-occultation constituent sensitivities, aerosols, ozone and neutral atmospheric density were modeled. The results of the stellar

occultation-inversion sensitivity analysis are illustrated in Fig. 2.4-2 and documented in Section 3.2.4 and in Merritt, 1972. Noted here is the nighttime sensitivity to ozone and neutral atmospheric density over a wide altitude region. Although aerosol sensitivities are only significant at lower altitudes, it is important to note that the constituent sensitivities are based on both the initial statistics and the density distribution. Thus, where there is a higher-altitude (anomalous) aerosol layer, the constituent sensitivities would reflect the perturbed distribution. Documentation of the wavelength, bandwidth, and primary inversion constituents for the stellar occultation case are also shown in Table 2.4-I. The maximum expected signals are for a 11,200°K, m_v=0 star (a typical bright star) utilizing diffraction-limit optics with an entrance aperture of 100 cm^2.

2.4.4 Emissions

The emission wavelengths for monitoring (1) atomic oxygen $O[^1S]$, (2) nitrogen $N_2^+[1N]$ and $N_2[2P]$, (3) molecular oxygen $[O_2]$, and (4) nitrous oxide $[NO]$, have recently been confirmed by laboratory experiments and rocket flight. Tabulation of the maximum expected intensity for these emission measurements, wavelengths, and bandwidths, are also contained in Table 2.4-I and referenced in Cunnold, 1970, and Cunnold and Gray, 1971. Specification of the emission wavelengths followed the wavelength sensitivity requirements set forth for the scattered-sunlight and stellar-occultation measurement data sets. In each case, the tabulated wavelength specifications are spectrally located at or near the optimum wavelength, without sacrificing constituent inversion sensitivity.

While some variations in emission intensities are to be expected, it is anticipated that, in general, the emissions will fall within one order of magnitude of the values listed. However, at high geomagnetic latitudes, aurora will often occur and in that case the emissions from $O[^1S]$, $N_2^+[N]$ and $N_2[2P]$ may exceed the quoted values by as much as three orders of magnitude.

TABLE 2.4-I

MAXIMUM EXPECTED SIGNALS

Wavelength (Angstroms)	Bandwidth (Angstroms)	Measurement	Constituent	Photons per Second	Watts
1900	20	Occultation**	Neutral Density	1.1×10^{6}	1.15×10^{-12}
2000	20	Occultation**	Neutral Density	1.35×10^{6}	1.35×10^{-12}
2150	10	Occultation**	Neutral Density & Ozone	8.0×10^{5}	7.4×10^{-13}
		Emission* (D)	Nitric Oxide [NO]	1.35×10^{6}	1.25×10^{-12}
2600	20	Occultation**	Ozone	2.2×10^{6}	1.7×10^{-12}
		Scattered Sunlight*	Ozone	1.5×10^{7}	1.14×10^{-11}
2850	20	Occultation**	Ozone	2.4×10^{6}	1.7×10^{-12}
		Scattered Sunlight*	Ozone	9.0×10^{7}	6.2×10^{-11}
		Emission* (N)	Molecular Oxygen [O_2]	1.2×10^{5}	8.4×10^{-14}
3100	20	Occultation**	Ozone	2.4×10^{6}	1.55×10^{-12}
		Scattered Sunlight*	Neutral Density & Ozone	1.45×10^{10}	9.3×10^{-9}
3371	10	Occultation**	Neutral Density	1.1×10^{6}	7.2×10^{-13}
		Scattered Sunlight*	Neutral Density	2.55×10^{10}	1.5×10^{-8}
		Emission* (D, A)	Nitrogen N_2[2P]	2.6×10^{6}	1.5×10^{-12}
3914	10	Occultation**	Neutral Density	9.3×10^{5}	6.0×10^{-13}
		Scattered Sunlight*	Neutral Density & Aerosols	4.8×10^{10}	2.43×10^{-8}
		Emission* (D, A)	Nitrogen N_2^+[1N]	2.6×10^{6}	1.3×10^{-12}
5577	10	Occultation**	Ozone	8.1×10^{5}	2.9×10^{-13}
		Scattered Sunlight*	Neutral Density & Aerosols	6.3×10^{10}	2.25×10^{-8}
		Emission* (D, N, A)	Atomic Oxygen O[^{1}S]	1.05×10^{6}	3.7×10^{-13}
7000	10	Occultation**	Aerosols	5.6×10^{5}	1.6×10^{-13}
		Scattered Sunlight*	Aerosols	1.05×10^{11}	3.0×10^{-8}

*entrance aperture - 100 cm^2
field of view - 1.5×10^{-5} steradians

(D) - Daytime
(N) - Nighttime
(A) - Aurora

**entrance aperture - 100 cm^2
star - 11,200°K; $m_v = 0$

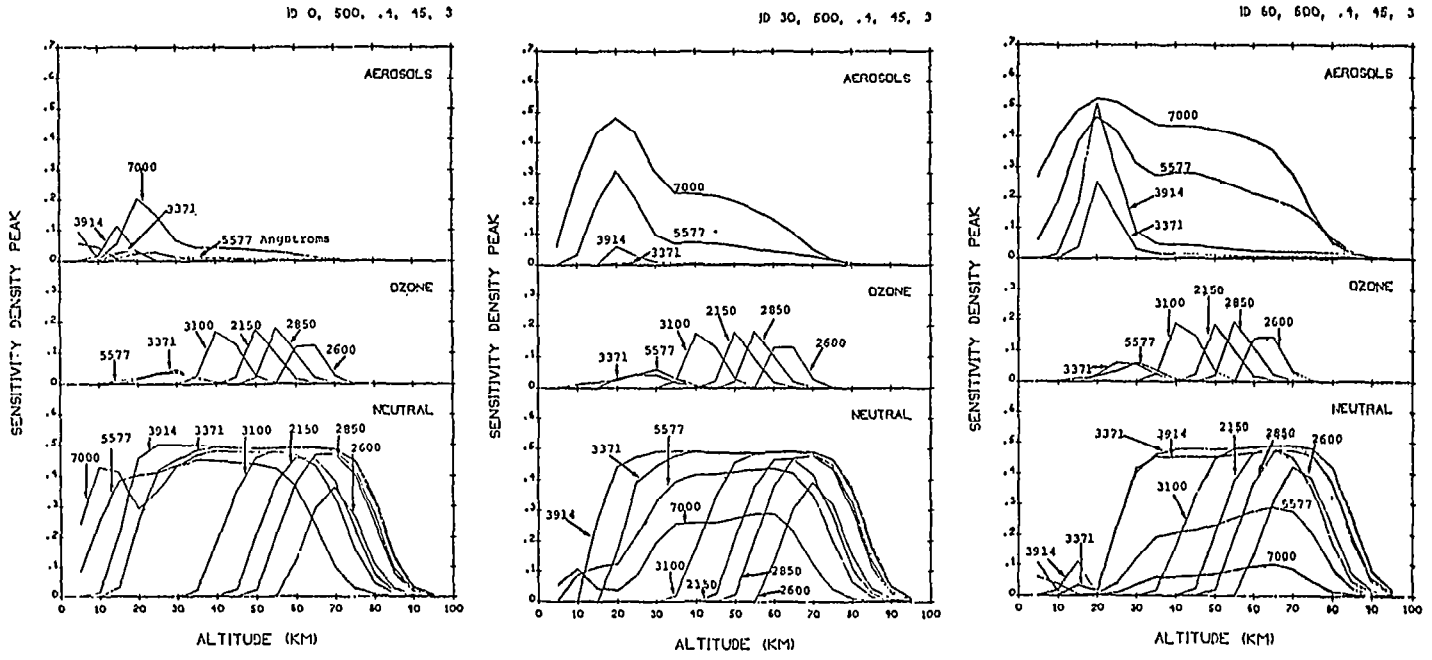

Fig. 2.4-1 Scattered Sunlight Constituent Peak Sensitivity Profiles (Zenith Angle = 0°, 30°, 60°--left to right)

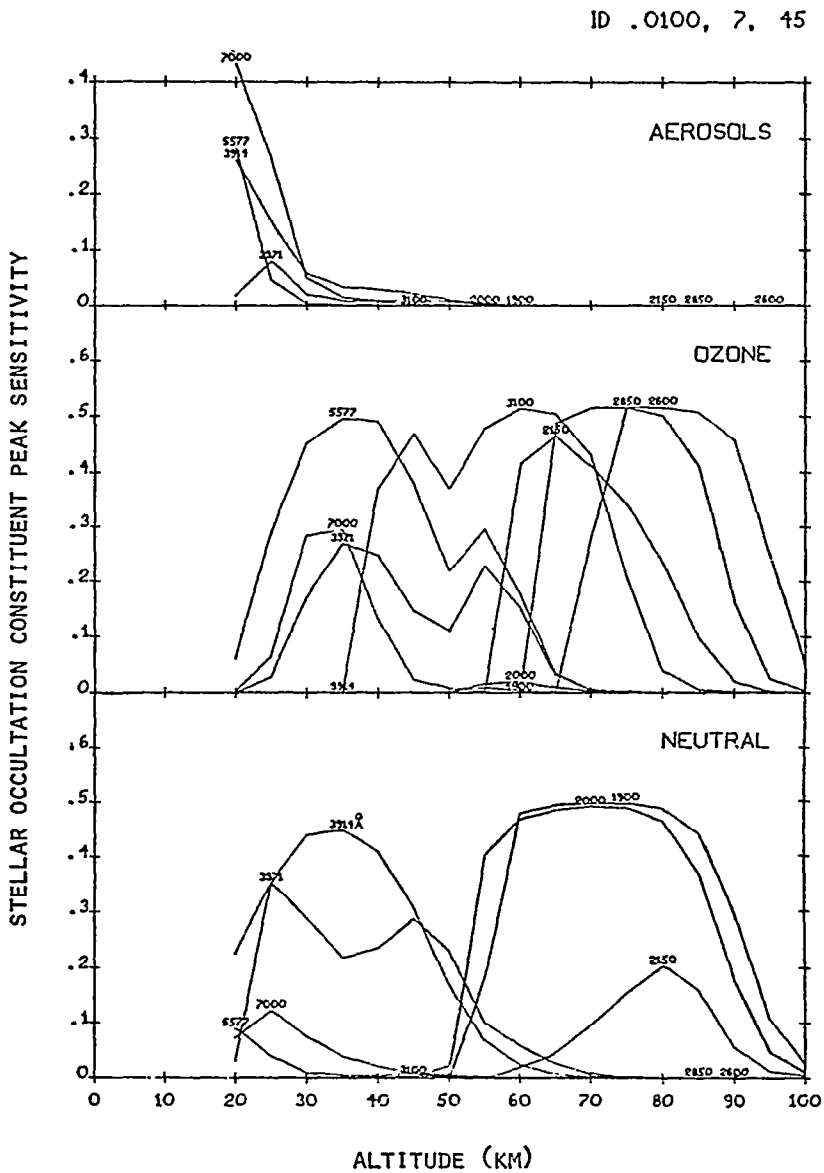

Fig. 2.4-2 Stellar Occultation Constituent Peak Sensitivity Profiles

References for Section 2.4

Cunnold, D. M., "The Measurement of 5577 Å Radiation Profiles", Internal Report No. AER 2-1, August, 1970.

Cunnold, D. M., and Gray, C. R., "Constituent Detectivity of the Aeronomy Limb-Scanning Experiment", Internal Report No. AER 9-2, May, 1971.

Gray, C. R., 1969: MIT/IL X-15 Horizon Definition Experiment Final Report. Apollo Guidance and Navigation, MIT Instrumentation Laboratory, R-648.

Heath, D. F., and Krueger, A., Nimbus 4-BUV data, 12 April 1970.

Merritt, D. C., "The Estimation of Atmospheric Constituent Densities Through the Inversion of Stellar Occultation Measurements", Internal Report No. AER 8-8, January, 1972.

Merritt, D. C., and Var, R. E., "The Estimation of Atmospheric Constituent Densities Through the Inversion of Scattered Sunlight Measurements", Internal Report No. AER 8-7, August, 1971.

2.5 THE INVERSION PROCESS

2.5.1 Introduction

The generation of the earth's horizon profiles is described by the well known equation of radiative transfer, which includes as variables the densities of the various atmospheric constituents. In principle, the densities can be recovered from horizon measurements. However, the situation is complicated by the fact that the constituents appear both as sources and as attenuators. Reviewed here for the scattered-sunlight inversion process are the mathematical roles played by the radiative-transfer models and the recursive filters. The general Aeronomy horizon-inversion techniques for recovery of constituent densities are applicable to the cases of stellar occultation and airglow emission inversion as well.

2.5.2 Scattered-Sunlight Inversion

Scattered sunlight in the spectral interval 2000 to 7000 Å can be inverted to obtain the densities of scattering air molecules, aerosols, and ozone. Each of these constituents strongly affects the radiative transfer at some altitude and wavelength in the chosen spectral interval. Radiation is scattered into the field of view of the horizon-scanning telescope by all of the molecular and aerosol particles along the path traced by the telescope line of sight. If one mathematically divides the atmosphere into a set of n thin, concentric spherical layers (thin enough, say, to consider scale height a constant over the interval), then the receiver field of view can then be expressed mathematically as a function of the densities of the relevant constituents taken at reference points within or bounding the n layers. Formally, one can write

$$I_{Mj} = f_j\left(\rho_{11},\cdots\rho_{1n},\cdots,\ \rho_{k1}\cdots\rho_{kn}\right) \quad , \qquad (2.5\text{-}1)$$

where I_{Mj} is the measured signal at scan position j; $\rho_{k1}\ldots\rho_{kn}$ are the reference densities of the k constituents for the n layers, and f_j is a function which satisfies the differential equation of radiative transfer. It is reasonable to assume horizontal homogeneity, since the telescope line of sight intersects the atmosphere over a significant path length of the order of 300 km. The densities $\rho_1\ldots\rho_n$ are assumed constant for a complete altitude scan. Thus, each successive scan angle yields a new I_{Mj} value and a new function f_j. After completing one limb scan, at one wavelength, one has established in a formal sense the set of equations

$$\begin{aligned} I_{M1} &= f_1\left(\rho_{11}\cdots\rho_{1n},\cdots,\ \rho_{k1}\cdots\rho_{kn}\right) \quad . \qquad (2.5\text{-}2) \\ &\vdots \\ I_{M\ell} &= f\ \left(\rho_{11}\cdots\rho_{1n},\cdots,\ \rho_{k1}\cdots\rho_{kn}\right) \quad . \end{aligned}$$

Here ℓ is the number of scan positions, which, in general, may be unequal to the number of layers n.

In principle, this set of equations can be solved simultaneously to obtain the $\rho_{k1} \ldots \rho_{kn}$ values, given that there are as many independent equations as unknown ρ_{kn} values. In the case of a one-constituent atmosphere, the criterion for a sufficient set of independent equations is that there be at least one radiance sampling within each layer interval. This criterion could also be expressed by saying that the mapping of the line-of-sight sample points should place one line of sight within each defined layer. If additional constituents are present, it is necessary to expand the set of independent equations by sampling the radiation at one additional wavelength for each added constituent.

It is important to emphasize at this point that the equation set (2.5-2) can be directly and deterministically solved or "inverted" only in principle. In a real situation, the functions f_ℓ are complicated beyond closed form statement, the measurements $I_{M\ell}$ are contaminated with noise, and the ρ_{kn} values are coupled with one another.

A much more viable approach is to apply the technique of modern filter theory. With this approach, the first step is to assume that the complicated numerical solution to the transfer equation can be expanded linearly, i.e., that equation (2.5-2) can be expanded in the form

$$\Delta I_\ell = \sum_{k=1}^{k} \sum_{n=1}^{n} \frac{\partial f_\ell}{\partial \rho_{kn}} \Delta \rho_{kn} \quad . \qquad (2.5\text{-}3)$$

Here, as before, the ρ_{kn} are k constituent densities related to n mathematical layers. This equation says in effect that a set of small deviations of the ρ_{kn} lead to a small change in the intensity. Let us then assume that we have an initial estimate of ρ_{kn}, and we have also an initial estimate of I which we obtain numerically by solving the radiative transfer equations. The partial derivatives $\partial f / \partial \rho_{kn}$ can be obtained numerically by the same procedure. The equation set resulting from the set ℓ of scan sample positions then takes the form (after a horizon scan)

$$\begin{aligned} I_{1M} - I_{1c} &= \sum_{i=1}^{k} \sum_{j=1}^{n} \left(\frac{\partial f_1}{\partial \rho_{ij}} \right)_c \left(\rho_{ij} - \rho_{ij}(0) \right) \\ &\vdots \qquad\qquad \vdots \qquad\qquad \vdots \\ I_{\ell M} - I_{\ell c} &= \sum_{i=1}^{k} \sum_{j=1}^{n} \left(\frac{\partial f_\ell}{\partial \rho_{ij}} \right)_c \left(\rho_{ij} - \rho_{ij}(0) \right) \end{aligned} \quad . \qquad (2.5\text{-}4)$$

Here, again, I_{Mj} is the measured intensity at the j^{th} scan position. I_{cj} is the calculated value. The partials are also calculated. The densities $\rho_{ij}(0)$ are the initial assumed values. If the measurement by chance equalled the computed I_{cj}, then $\rho_{ij} = \rho_{ij}(0)$ for all i,j. On the other hand, the general condition that $I_{M\ell} \neq I_{c\ell}$ leads to a set of linear equations in the unknowns ρ_{ij} which can be solved to yield these densities. This procedure eliminates the problem of solving the explicit transfer equation solutions. However, this method also leaves one with the problems of handling the statistics of the measurement noise, and of the initial estimate of $\rho_{ij}(0)$. These statistical problems are best handled by recasting equation set (2.5-4) in linear recursive-filter forms. The filter will apportion each ΔI value among the $\Delta\rho$'s in such a way that the collective variances of the ρ_{ij}'s are always minimized. The apportionment or "weighting" factor is so structured that when the measurement uncertainty is large, with respect to the uncertainty in the initial estimate, the measurement is effectively ignored, i.e., given little weight. Conversely, if the measurement is much more accurate than the initial estimate, the initial estimate is effectively ignored and the measured value is accepted.

It is instructive here to look at a simple case. Assume a one-constituent atmosphere of three layers. According to our linearization, the relation between the measurement and the densities is

$$I_{M\ell} - I_{c\ell} = \frac{\partial f_\ell}{\partial \rho_1}\left(\rho_1 - \rho_1(0)\right) + \frac{\partial f_\ell}{\partial \rho_2}\left(\rho_2 - \rho_2(0)\right) + \frac{\partial f_\ell}{\partial \rho_3}\left(\rho_3 - \rho_3(0)\right), \quad (2.5\text{-}5)$$

Now the recursive filter for this problem yields the set of three equations

$$\begin{aligned} \rho_1 - \rho_1(0) &= \omega_1\left(I_{M\ell} - I_{c\ell}\right) \quad , \\ \rho_2 - \rho_2(0) &= \omega_2\left(I_{M\ell} - I_{c\ell}\right) \quad , \\ \rho_3 - \rho_3(0) &= \omega_3\left(I_{M\ell} - I_{c\ell}\right) \quad . \end{aligned} \quad (2.5\text{-}6)$$

These equations can be solved for

$$I_{M\ell} - I_{c\ell} = \frac{1}{3\omega_1}\left(\rho_1 - \rho_1(0)\right) + \frac{1}{3\omega_2}\left(\rho_2 - \rho_2(0)\right) + \frac{1}{3\omega_3}\left(\rho_3 - \rho_3(0)\right). \quad (2.5\text{-}7)$$

The similarity between these recast filter equations and the linear equation (2.5-5) is quite apparent, and the difference is in the coefficients—pure partials in one case and functions of the statistics of ρ_0 and I_M in the other. For this simple problem the weighting function ω_1 has the form

$$\omega_1 = \frac{\left[\left(\frac{\partial f_\ell}{\partial \rho_1}\right)\sigma_1^2 + \left(\frac{\partial f_\ell}{\partial \rho_2}\right)\sigma_1\sigma_2 + \left(\frac{\partial f_\ell}{\partial \rho_3}\right)\sigma_1\sigma_3\right]}{\left[\left(\frac{\partial f_\ell}{\partial \rho_1}\right)\sigma_1 + \left(\frac{\partial f_\ell}{\partial \rho_2}\right)\sigma_2 + \left(\frac{\partial f_\ell}{\partial \rho_3}\right)\sigma_3\right]^2 + \sigma_M^2} \quad . \quad (2.5\text{-}8)$$

If we reduce the problem to one single constituent, ω_1 becomes

$$\frac{\left(\frac{\partial f_\ell}{\partial \rho_1}\right)\sigma_1^2}{\left(\frac{\partial f_\ell}{\partial \rho}\right)^2\sigma_1^2 + \sigma_M^2} \quad , \quad (2.5\text{-}9)$$

where σ_M^2 is the variance of the measurement noise, and σ_j is the RMS uncertainty of the j^{th} density. Finally, if the measurement noise is set equal to zero, the filter equation becomes

$$\rho_1 - \rho_1(0) = \frac{\partial \rho_1}{\partial f_\ell}\left(I_{M\ell} - I_{c\ell}\right) \quad , \quad (2.5\text{-}10)$$

which is identical to the linear equation case.

The filter equation set (2.5-6) is usually expressed in the form

$$\hat{\vec{x}}_k = \vec{x}_{k-1} + \vec{w}_{k-1}\left(I_{Mk} - I_{c,k-1}\right) \quad . \quad (2.5\text{-}11)$$

Here $\hat{\vec{x}}_k$ is called the optimal estimate of the atmospheric state given the measurement I_{Mk}, and w is the filter "gain" vector with elements like equation (2.5-8). The filter is recursive because after each measurement it reallocates the measurement deviation to each density and changes it appropriately. Then a new set of weighting factors (the so-called filter gains) and a new predicted intensity are computed by a numerical transfer simulation and matched against the next measurement, etc. Thus, given equation (2.5-3), the filter format of equation (2.5-4) and a radiative-transfer simulation, one can effectively convert measured intensities obtained during a horizon scan to a minimum-variance estimate of the densities of the constituents at each altitude layer. The practical application of this technique is discussed in detail in Section 3.1.

2.5.3 Inversion of Other Sources

Inversion of occulted starlight and airglow can be accomplished in the same way. The only difference is that the formulations of I_{cj} and $\partial f_j / \partial \rho_{ij}$ are much simpler because albedo and multiple scattering can be neglected.

2.6 EXPERIMENTAL DESIGN CHARACTERISTICS

2.6.1 Satellite Orbit Characteristics

Selection of satellite orbit characteristics is based on the meteorological and ecological requirement for global coverage and the maintenance of a local-hour angle for constituent parameterization. The orbit characteristics that satisfy these desired features are listed in Table 2.6-I. It may be noted that two of the orbital combinations specified in the Statement of Work fall within the baseline mission design (i.e., near-polar orbits in the 500-to-1000 km altitude range).

TABLE 2.6-I

AERONOMY SATELLITE ORBIT CHARACTERISTICS

Number of Orbits Per Day	Period (Min)	Altitude (km)	Altitude (nm)	Retrograde Inclination	Orbit Separation at Equator
13	110.769	1265.036	683.065	79.353	27.692
14	102.857	896.598	484.124	81.059	25.714
15	96.000	569.572	307.544	82.397	24.000
16	90.000	276.980	149.557	83.465	22.500

Earth Radius - 6378.165 km

The global coverage attainable from a 577-km and a 904-km near-polar orbit with a $\pm 25^{\circ}$ line-of-sight azimuth scan is illustrated in Fig. 2.6-1. Coverage under these conditions is adequate in the equatorial region for daily constituent-distribution identification, while in the polar regions, orbit-to-orbit coverage will provide more frequent updating. Figure 2.6-2 provides a typical star time line without sunangle limitations for stellar occultation and tracking, also for a 576-km near-polar orbit and a $\pm 25^{\circ}$ azimuth scan.

2.6.2 Satellite Attitude Requirements

The satellite attitude-stabilization requirements for attaining the desired line-of-sight position uncertainty are tabulated in Table 2.6-II.

TABLE 2.6-II

ATTITUDE-STABILIZATION REQUIREMENTS

Maximum Excursion	Pitch	$\leqslant 0.25°$
	Roll	$\leqslant 0.25°$
	Yaw	$\leqslant 0.25°$
Maximum Rates	Pitch	$\leqslant 0.015°$ /sec + orbit precession
	Roll	$\leqslant 0.015°$ /sec
	Yaw	$\leqslant 0.015°$ /sec
Attitude Position Uncertainty	Pitch	$\leqslant 0.01°$
	Roll	$\leqslant 0.01°$
	Yaw	$\leqslant 0.1°$

2.6.3 Engineering Design

In establishing the engineering design criteria for probing the stratosphere and mesosphere via a horizon scanning technique, one must first realize that each of the constituents—neutral atmospheric density, ozone, aerosols, and atomic oxygen—has been individually measured with varying degrees of success via rocket and aircraft techniques. Therefore, the Aeronomy Program objectives as stated—to measure these constituents systematically and simultaneously from a satellite—are not without precedence. The limb-scanning, single line-of-sight instrument which will sequentially perform the multispectral analysis of the scattered-sunlight photometer, star occultometer, and emission photometer, is to be governed by the considerations discussed in the following sections. These considerations encompass the basic instrument design philosophy of a two degree of freedom, limited motion, line of sight which is centrally aligned to the satellite's aft ground track and the earth's horizon.

2.6.3.1 Optical Considerations

Optical design considerations have been based on a diffraction-limited Cassegrainian telescope design with a 100-cm^2 entrance aperture. In addition, the optics are to be fitted with a two-stage external baffle and complementary internal baffling for reduction of off-axis scattering (i.e., improved altitude resolution of the constituent densities) as described more extensively in Section 3.4.1.

The field of view of the multispectral analyzer that forms the basis of the spectral measurements of the scattered-sunlight and emission photometer is 1.36 arc minutes by 136 arc minutes. In each case, the 100:1 aspect ratio is retained for constituent intensity enhancement without appreciable loss of vertical resolution. For the stellar occultometer, the field of view of the multispectral analyzer would be reduced to 1.36 arc minutes by 1.36 arc minutes, while the instantaneous field of view of the star tracker will be equal to or less than one arc minute.

Summarized, the scattered-sunlight photometer measurement data sets may be performed within 11^o of the sun for a signal-to-background ratio of

10^3 in the spectral range of 2000 to 7000 Å. Daytime stellar occultation measurements are limited, however, to 23° of the sun for a 10^3 signal-to-background ratio and to wavelengths less than 2600 Å due to horizon intensity background. These wavelength limitations are imposed as a function of occultation altitude where the stellar-to-horizon intensity ratio decreases below acceptable levels for data processing. Daytime emissions are similarly limited by horizon intensity background. The daytime emissions to be monitored have sun angle constraints for a 10^3 signal to a background ratio as follows: 18° for nitric oxide - [NO]; 50° for atomic oxygen - O[^{1}S]; and approximately 32° for nitrogen - N_2^+[1N] and N_2[2P].

2.6.3.2 Horizon Scan-Rate Considerations

The angular scan rates for the scattered-sunlight photometer and emission photometer are to be a maximum of one degree per second during mechanical scan measurement activities. However, design capability is to be retained for an orbit precession scan of the scattered-sunlight photometer and emission photometer, in a vertical offset star tracking mode. Stellar occultation measurements will be performed as the satellite normally precesses in its near-polar orbit.

2.6.3.3 Detector Considerations

Due to the low intensity levels and the wide dynamic ranges to be monitored in the multispectral analyzer section of the measurement instrument, a combination of photon-counting tube and photomultiplier appears to be the most desirable detector candidate. The spectral response of an extended ultraviolet S-20 photocathode with its high quantum efficiency is specified for this visible and ultraviolet application. Commercial photon-counting tubes and photomultipliers are presently available where photocathode dark counts of less than 20 and 125 photons per second respectively for gains of 10^6 are typical.

For the star-tracking section, an image dissector appears to be the most desirable detector candidate due to acquisition and an off-axis tracking requirement. Rugged image dissector tubes are presently available commercially with S-11 and S-20 photocathodes having applicable performance characteristics.

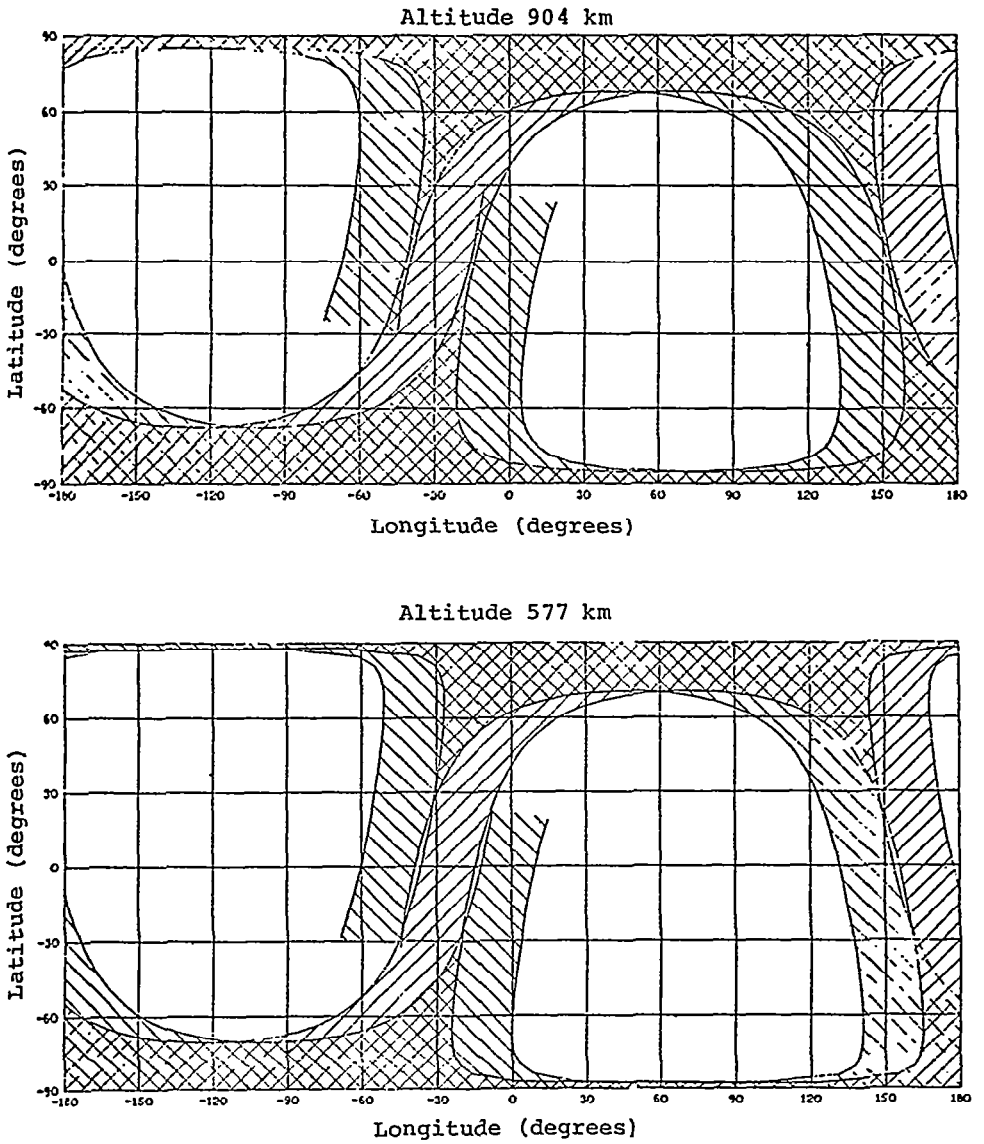

Fig. 2.6-1 Global orbit coverage for ±25° azimuth instrument scan angle. (Diagonal lines represent orbit coverage on each orbit. Crosshatched lines represent orbit coverage overlap on consecutive orbits.)

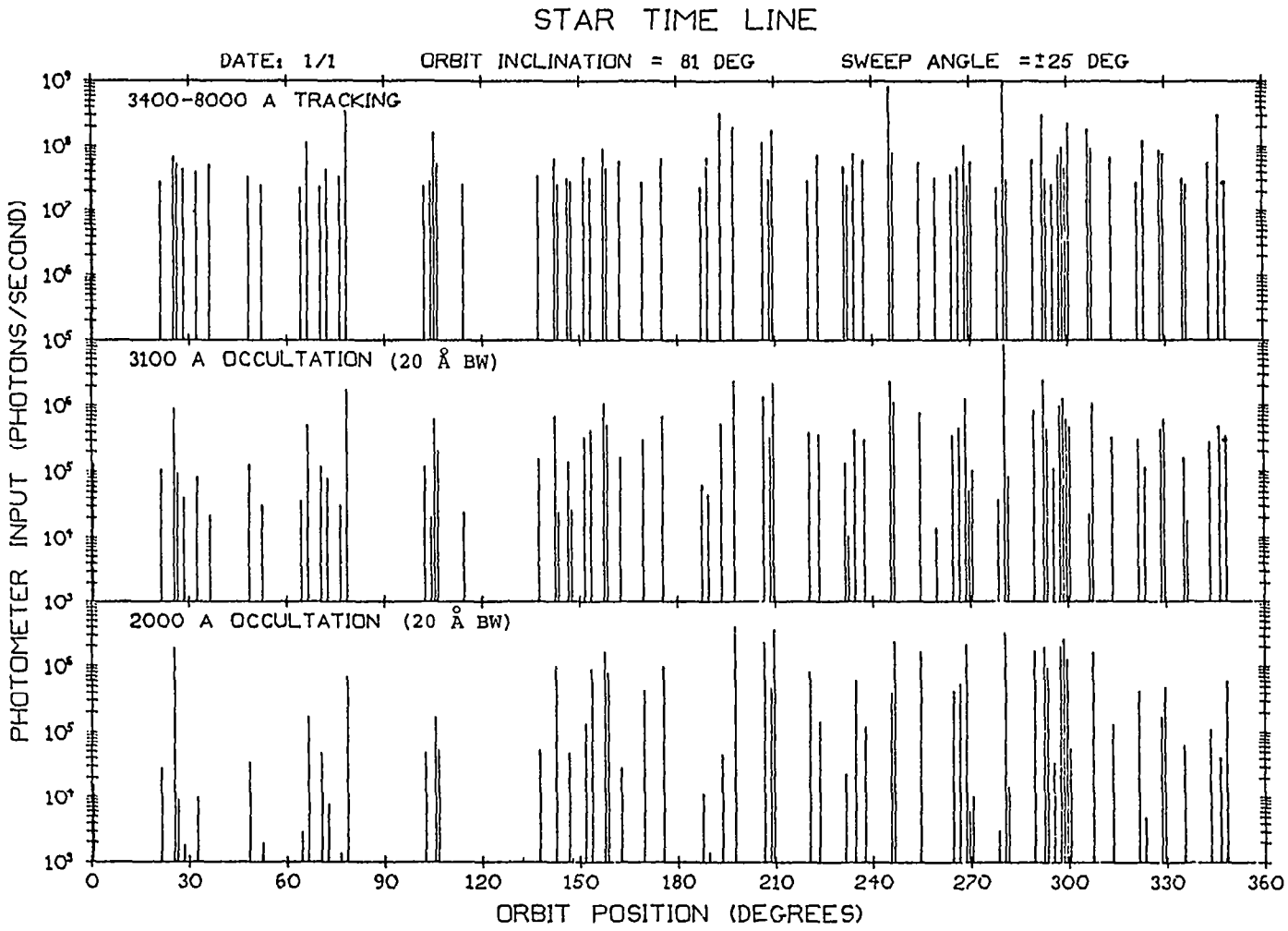

Fig. 2.6-2 Star time line without sun angle constraints.

2.7 SUMMARY

The MIT Aeronomy Program is a viable experiment whose uniqueness lies in its ability to determine simultaneously the vertical distribution of ozone, neutral atmospheric density and aerosols and airglow emissions in the stratosphere and mesosphere. Whether it be for meteorological or ecological application, the horizon-inversion technique of monitoring the constituent scattering, absorption and emission characteristics is an outstanding vehicle for environmental-probing. Through our work in the area of constituent identification, we have demonstrated the feasibility of horizon-inversion by scattered sunlight, stellar occultation, and emission techniques and their ultimate utility as the basis for a global-monitoring program.

During this experiment-feasibility phase, we have demonstrated that a scattered-sunlight photometer, stellar occultometer and emission photometer can be compatibly combined into a single line-of-sight optical instrument which will sequentially perform multispectral analysis for constituent identification by day or by night. Additionally, we have successfully demonstrated the inversion of measured data from simulated and actual flight data. For the scattered-sunlight inversion case, inversions of horizon measurement data have been shown to converge for the expected range of constituent density uncertainties, absolute altitude uncertainties and calibration errors. Ultimate limitations will be in our ability to accurately model the measurement inputs. In this area, significant theoretical advances in radiative-transfer modeling have been accomplished under the present contract.

From an engineering standpoint, there are no apparent design constraints. The system as designed is a practical application of present instrumentation technology. Each measurement technique has been successfully demonstrated separately in rocket or rocket-plane instrumentation. Only natural phenomena (such as aurora, South Atlantic anomaly radiation and the terminator) place potential measurement restrictions on data acquisition. However, these restrictions are themselves limited in extent.

There is no question in our minds about the need to make these stratospheric and mesospheric measurements, or about the desirability of a comprehensive satellite experiment that can obtain simultaneous multispectral measurements. For meteorological purposes these measurements are required to gain a better understanding of the energetics and dynamics of the upper atmosphere and its interaction with the lower atmosphere; to provide a climatology of the upper atmosphere; and to provide a data base for developing and verifying forecasting techniques. For ecological purposes, the observational program will provide a capability for measuring the vertical distribution of stratospheric and mesospheric aerosols, thereby providing baseline environmental-pollution measurements globally for international consumption.

3.0 AERONOMY TECHNICAL HIGHLIGHTS

3.1 SCATTERED SUNLIGHT INVERSION

3.1.1 Introduction

This section discusses the feasibility of determining the densities of air, ozone and aerosols in the atmosphere from limb measurements of scattered sunlight at various wavelengths. An extended Kalman-Bucy filter is used for the inversion and is applied to both real data (obtained from X-15 flights) and data simulated from a theoretical measurement model comprised of a radiative transfer model and an atmospheric model. The optimum measurement conditions (e.g., wavelength, altitude and zenith angle) which maximize the inversion accuracy for each constituent are presented; in addition, this section analyzes problems which resulted from inaccuracies in the measurement model, from poor a priori knowledge of the constituent densities, and from measurement biases.

3.1.2 The Radiative Transfer Model

The radiative transfer model used in the preliminary inversion analysis is a modified single scattering solution to the equation of radiative transfer which simulates the characteristics of a limb scan for a given set of optical conditions (ground albedo, sun zenith angle, wavelength, etc.). This model gives the radiance at the telescope as

$$h(m) = MS(m)\Big(1 + A(m)\Big) I(m) \qquad \frac{\mu watts}{cm^2\text{-}\mathring{A}\text{-}ster} \quad , \qquad (3.1\text{-}1)$$

where the measurement parameter (m) refers to a given tangent height (Fig. 2.2-1), wavelength and zenith angle.

I(m) is a single-scattering computation for the radiance produced at the scanning telescope due to the direct scattering of sunlight along a line of sight ξ.

$$I(m) = \int_{-\infty}^{L} J(\xi,m)\, e^{-\tau S(\xi,m)}\, e^{-\tau(\xi;L,m)}\, d\xi \quad . \qquad (3.1\text{-}2)$$

The terms contained in equations (3.1-1) and (3.1-2) are defined as follows:

ξ is zero at the tangent point and $d\xi$ is positive in the direction of the satellite.

$\tau S(\xi,m)$ is the optical thickness of the curved atmosphere (or air, ozone and aerosols) along the sun's ray path to the point ξ on the line of sight.

$\tau(\xi;L,m)$ is the optical thickness of the curved atmosphere from the point ξ on the line of sight to the telescope.

$J(\xi,m)$ is the scattering source term or radiance per unit length at the point along the line of sight. $J(\xi,m)$ is expressed as

$$J(\xi,m) = F(m)\sum_i P_i\left[\psi(m)\right]\kappa_i(m)\rho_i(\xi) \quad , \tag{3.1-3}$$

where $F(m)$ is the sun's irradiance; $P_i[\psi(m)]$ is the scattering phase function for the i^{th} constituent; $\kappa_i(m)$ is the scattering cross-section per molecule for the i^{th} constituent; and $\rho_i(\xi)$ is the molecular density of the i^{th} constituent.

$A(m)$ is the fractional increase in $I(m)$ due to sunlight which is scattered upward from the earth's surface.

$MS(m)$ is a multiple scattering correction function.

Typical horizon radiance profiles obtained with this radiative transfer model are shown in Figs. 3.1-1 and 3.1-2, corresponding to four values of zenith angle, a ground albedo of 0.2 and an MS factor of unity. The solar irradiances P (μwatts/cm^2-Å) used with each wavelength λ(Å) are listed below (Malchow, 1971):

λ	2600	2850	3100	3370	3914	5577	7000
P	1.3	3.15	6.89	10.81	10.98	16.95	13.69

A detailed description of this model is presented in Var, 1971.

3.1.3 Filter Description

In general, given measurements of a system, filtering theory is used to obtain the best estimate of the state of the system as well as the uncertainties (covariance) of that state. For linear systems with Gaussian white noise, it is possible to write the filtering equations in a discrete recursive form. The state of the system is represented by a vector (x) whose elements are parameters of the system. The measurements (y) are a function of the state, a measurement parameter (m), and white noise (u).

$$y(m) = h(x,m) + u \quad . \tag{3.1-4}$$

For the inversion of scattered light, the state vector elements are the densities (ρ_j) of constituents at specified altitudes.

$$x = [\underbrace{\rho_0,\ldots\rho_{n_1}}_{\text{Air}}, \underbrace{\rho_{n_1+1},\ldots\rho_{n_2}}_{\text{Ozone}}, \underbrace{\rho_{n_2+1},\ldots\rho_{n_3}}_{\text{Aerosols}}]$$

$$\equiv [x_j] \quad . \tag{3.1-5}$$

It has been assumed throughout the scattered sunlight studies (Merritt, 1971) that the only constituents which significantly affect the incident solar energy are (1) air molecules which are responsible for Rayleigh scattering, (2) ozone molecules which act as pure absorbers, and (3) aerosols which scatter incident light anisotropically.

The measurement equation (3.1-4) is modeled by an appropriate solution to the equation of radiative transfer—in this case, equation (3.1-1), with the understanding that h(m) h(x,m). The measurement model therefore includes an assumed atmospheric model, consisting of the vertical distributions of the constituent densities. The measurement parameter (m) in this case refers to a particular combination of tangent height and wavelength. From the measurement model we obtain a measurement vector B(m) defined by the row vector

$$B(m) = \left[\ldots, \frac{\partial h(m)}{\partial x_j}, \ldots \right] \quad . \tag{3.1-6}$$

In addition, a covariance matrix P is used in the inversion routine for describing the statistical behavior of the x_j.

In the following inversion analysis, P is initially assumed to be diagonal; that is, the densities for the initial estimate of the state vector are assumed to be uncorrelated and the variances are specified as a given fractional amount (a) of the expected value of the constituent densities (x):

$$P_0 = \begin{pmatrix} \ddots & & 0 \\ & (a\bar{x}_j)^2 & \\ 0 & & \ddots \end{pmatrix} \tag{3.1-7}$$

The following steps are then used to update recursively the estimate of the state (x) and its covariance (P) with each successive measurement y(m).

(1) Calculate the filter gain column-vector (K) from the present covariance matrix (P), the theoretical measurement vector B(m), and the measurement noise covariance (R).

$$K(m+1) = P(m)B(m+1)^T(B(m+1)P(m)B(m+1)^T + R)^{-1} \quad . \tag{3.1-8}$$

(2) Incorporate the next measurement y(m+1) in the next update of the estimate of x.

$$x(m+1) = x(m) + K(m+1)[y(m+1) - h(x,m+1)] \quad . \tag{3.1-9}$$

(3) Update the covariance matrix

$$P(m+1) = P(m) + K(m+1)B(m+1)P(m) \quad . \tag{3.1-10}$$

The above recursive filter will converge and yield the best estimate of the state vector and the corresponding covariance matrix if the following conditions prevail: (1) the initial estimate of x is sufficiently close to the actual answer and the differences between measured and computed intensities are linearly related to the differences between the actual and estimated state vector; (2) the measurement model is accurate; and (3) no fixed biases are present in the measuring process.

When any of these conditions are not met the updates of the state vector given by equation (3.1-9) will be inaccurate, but this inaccuracy will not be correctly reflected in the updates of the covariance matrix given by equation (3.1-10) since the covariance matrix naturally converges to smaller values as successive measurements are processed; the addition of reliable information hypothetically yields smaller uncertainties. Since the convergence of the covariance matrix reduces the gain given by equation (3.1-8), successive updates of the state vector are insufficient to overcome large initial errors in the estimate of the state vector. In this sense, the state vector diverges from the best estimate of the actual state.

In general, it is possible to develop special techniques and modifications which extend the range of the filter and prevent the estimate of the state vector from diverging even when significant exceptions to the above conditions are encountered.

Although numerous techniques have been reported for extending the range of convergence of recursive filters, these are generally related to the unique behavior characteristics of the particular system being considered. No simple procedure exists for optimizing the range of filter convergence for all physical systems. Extensive simulation of the system and the filter is necessary to determine the best modification of the filter to insure convergence when exceptions to the above conditions are present. A large variety of techniques were applied to the scattered light inversion problem, and those which worked are described below.

The most important problem studied related to the basic nonlinearity of the system. This nonlinearity is clearly anticipated by inspection of the measurement equation (3.1-1). The direct application of the above filter to the inversion of scattered sunlight should be expected to lead to large errors in the updates of the state vector when the measured and computed intensities differ appreciably. Indeed, early simulations showed that the filter diverged when the initial estimate of the densities was more than 20 percent from the actual state. Since most constituents are not known to that degree of accuracy, it was necessary to extend the range of the existing filter. This was accomplished by applying a damping factor to the filter gain, thus minimizing the absolute value of the error due to nonlinearity in each update of the estimate of the state while maintaining the covariance matrix at a reasonably large value. At the cost of slower convergence, this technique yielded significantly greater accuracy, causing the filter to converge when the initial estimate of all densities erred by 300 percent.

Recent work has shown that the range of the filter can be extended even further by changing the state variables. By utilizing the log of the densities as the elements of the state the sensitivity of the new measurement vector to changes in the densities is reduced and hence the system is effectively more linear. Employing the new state variables in conjunction with the damping factor on the gain causes the filter to converge even when the initial estimate is in error by an order of magnitude or more. Although the full potential of this filter has not yet been determined, it is clear that it will easily handle the types of variations found in the atmosphere.

The problem of model inaccuracy was studied for the particular case of erroneous and coarse simulations of the real world densities. The simulated "real world" density distributions correspond to the typical reference density profiles (Fig. 3.1-3). The density distributions given to the filter, however, were exponential with constant scale heights between selected breakpoints spaced from 5 km to 20 km apart. The optimum choice of breakpoints for minimizing inversion time depends on the real world distribution assumed for each particular constituent. For example, the ozone profile requires a tighter spacing about its peak at 30 km than it does above 40 km where it truly behaves exponentially. To prevent the filter from converging prematurely on a particular segment of the state vector before establishing the remainder of the density profile, it was necessary to incorporate a form of global iteration on the data. Rather than sampling the tangent-height data sequentially, the data was sampled in coarse intervals repeatedly. For example, instead of incorporating measurements in an order such as 80, 79, 78, 77 ..., the data is sampled at 80, 70, 60 ..., and then 79, 69, 59 ..., etc. This technique has the desired effect of adjusting the entire state vector as a unit.

Other model inaccuracies, such as errors in the radiative transfer model, density distribution errors, ground-albedo errors and cloud errors, can be handled only by studying their effect on the convergence of the state vector. Until these secondary problem areas have been accurately modeled, final estimates of the state accuracy element cannot be made.

The problem of biased measurements was studied for the particular problem of an error in tangent height. The most effective way to deal with this type of problem is to incorporate an estimate of the bias as an element of the state vector. The filter then estimates not only the constituent densities but the tangent height bias as well. The success of this technique depends on the a priori statistics attributed to both the densities and the tangent height bias. If the densities are assumed to be well known, then the filter gain will emphasize the bias term; the converse is equally true. This technique has proven reasonably effective in simulated calculations. Details of the specific inversion results are presented in Section 3.1.5.

3.1.4 Sensitivity Analysis

Since the light scattering and absorbing properties of the constituent densities are wavelength-dependent, it might be expected that certain wavelengths are better suited than others for estimating particular constituents. For example, wavelengths about the ozone absorption peaks are best suited

for determining ozone concentrations. It would also be expected that wavelengths which are highly attenuated and do not penetrate deeply into the atmosphere will not yield information about constituent densities near the ground.

Sensitivity is a function derived from the filter equations, which indicates the relative information content from constituent to constituent and altitude to altitude for every measurement condition (i.e. wavelength and tangent height). Given a measurement, the information content for a particular constituent and altitude (state element) is reflected in a decrease in the variance associated with that element and it is natural to look at the covariance update equation for the definition of sensitivity:

$$P(m+1) = P(m) - K(m+1)B(m+1)P(m) \qquad (3.1\text{-}11)$$

the term of interest here is K(m+1)B(m+1)P(m), which is the decrease in the covariance for a particular measurement condition. Normalizing by P(m) yields the sensitivity matrix K(m+1)B(m+1). Of particular interest in the sensitivity matrix are the diagonal elements which indicate the relative decrease in variance of the elements of the state vector. To isolate the effects of the measurement vector on the sensitivity, the covariance is assumed to maintain its initial value. With this assumption the sensitivity of the jth element of the state vector is

$$s_j(m) = \frac{\partial y(m)\,\bar{x}_j}{\partial x_j}^2 \quad \Sigma_i \quad \frac{\partial y(m)\,\bar{x}_i}{\partial x_i}^2 + R \quad . \qquad (3.1\text{-}12)$$

For the purposes of the sensitivity analysis, the state vector is assumed to be defined at 1-km intervals. Figure 3.1-4 is an example of a plot of sensitivity versus altitude for neutral atmospheric density, ozone and aerosols at a tangent height of 40 km and at wavelengths of 2500, 4000, and 7000 Å. These curves indicate that wavelengths around the ozone peak (2500 Å) do not penetrate below 50 km, whereas the longer wavelengths (4000 and 7000 Å) which are attenuated less by ozone have a peak sensitivity at the tangent height. This figure also indicates that 4000 Å is the optimal wavelength for determining neutral atmospheric density at 40 km, whereas 7000 Å is the optimal wavelength for aerosols.

Since the peak sensitivity usually occurs at the tangent height, it is convenient to analyze a complete limb scan by plotting sensitivity vs. tangent height for the three constituents at various wavelengths. Fig. 3.1-5 shows the distributions of the peak values of the sensitivity for each constituent as a function of wavelength and measurement tangent height for several values of the sun's zenith angle. The sun's azimuth angle is assumed to be zero (coplanar) and the zenith angle is defined relative to an earth radius vector which is normal to the line of sight. A zenith angle of 90° means that the telescope is pointed directly at the sun.

In Fig. 3.1-5, the relative invariance of the ozone sensitivity profile to changes in zenith angle is due to the fact that ozone is an absorptive constituent. The large variation in the aerosol and neutral sensitivities with zenith angle reflects, therefore, the relative changes in the scattering phase functions for air and the aerosols assumed in the measurement model.

in the updates of the state vector w

The peak in aerosol sensitivity around 20 km is related to the large concentration of aerosols between 35 and 20 km assumed in our atmospheric model (see Fig. 3.1-3). If ozone and aerosols had been neglected in the measurement model, the penetration altitudes for the neutral or Rayleigh constituents would continue to decrease with increasing wavelength, because of the λ^{-4} dependence of the Rayleigh scattering cross section and the exponential distribution of neutral density. The presence of a strong ozone-absorption peak at 2550 Å, however, accounts for the general increase in penetration altitude as wavelength decreases below approximately 4000 Å or increases above 2000 Å toward the peak at 2550 Å.

By examining sensitivity profiles one can predict the altitude ranges over which the inversion accuracy will be greatest for each constituent. Thus one is able to design flight hardware with the minimum number of wavelengths for an optumum (after the fact) inversion of all constituents.

3.1.5 Selected Results

To adequately assess the performance of the horizon-inversion technique, a sequence of simulations was conducted. These simulations were performed to determine whether or not the inversion is performed adequately, since in a simulation—unlike in the real experimental case—the actual value of the state is known beforehand. Therefore, if the actual value of the state falls within the rms limits about the final estimate of the state, the inversion has succeeded. Many simulations have been performed, and they indicate that bias errors, nonlinearities and selected modeling errors can be adequately accommodated.

In each of the following simulations the initial estimate of the state was based on the reference densities in Figure 3.1-3 (Malchow, 1971). The simulated measurements, however, were created from density distributions that were grossly perturbed from the standards (Perturbed Reference State). To these measurements was added an arbitrarily chosen Gaussian white noise of 0.00001 μwatts (cm^2-Å-steradian). The final covariance values in the following simulations are functionally dependent on the gain-damping factor, spatial separation of scan altitudes chosen, and the wavelengths used. These final covariance values reflect the accuracy obtainable when the transfer model is an accurate representation of the atmosphere and the instrument has no unfilterable biases. The Perturbed Reference State (those densities used to create the simulated measurements) is represented by a dotted line in the simulation results. The two solid lines represent the rms limits centered about the final estimate of the state generated by the inversion routine. Noted is the Perturbed Reference State which in general falls with the rms limits about the estimate state indicating that the inversion routine performs well under each of the simulated measurement conditions.

Figure 3.1-6 shows the results of an inversion in which the simulated measurements were computed from density curves obtained by adding a sinusoidal contribution to all the standard densities. The sinusoid has a period of 70 km and a peak value of 70 percent of the value of the particular constituent. The scan heights were spaced approximately 1.5 km apart, the gain was damped

by a factor of three, and wavelengths of 2550, 4000, 5500, and 7000 Å were used in the inversion. This example illustrates the success of the modified global-iteration technique. Without this technique, the neutral density profile would oscillate wildly about the actual densities; with this technique, however, the filter finds a good fit to the data.

Figure 3.1-7 shows the results of an inversion in which a 60-percent anomalous aerosol layer was added at 40 km, and a 20-percent bias was added to neutral and ozone densities. Again, the scan heights were spaced approximately 1.5 km apart, but the gain was damped by a factor of two and the wavelengths 3000, 4000, 5000, 6000, and 7000 Å were used in the inversion. This example shows that the inversion routine can detect local aerosol layers. It also shows that the final covariance values for ozone are smallest between 40 and 60 km and largest below 35 km. This can be seen to correlate well with the sensitivity curves discussed previously.

Figure 3.1-8 shows the results of an inversion in which a bias of 70 percent was added to all the constituents. This problem used the same measurement-inversion schedule as the preceding problem and again illustrates how the final covariance values are correlated to the sensitivity curves.

Actual limb-scan data (Fig. 3.1-9) were obtained from an experiment conducted by MIT for the original purpose of defining the horizon for navigation (Gray, 1969). A photometer was mounted in the tail of the X-15-1 aircraft and flown to a height of approximately 80 km, where a number of limb scans were taken of the horizon. The scans at different wavelengths were performed sequentially as the X-15-1 was flying, causing some loss of correlation between scans with regard to relative tangent-height positioning and cloud cover. The wavelengths were chosen for the scans on the basis of navigation criteria, rather than inversion criteria; however, the sensitivity curves show that the chosen wavelengths of 3500, 3800, 4200, 5800, and 7000 Å will yield information about neutral density and aerosols. As mentioned previously, the transfer model presently incorporated in the inversion routine has only a crude approximation of multiple-scattering effects, but the filter nevertheless processed the data, with the final results shown in Fig. 3.1-10.

The data start at a tangent height of approximately 60 km and continue down to 15 km (below which level clouds significantly affect the signal). Confidence in the accuracy of these final results can be acquired by comparing the inversion estimate of neutral density with a reference value of neutral density, which is a good base line, since neutral density at all altitudes falls within the rms limits about the inversion estimate, indicating that the inversion estimates of neutral density and also therefore of the other constituents are accurate to within their predicted rms limits. The rms limits are large, in this case, because of the assumed large noise level and gain-damping factor, and because of the poor quality of these data and the modeling errors inherent in the single-scattering transfer model. The two aerosol layers at 25 and 50 km are both real; although the rms values are large (0.5 orders of magnitude at 25 km and 0.8 orders of magnitude at 50 km), the estimated increases are even larger (0.7 orders of magnitude at 25 km and 1.2 orders of magnitude at 50 km). These two layers can both be seen in the raw data as increases in

X-15-1 horizon data at 5800 and 7000 Å. This 50-km layer is in general agreement with the layer recently measured (Rossler, 1968) by a rocket-borne sensor at that altitude, and with the layer suggested by satellite measurements (Elliott, 1971, and Merritt, 1971) of an anomalous increase in the backscattered ultraviolet intensity.

The ultimate inversion accuracy obtainable from a limb-scan experiment lies somewhere between the near-perfect results of the simulations and the errors in the results of the X-15-1 data. As has been stated above, the X-15 error is due to the quality of both the data and the transfer model. In the final analysis, the accuracies in these two areas will define the ultimate limitations on inversion accuracy. To the transfer model, the single-scattering model is accurate in its behavior, but it fails to give the correct absolute values of intensity.

The single-scattering model is consistently in error by a certain fraction which is due to multiple scattering; a good multiple-scattering model, when operational in the inversion routine, will greatly improve the accuracy in this area. Regarding data accuracy, the sequential nature of each wavelength scan and lack of correlation between wavelengths—coupled with a relatively poor estimate of the actual scan heights—make the X-15-1 data an absolute worst case. The final Aeronomy instrument package to be flown will generate all of the wavelengths simultaneously, giving exact correlation point by point between the wavelengths, in addition to having an absolute uncertainty of only 1 km in the scan height. Although impossible to estimate final absolute accuracy, it does not seem unreasonable to foresee that a multiple-scattering model and wavelength-to-wavelength correlated data will result in an order-of-magnitude improvement over the X-15-1 experiment.

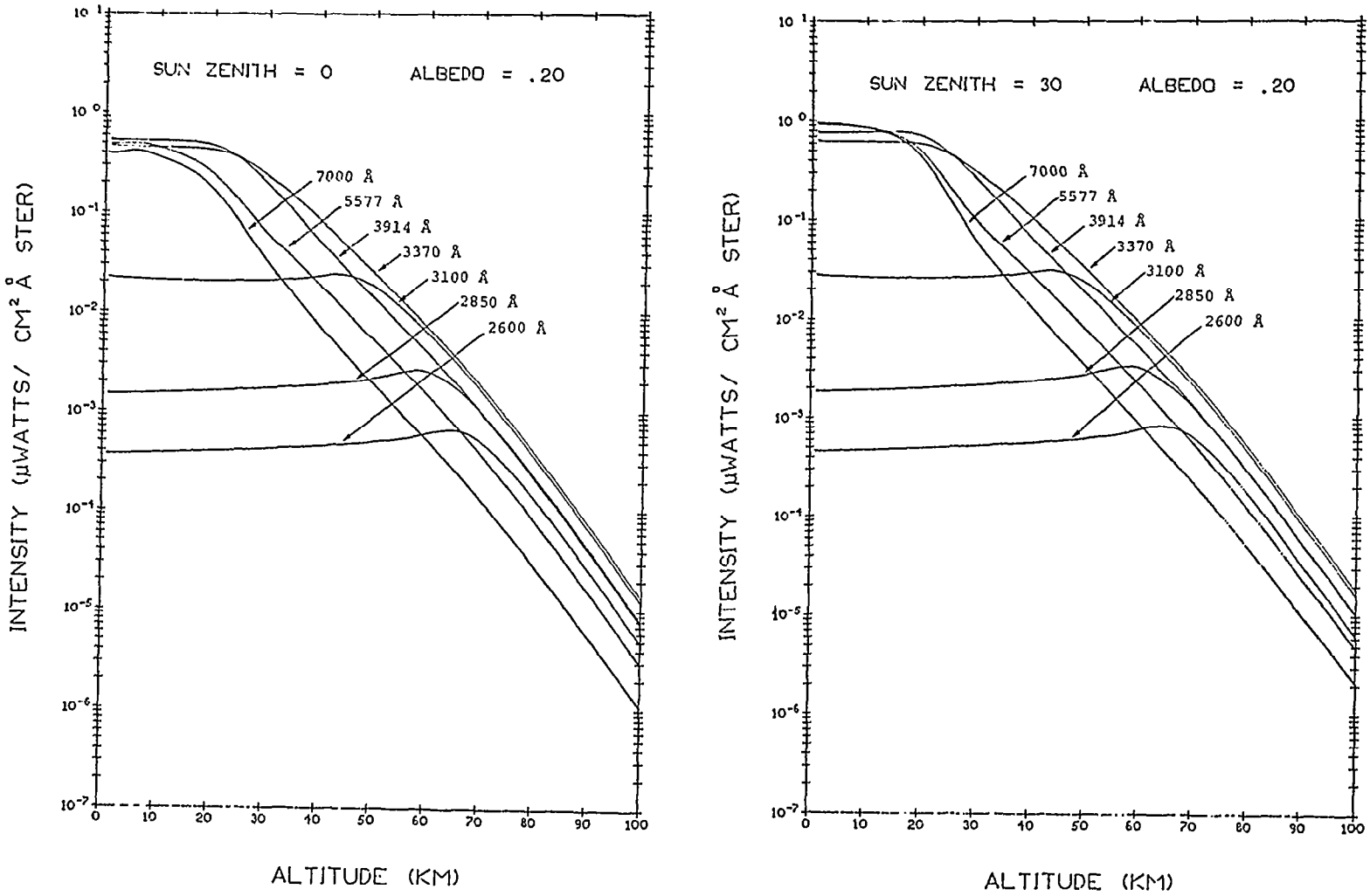

Fig. 3.1-1 Horizon Radiance Profile (Sun Zenith = 0°, 30°)

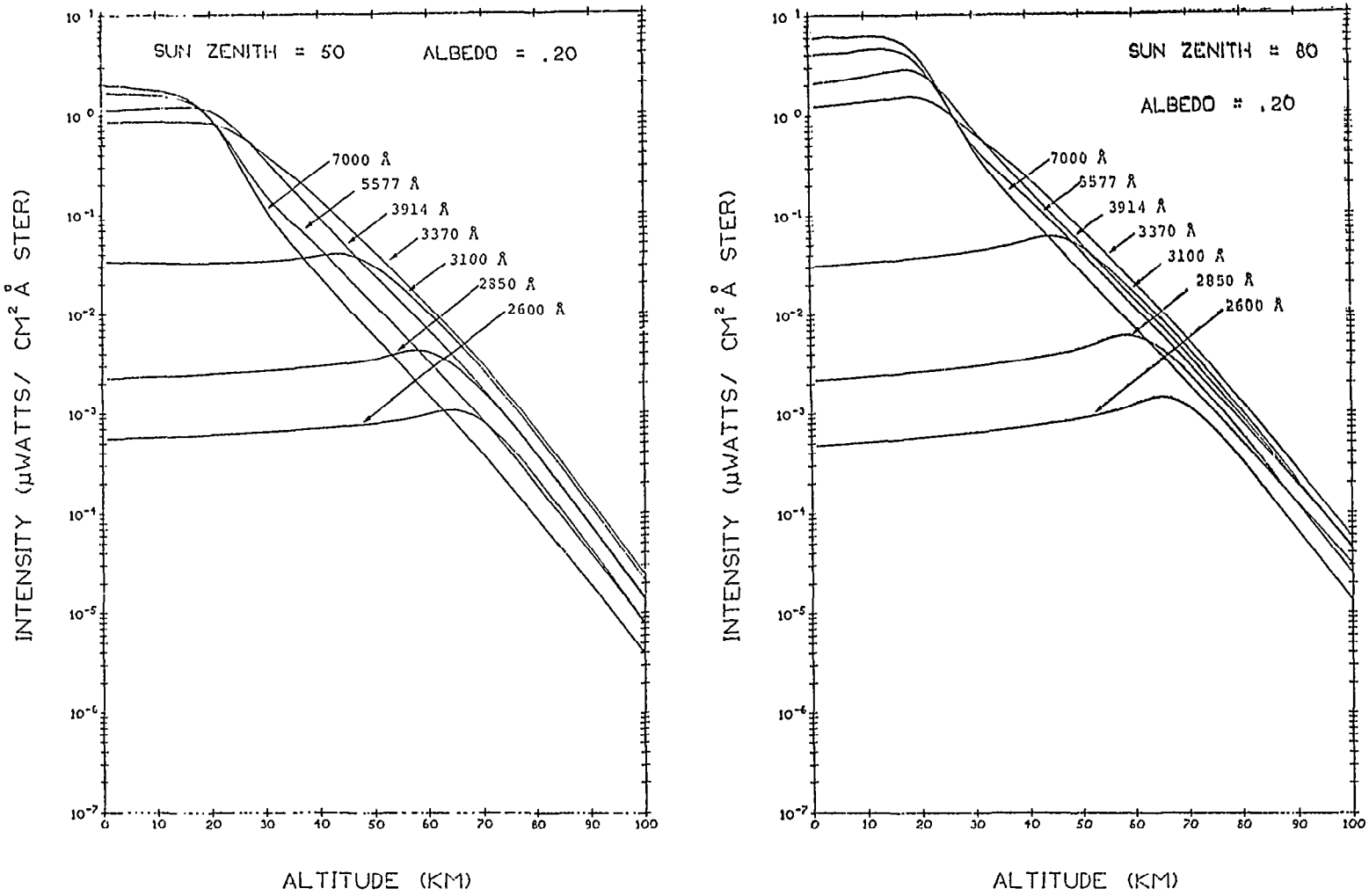

Fig. 3.1-2 Horizon Radiance Profile (Sun Zenith = 50°, 80°)

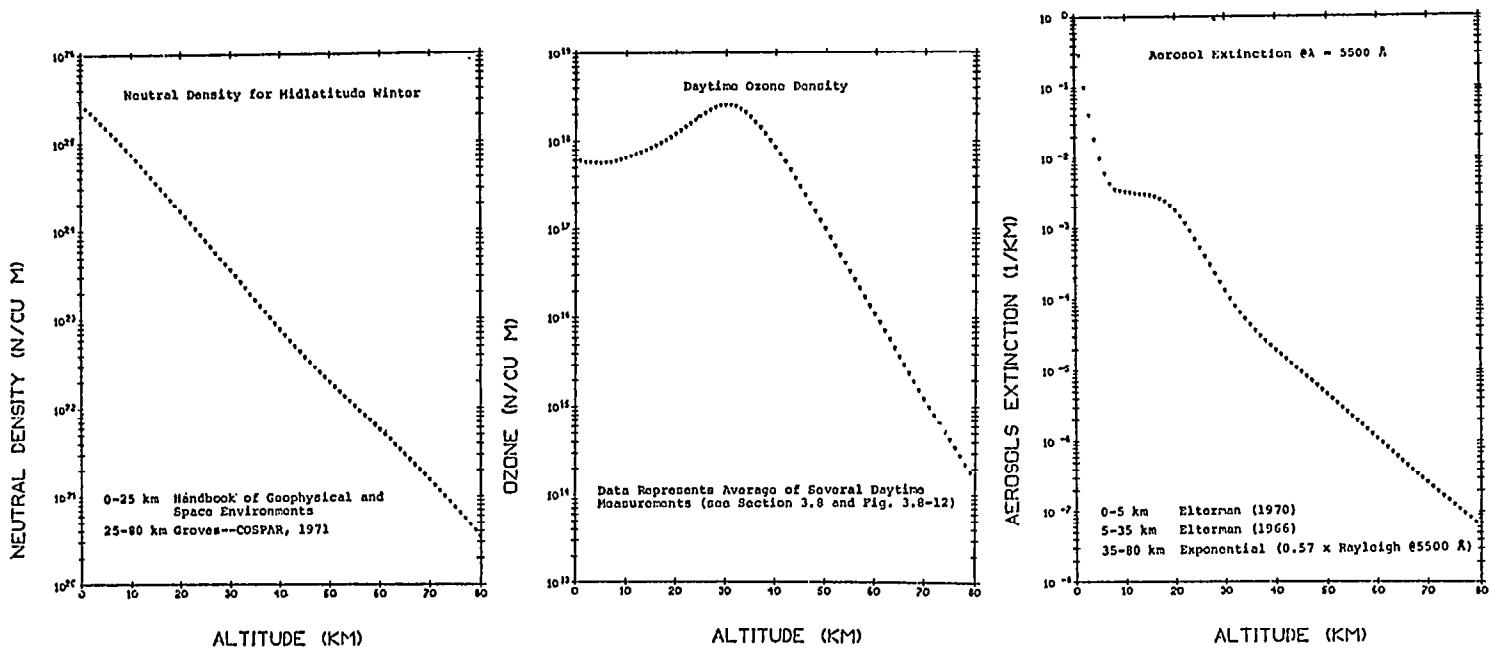

Fig. 3.1-3 Reference Density and Extinction Profiles for Neutral Density, Ozone and Aerosols

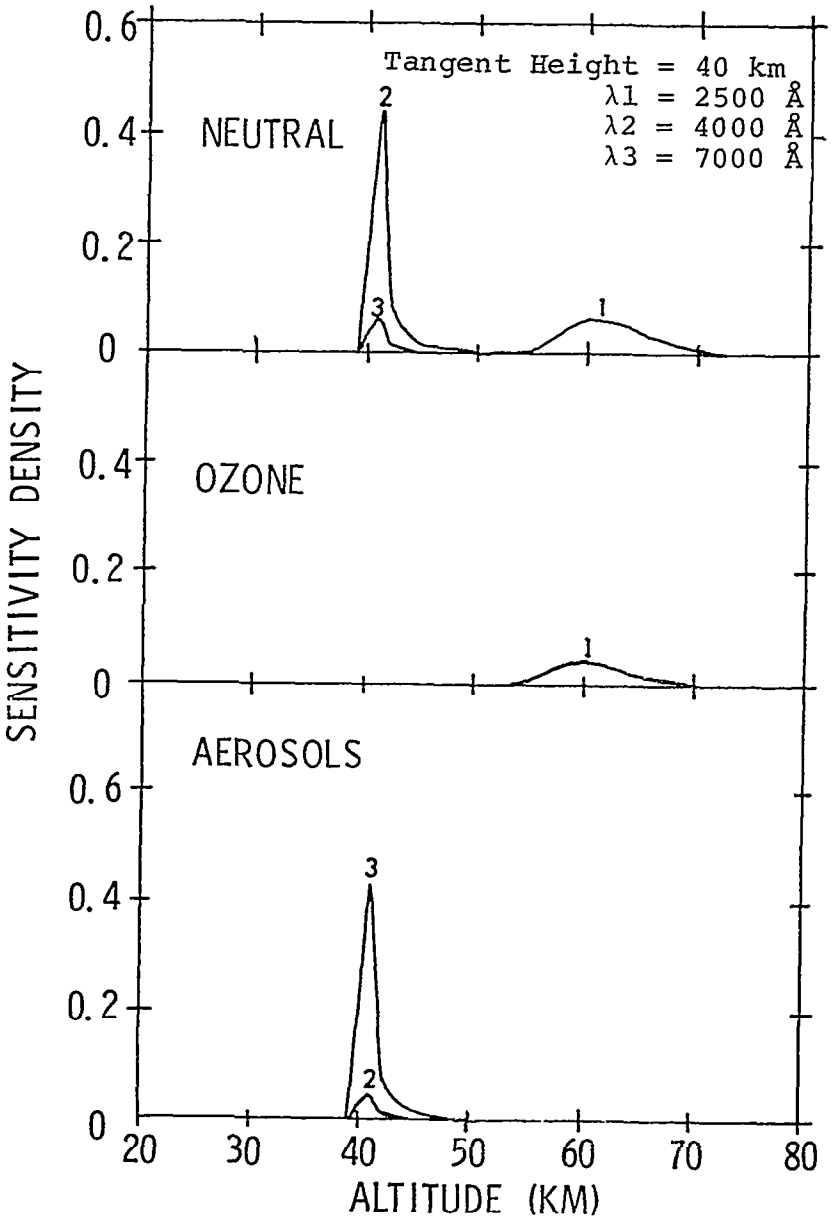

Fig. 3.1-4 Horizon-Inversion Sensitivity -- 40-km Tangent Height Distribution

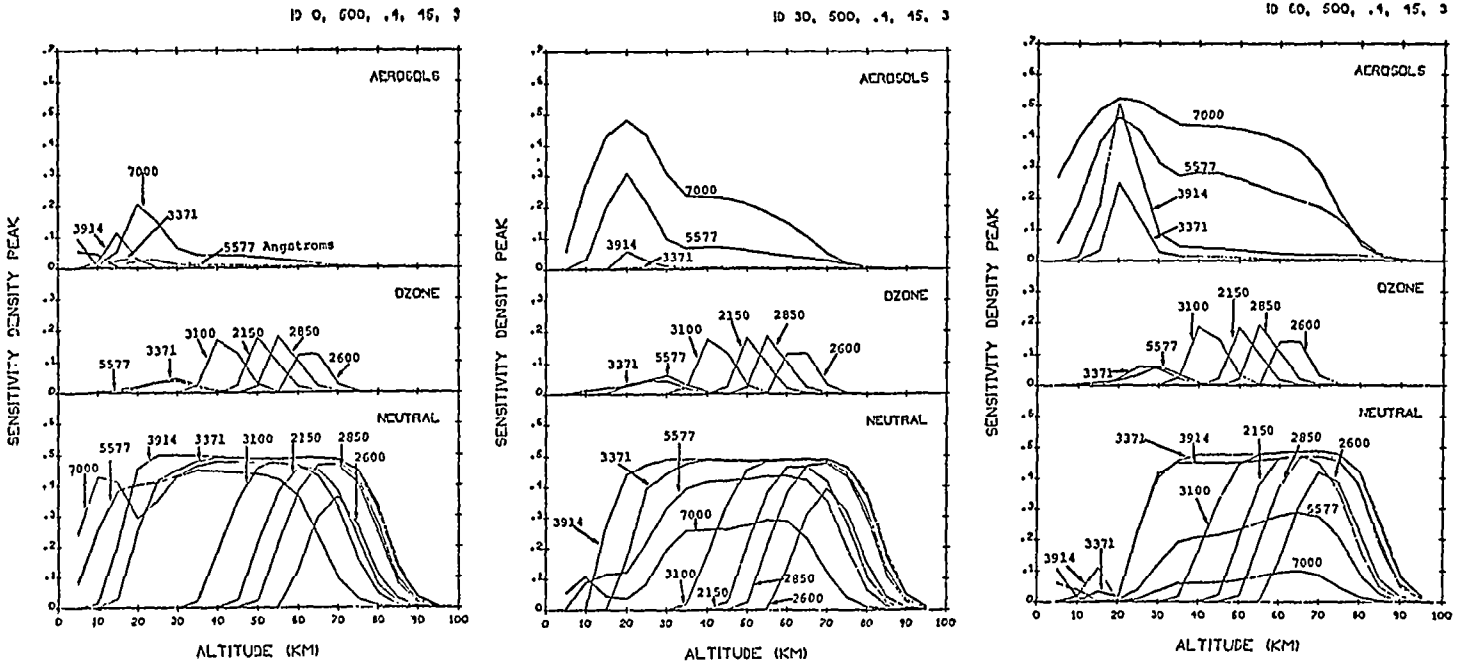

Fig. 3.1-5 Scattered Sunlight Constituent Peak Sensitivity Profiles
(Zenith Angle = 0°, 30°, 60°--left to right)

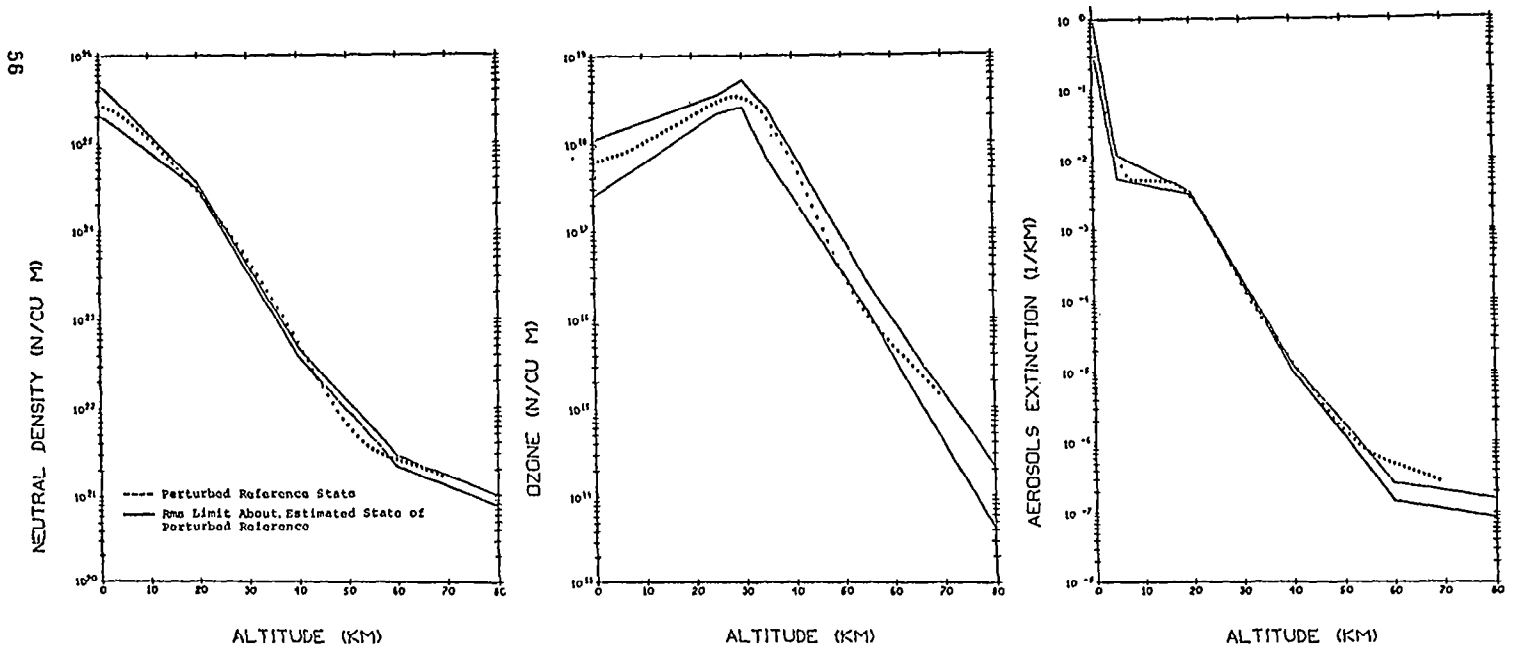

Fig. 3.1-6 Simulation Results--Scattered Sunlight Inversion of 70% Sinusoidal Bias to Reference Neutral Atmospheric Density, Ozone and Aerosols.

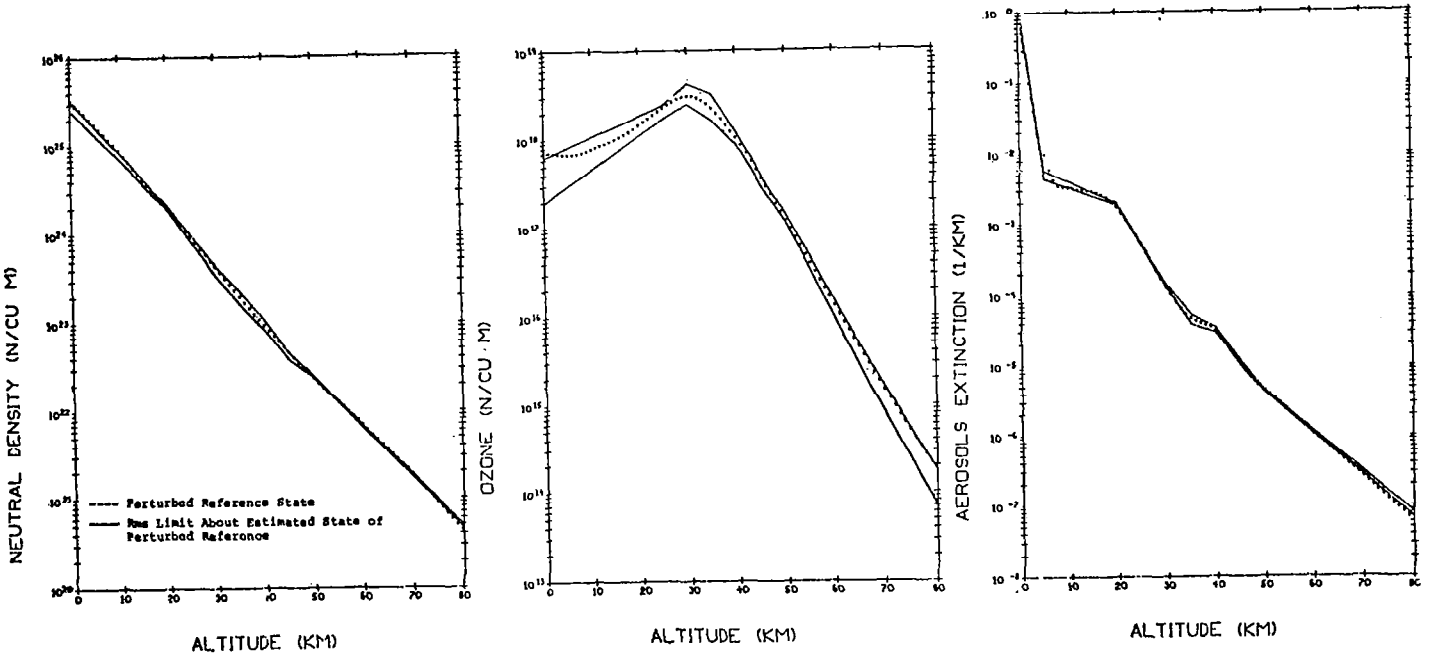

Fig. 3.1-7 Simulation Results--Scattered Sunlight Inversion of +20% Bias of Neutral Atmospheric Density and Ozone and 60% Anomalous Aerosol Layer at 40 km.

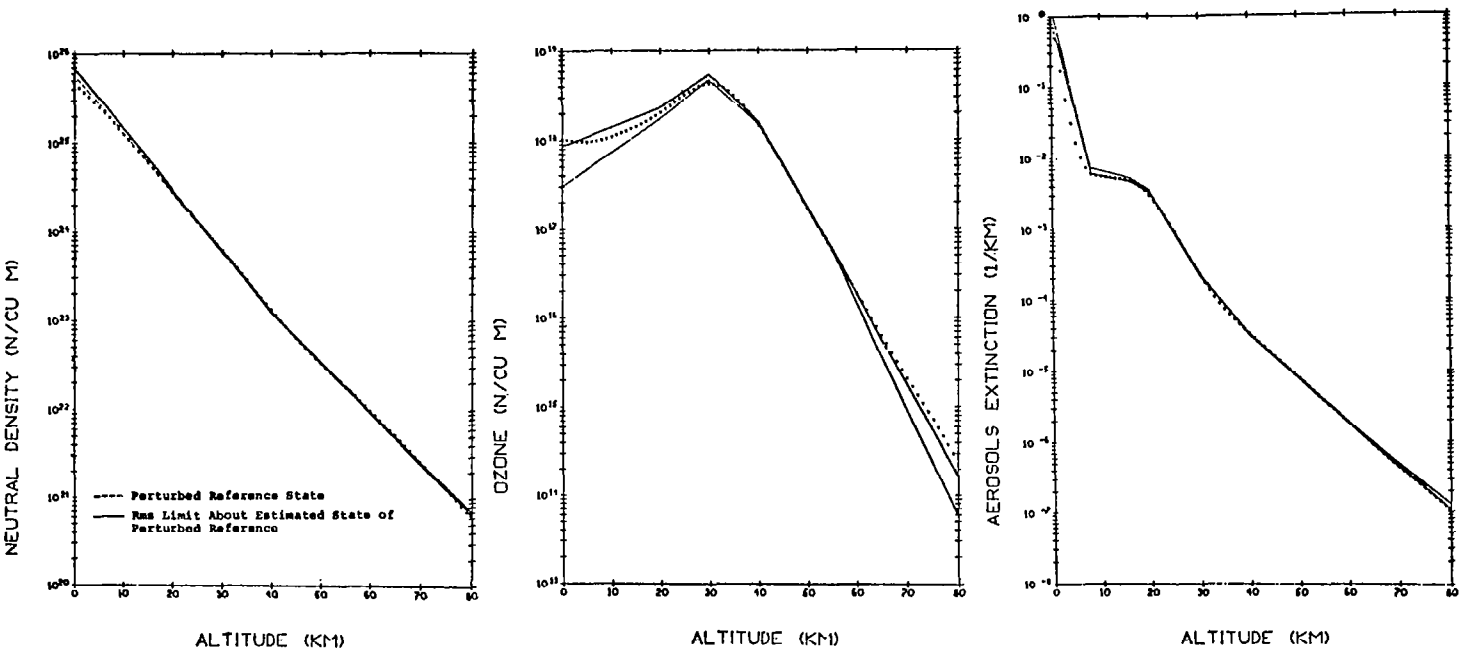

Fig. 3.1-8 Simulation Results--Scattered Sunlight Inversion of +70% Bias of Neutral Atmospheric Density, Ozone and Aerosols.

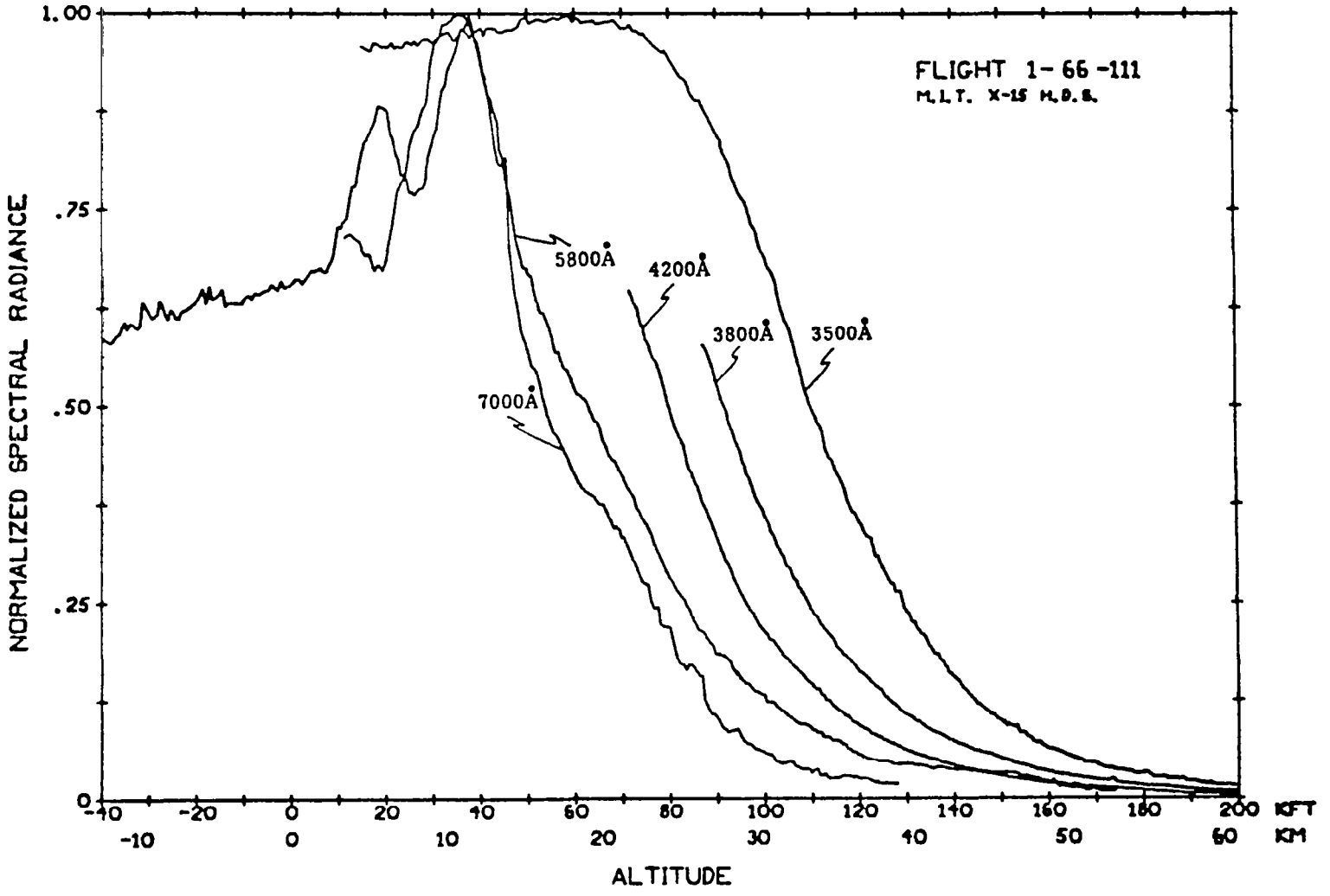

Fig. 3.1-9 Normalized Spectral Radiance Profiles, X-15-1 Flight 1-66-111

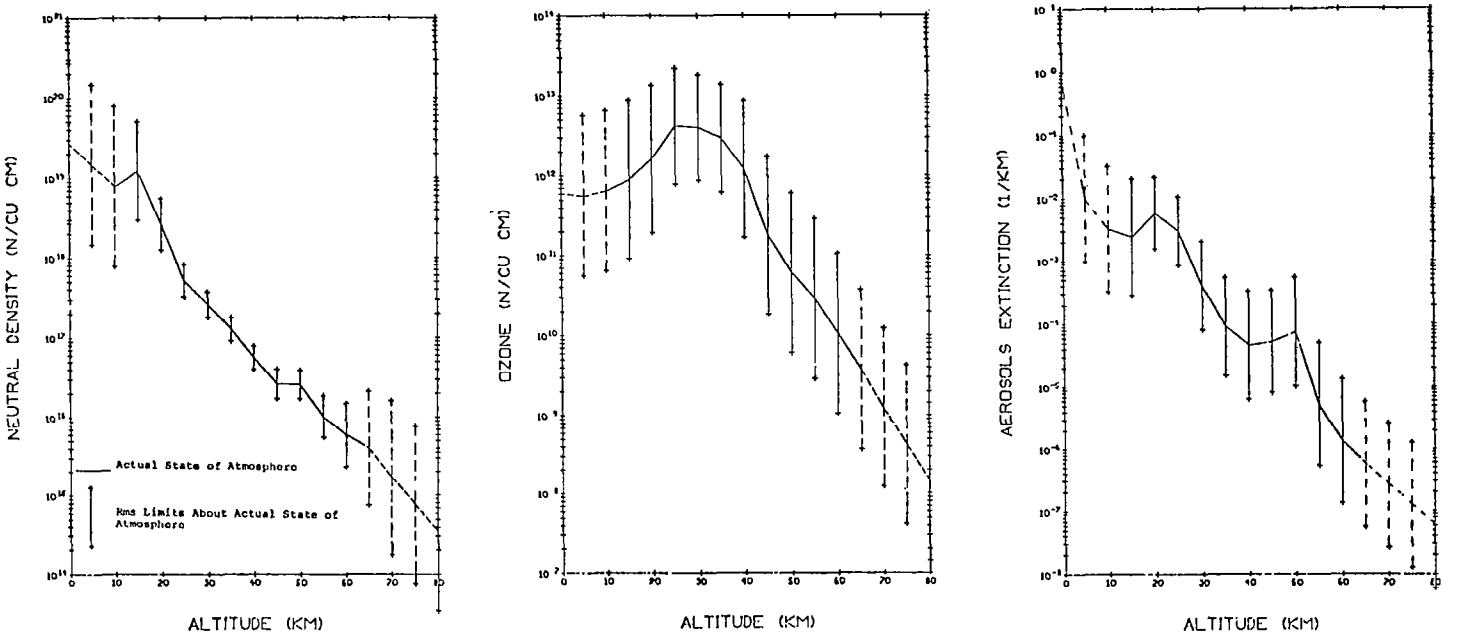

Fig. 3.1-10 Experimental Results--Scattered Sunlight Inversion of X-15-1, Flight 1-66-111.

References for Section 3.1

Elliott, D. D., "Effect of High Altitude (50 km) Aerosol Layer on Topside Ozone Sounding", Space Res. XI, North Holland Publishing Co., 1971.

Gray, C. R., MIT/IL X-15 Horizon Definition Experiment Final Report, Apollo Guidance and Navigation, MIT Instrumentation Laboratory, R-648, October, 1969.

Malchow, H. L., "Standard Models of Atmospheric Constituents and Radiative Phenomena for Inversion Simulation", Internal Report No. AER 7-1, January, 1971.

Merritt, D. C., "The Application of a Linear Recursive Filter to Nadir Ultraviolet Inversion", Internal Report No. AER 11-2, April, 1971.

———, "The Estimation of Atmospheric Constituent Densities Through the Inversion of Scattered Sunlight Measurements", Internal Report No. AER 8-7, August, 1971.

Rossler, F., "The Aerosol Layer in the Stratosphere", Space Res. VIII, North Holland Publishing Co., 1968.

Var, R. E., "A Hybrid Algorithm for Computing Scattered Sunlight Horizon Profiles", Internal Report No. AER 7-3, April, 1971.

3.2 STELLAR OCCULTATION INVERSION

3.2.1 Introduction

The problem of inverting the residual signal of a star undergoing occultation has many features in common with the scattered-sunlight problem discussed in Section 3.1. The same filter equations are used, and one is faced with the same sensitivity analysis problem. The two inversion procedures are virtually identical, but several operational differences are apparent. The starlight signal levels are much lower than the scattered sunlight signal levels. Thus, star occultation is useful mainly at night. Also, the detected signal is dominated by radiation directly from the source, rather than radiation that is at least singly scattered. This leads to sensitivities to given constituents at given altitudes different from those in the scattered-sunlight case. Finally, spectral differences between stars generally lead to selection of different wavelength intervals to optimize constituent detection.

The occultation geometry illustrated in Fig. 3.2-1 is based on the assumption that the star is in the orbital plane, although, in general, this will not be the case, since many useful stars will not necessarily fall in the orbital plane. From the figure it can be seen that as the satellite rotates about the earth, the tangent height of the line of sight decreases and an entire scan of the limb is obtained.

3.2.2 Transfer Model

Since there are no sources inside the atmosphere, the transfer equation can be reduced to the case of pure attenuation, i.e.,

$$I_m = I_s e^{-\tau} \quad , \tag{3.2-1}$$

where I_s is the star irradiance and I_m is the measured irradiance. The modeling problem therefore reduces to computing the optical depth τ over the receiver line of sight. This is done by assigning a layer structure to the atmosphere with divisions sufficiently fine that τ is expressible in the form

$$\tau = \sum_{i=1}^{n} \sum_{j=1}^{m} k_j \rho_{ij} \Delta x_i \quad , \tag{3.2-2}$$

with k_j equal to the absorption or scattering cross section of the k^{th} constituent, ρ_{ij} the density, and Δx_i the length of the line of sight through a layer.

Figure 3.2-2 shows the results of a simulated set of occultation scans for a star of magnitude (-1.6) and color temperature of 11200°K, with the wavelengths that will probably be flown in the actual occultation experiment. The depth to which the starlight penetrates the atmosphere is a function of the optical depth of the atmosphere at that wavelength. For example, at 1900 Å the atmosphere is optically thick due to molecular oxygen absorption, and the starlight is reduced by two orders of magnitude at a tangent height of 75 km. At 3914 Å, however, the atmosphere is relatively thin optically and the

starlight penetrates well below 20 km. This varying effect of wavelength on the occultation curves is the basis of the inversion routine.

3.2.3 Estimation

Estimating the density profile requires that a state vector be specified and that a measurement system be defined in terms of the chosen state vector. The vector was defined as the values of the constituent densities at the points at which an estimate is desired. For example, if a spatial resolution of 1 km is desired, the state vector is composed of the values of these densities at 1-km increments. If ozone and neutral atmospheric densities are desired over a 50-km range, there are 10^2 entries in the state vector. The state vector is generally designated by the vector x(t), where t represents an independent variable, usually time. To fully specify the state vector, a state equation must be given. For constituent densities, such an equation is based upon several assumptions. The first is that the densities observed at a given altitude are constant with regard to latitude or longitude variations over the scan area; this assumes that the scan areas are relatively small. The second assumption is that there are no random variations in the state vector within the scan time. With these two assumptions, the state equation becomes

$$\frac{dx(t)}{dt} = 0 \quad ; \quad x(0) = x_0 \quad . \tag{3.2-3}$$

The initial condition x_0 represents the constant value taken by the vector x(t). This value is assumed to be a random variable with a known mean and covariance.

The measurement equation can be given in terms of the state vector. The total measurement is a vector containing the intensities measured at m different wavelengths and is represented by a vector z(t). Each $z_i(t)$, or intensity in the i^{th} wavelength band, is given by

$$z_i(t) = c_i \exp\left(-h_i^T(t)x(t)\right) + w_i(t) \quad , \tag{3.2-4}$$

where c_i is a normalizing constant, $h_i^T(t)x(t)$ is a vector product form for the optical depth at the wavelength, and $w_i(t)$ is a white noise process associated with the measurement.

Equations (3.2-3) and (3.2-4) specify an estimation problem for the densities x(t). Specifically, given z(t) from t=0 to t=T, the estimates of x(t) are sought which will reduce the initial covariance associated with x(t). Using the structure discussed in Section 3.6, the linearized discrete recursive estimation equations are

$$k(t+1) = P(t)B(t+1)^T\left[B(t+1)P(t)B(t+1)^T + R\right] \quad , \tag{3.2-5}$$

$$x(t+1) = x(t) + k(t+1)\left[z(t) - z(t)\right] \quad , \tag{3.2-6}$$

and

$$P(t+1) = P(t) - K(t+1)B(t+1)P(t) \quad , \qquad (3.2\text{-}7)$$

where x(t) is the estimate, k(t) is the gain, P(t) the covariance of x(t) - x(t), R the measurement noise covariance matrix, z(t) the measurement estimate, and B(t) is an [m x n] matrix whose entries are the partial derivatives of the i^{th} intensity with respect to the j^{th} density. These equations completely specify the estimator and its performance.

The performance criterion for the estimator is the covariance associated with each estimate. The specific terms of P(t) that are of interest are the diagonal $P_{ii}(t)$ terms. Any estimation aims to reduce $P_{ii}(t)$ as close to zero as possible.

Dynamic variations of $P_{ii}(t)$ versus tangent heights are shown in Fig. 3.2-3 for a sample ozone density. The two lines on the graph represent the difference in performance between a system with respectively 33:1 and 100:1 signal-to-noise ratio. The improvement in performance can be noted by the lower terminal value of the normalized instantaneous covariance. Each curve represents the covariance for a density at the denoted altitude. This figure makes clear that no change in covariance occurs until the tangent height is equal to that of the altitude being measured. At that point, the measured intensity is affected by that density, and this effect is noted by the decreasing covariance. It can be further noted that the covariance reaches a point where it no longer decreases. This reflects the fact that scan heights below the layer in question are sensitive mainly to the layer at the scan height and relatively insensitive to the layers above.

3.2.4 Sensitivity Analysis

A sensitivity analysis has been performed for star occultation in a manner similar to the scattered sunlight (3.1.4). The stellar occultation constituent peak sensitivity curves, however, differ significantly from the scattered sunlight curves reflecting the measurement geometry of the stellar occultation experiment. In Figure 3.2-4, the sensitivity at 2850 Å is almost totally due to ozone. This is because the ozone extinction at 2850 Å is much greater than the corresponding neutral density or aerosol extinctions. Additionally the 2850 Å curve drops off below 60 km and above 95 km. The lower limit reflects the diminishing intensity of the signal with lower tangent heights whereas the upper altitude limit is due to the insignificant signal attenuation. The location of a sensitivity peak is determined by the distribution of the constituents and the atmospheric physics at a particular wavelength whereas the altitude region of maximum sensitivity is directly related to the quality (signal-to-noise) of the instrument. The curves of Figure 3.2-4 assume a constant white noise with an rms value 1/100th of the peak signal.

From Figure 3.2-4 it can be seen that ozone can be easily determined from 20 km up to 95 km utilizing three selected wavelengths. Neutral density can also be determined from 20 km to 95 km (but there is slightly less sensitivity

at 50 km). This reduced neutral density sensitivity is caused by the ozone absorption centered at 2600 Å. If the atmosphere was purely Rayleigh scattering, the neutral density sensitivity curve for 2600 Å would be located at about 50 km. Finally, aerosols are virtually unobservable above 35 km, but wavelengths near 7000 Å will be sensitive to them around 20 km.

It is important to note, however, that the sensitivity curves are density dependent and are based on the assumption of equal initial covariance. For example, if there was a large anomalous aerosol layer above 35 km and neutral density was well known, it would be possible to successfully invert the layer as is illustrated in the subsequent section on simulation results. The reduced sensitivity for aerosols above 35 km is based on the reference aerosol extinction model and the direct competition for information content with both neutral density and ozone.

The dependence of the variances on the signal-to-noise ratio, sampling rate, spatial resolution, and position uncertainties has also been studied (McGarty and Tompkins, 1971). Fig. 3.2-5 shows a plot of the power signal-to-noise ratio of the measurement versus the percent error of the final estimate for ozone density at 78 km. The percent error is the percent of the initial covariance which results at the end of a single scan. It is clear that high signal-to-noise ratios provide significant decreases in final percent error.

Resolution is defined as the distance between density samples. Generally, a resolution of 1-2 km is sought. The sampling rate is the difference in tangent heights at which measurements are made. The sample rate is always less than or equal to the desired resolution. Fig. 3.2-6 plots sample rate versus resolution for a given signal-to-noise ratio and parametrically in terms of four values of the ratio of the final covariance to the initial covariance for the four altitudes selected. These curves have been used to determine the required sample rate for a given resolution and final performance.

One of the potential problems is that of satellite-position uncertainty. The inversion equations assume perfect knowledge of satellite position with respect to the earth. This is never true, and the effect of the resulting uncertainties has been analyzed. It was found that for typical altitude, down-range and offset-angle errors, the errors involved were equivalent to less than one tenth of the total signal observed at that time. These errors may tend to bias the profile by means of an altitude shift, but such shifts are expected to be less than 1 km.

3.2.5 Simulated Results

Star occultation inversion simulations were carried out in a completely analogous fashion to the scattered light inversions (section 3.1-5). For each of the following curves the dotted line represents the actual value of the Perturbed Reference State used to generate the simulated measurements and the two solid lines represent rms limits centered about the final estimate state of the perturbed reference.

Figure 3.2-7 shows the results of an average simulation in which the initial estimate of the state was uniformly in error by one order of magnitude. The inversion was run for wavelengths of 2000, 2600, 3000, 3400, and 7000 Å. The gain was damped by a factor of two and a Gaussian white instrument noise was added of 1/100th of the peak signal. The results are predictable and agree with the sensitivity curve discussed previously. These wavelengths cover ozone better than neutral density and accordingly the ozone answer is more accurate as reflected by the smaller covariance. Also, aerosols are poorly known everywhere, but above 35 km the filter failed to converge even close to the correct answer as anticipated from the sensitivity curves.

Figure 3.2-8 is a simulation designed to test the filter on a specific atmospheric phenomena. It has been hypothesized that a large aerosol layer is present at approximately 50 km, and in this simulation such a layer was used to generate the simulated measurements. Wavelengths of 2000, 3000, 3200, 3400, 4000, and 7000 Å were used with a gain damping of two and a white instrument noise of 1/100th of the peak signal. In addition it was assumed that the initial variance of aerosols and ozone was one order of magnitude whereas the initial variance of neutral density was 1/10th of an order of magnitude. This inversion was successful which illustrates that sensitivities are dependent on initial covariances and absolute densities. In general, normal aerosol distributions as in Figure 3.2-8 will not be inverted from star occultation data; however, large anomalous layers will show up on the data and can be detected.

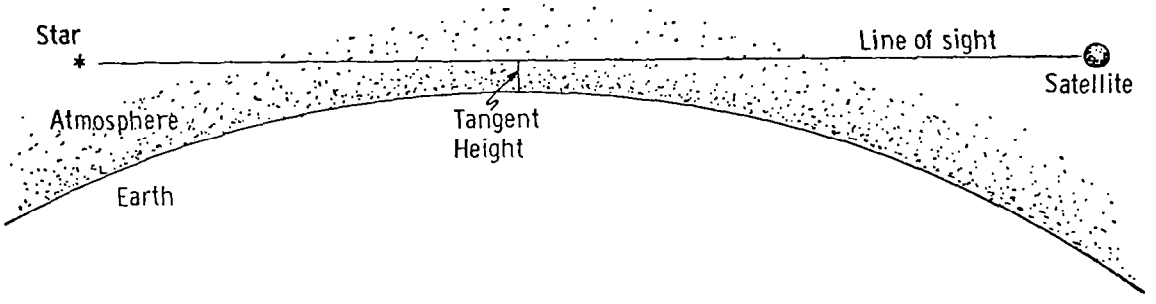

Fig. 3.2-1 Stellar Occultation Geometry

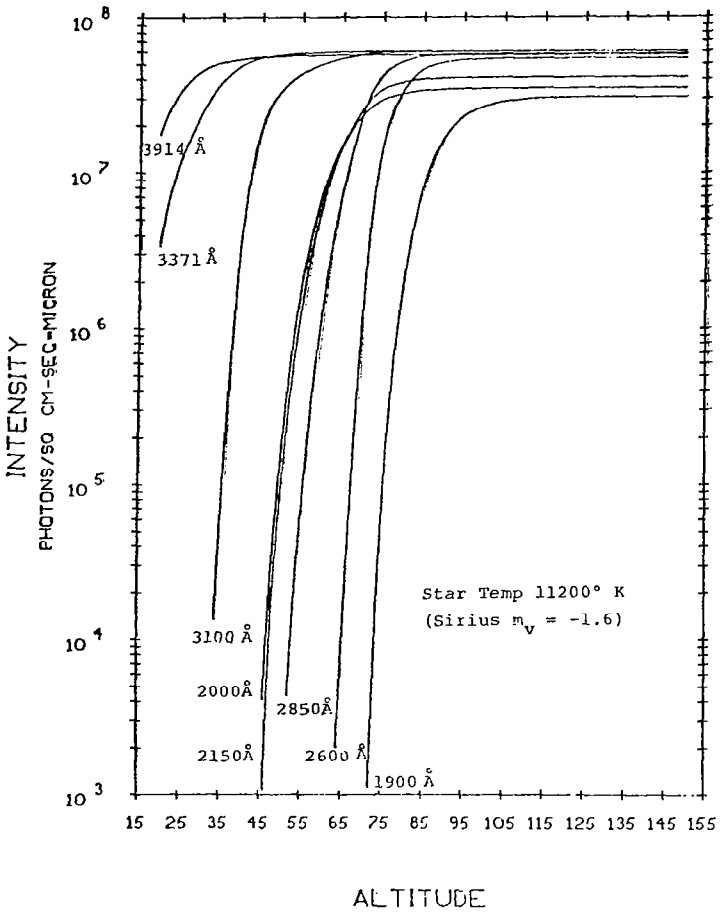

Fig. 3.2-2 Intensity vs. Tangent Height for Stellar Occultation Wavelengths.

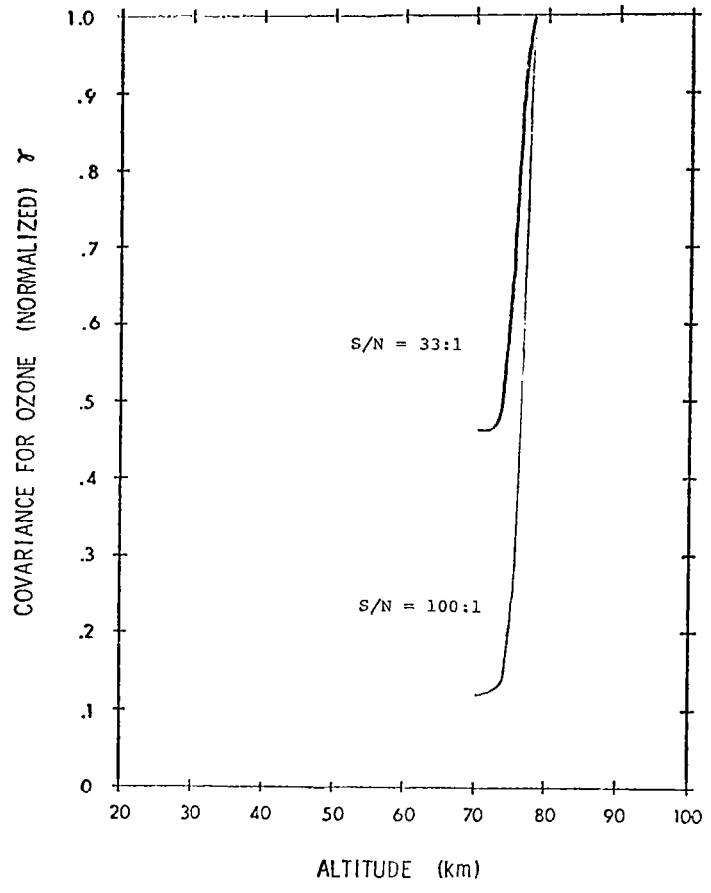

Fig. 3.2-3 The ratio γ of the final to initial covariance $P_{ii}(t)/P_{ii}(t_0)$ for the ozone concentration at 78 km as a function of tangent height.

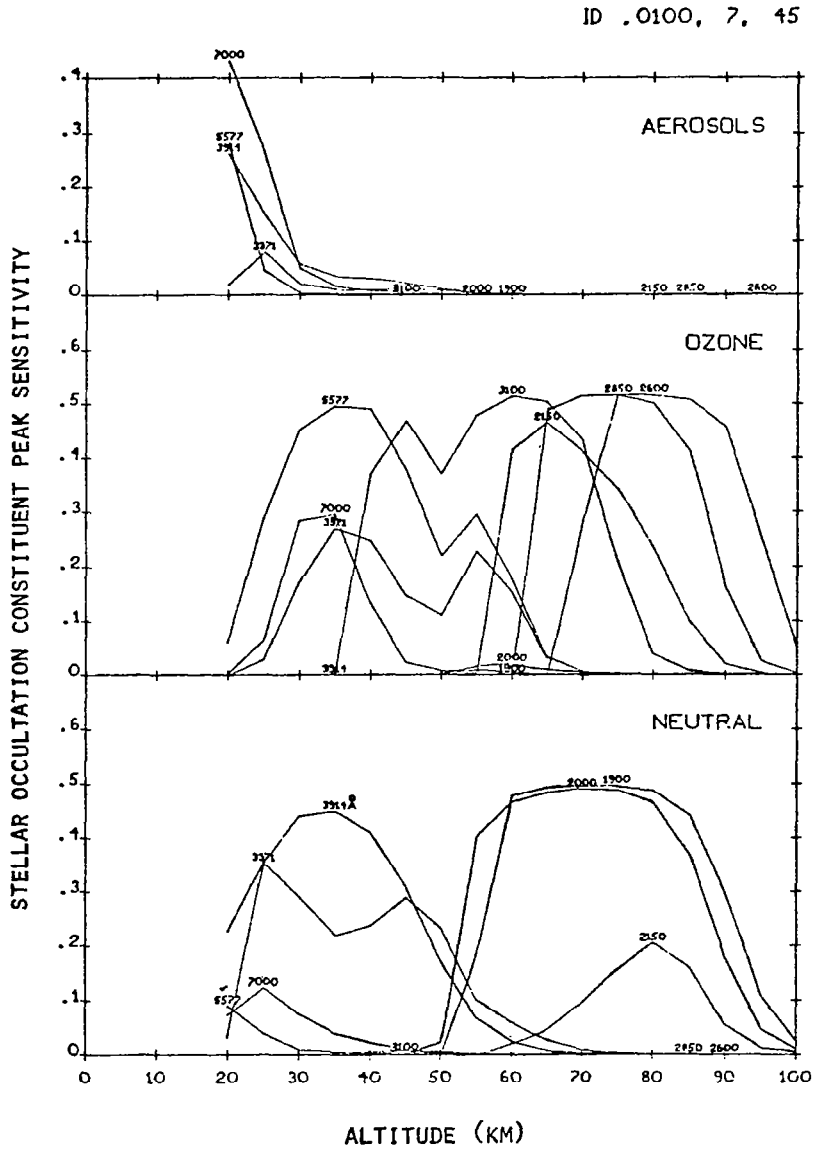

Fig. 3.2-4 Stellar Occultation Constituent Peak Sensitivity Profiles

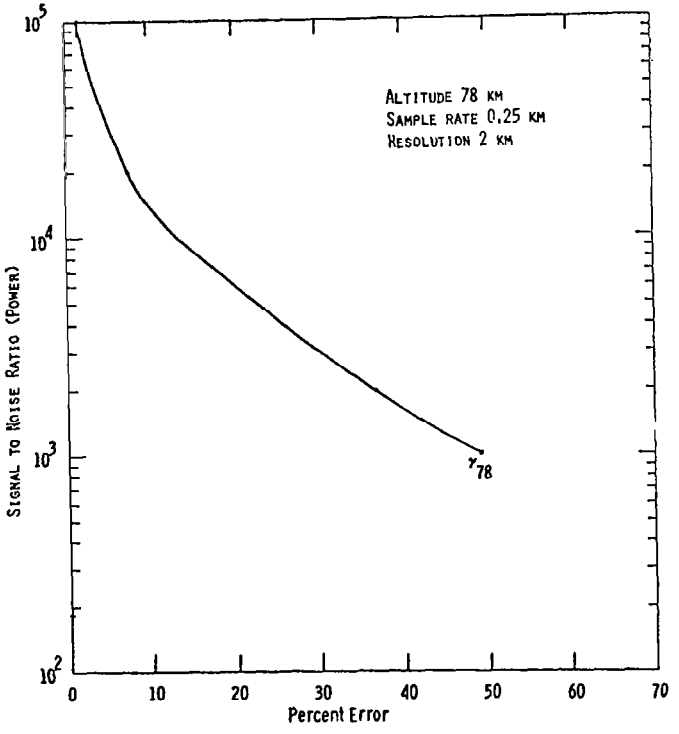

Fig. 3.2-5 The error associated with the determination of the ozone concentration at 78 km by the occultation inversion technique for the various S/N ratios.

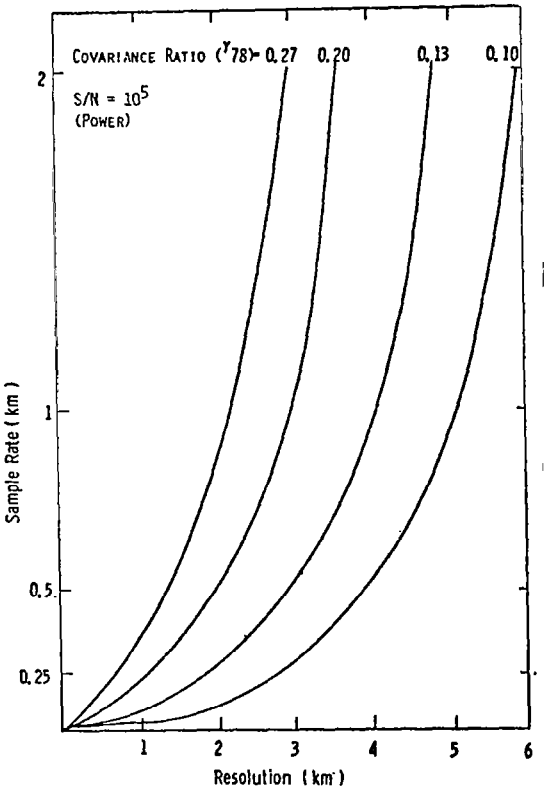

Fig. 3.2-6 The sampling rate required to give a specific altitude resolution and accuracy for the ozone concentration in the neighborhood of 78 km.

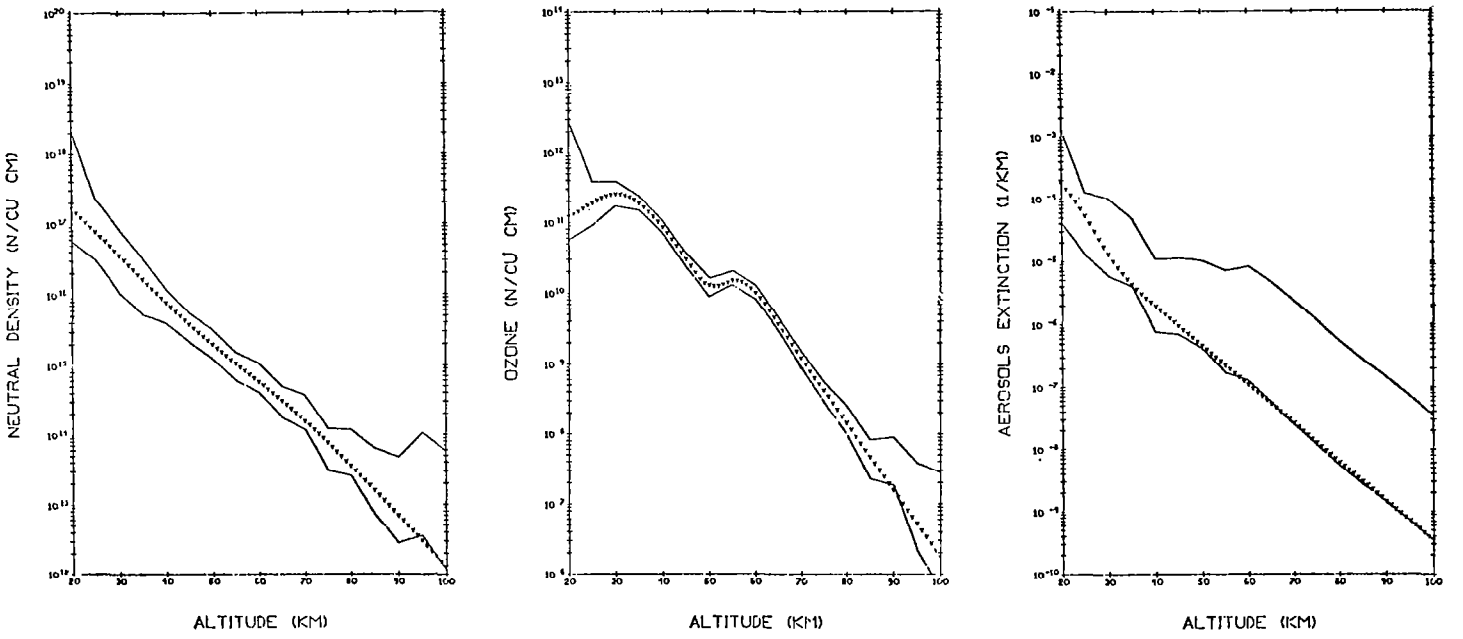

Fig. 3.2-7 Simulation results--stellar occultation inversion where neutral atmospheric density, ozone (nighttime) and aerosol extinction are reduced an order of magnitude from references.

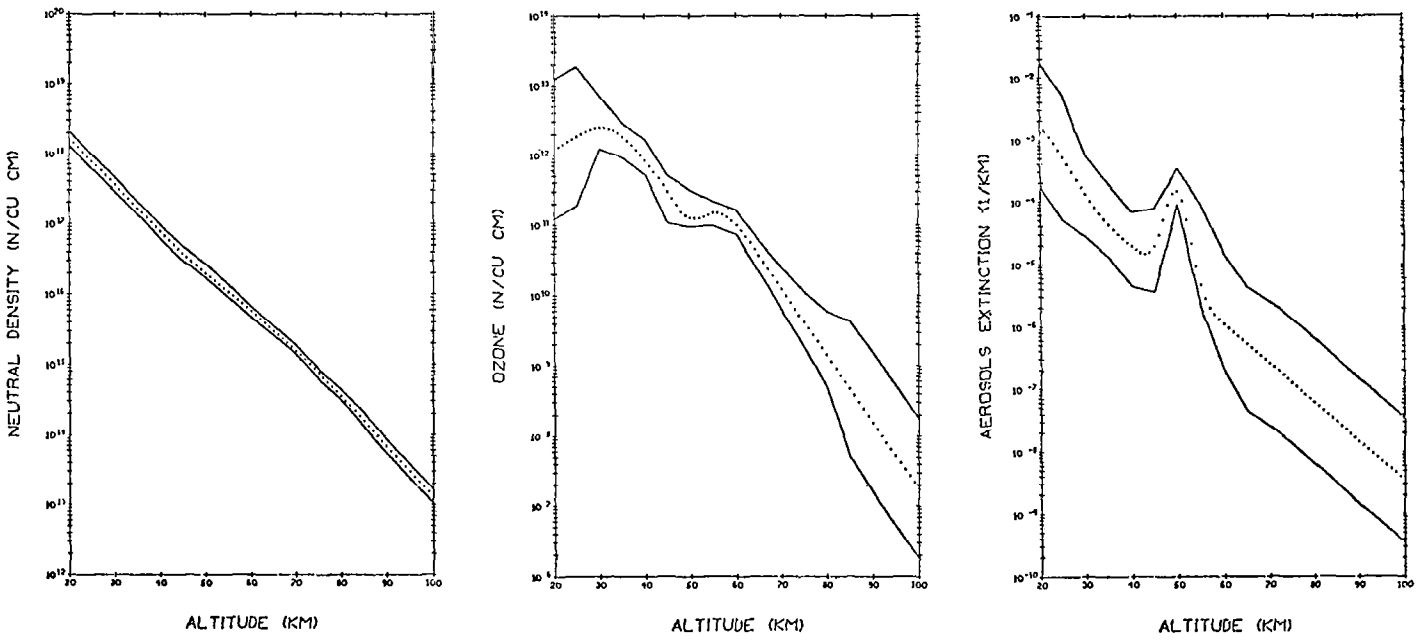

Fig. 3.2-8 Simulation results--stellar occultation inversion with a 1.5 order of magnitude increase in aerosol extinction at 50 km.

Reference for Section 3.2

McGarty, T. P., and Tompkins, K. L., "The Estimation of Constituent Density States by an Occultation Experiment–A Quasi-Exact Solution to the Kushner-Stratonovich Equation", Internal Report No. AER 8-6, February, 1971.

3.3 ATOMIC OXYGEN MEASUREMENTS AND THE 5577 Å EMISSION PROBLEM

3.3.1 Introduction

This section examines the use of a limb-scan measurement of 5577 Å as a technique for obtaining atomic-oxygen profiles in the 90-100 km region of the atmosphere. 5577-Å emission is categorized according to the various physical processes which contribute to the emission. It is noted that three-body reactions involving oxygen atoms are largely responsible for the nocturnal emission of 5577 Å at subauroral latitudes. However, the particular three-body reaction and its rate constant are uncertain. It is therefore proposed that additional simultaneous limb-scan measurements be made, consisting of monitoring the Herzberg emission from molecular oxygen and measurements of neutral density using the atmospheric absorption of starlight at wavelengths in the molecular-oxygen absorption band below 100 km. This proposal is investigated and it is noted that profiles of atomic-oxygen concentration may be obtained in this way unless reaction-rate constants are very sensitive to atmospheric temperature. More details and additional references concerning the work reported here are contained in Cunnold, 1971 and 1970b.

3.3.2 Morphology of 5577-Å Emission

5577-Å emission is produced from the ^1S excited state of atomic oxygen, which is situated roughly 4 ev above ground level. A schematic representation of the latitudinal variation of 5577 Å emission and other nightglow emissions is illustrated in Fig. 3.3-1 (from Roach and Smith, 1967). 5577 nightglow emission consists of tropical arcs, aurora, and an emission at the 100-km level. An altitude profile of the 5577 nightglow emission is illustrated in Fig. 3.3-2, based upon a rocket experiment by Gulledge et al (1968). Figure 3.3-3 shows another profile—measured, however, during a moderately intense aurora. It may be noted that 5577-Å radiation is roughly two orders of magnitude more intense during a strong aurora than in its absence. Figure 3.3-4 portrays a daytime altitude profile and, in this case, an additional layer of 5577-Å radiation is present at the 175-km level.

3.3.3 The Inversion of 5577-Å Limb Profiles

We have investigated the errors associated with determining volume emission rates for 5577-Å radiation from measurements of 5577 radiation using a limb-scanning technique. This inversion is a specialized application of the general inversion technique developed for the MIT Aeronomy Program. Results are presented in Figs. 3.3-5 and 3.3-6 for a nightglow and a dayglow emission profile. It may be noted that, for the experimental parameters which we believed reasonable to use, it is possible to obtain 5577 volume emission rates to 10 percent accuracy not only at the emission peaks but also at altitudes at which the emission is reduced by a factor of 6, compared to the value at the altitude of the peak. Therefore meaningful measurements of 5577 emission profiles both by day and by night appear probable. The peak signal level of 5577 emission viewed on the limb is roughly 7×10^8 photons/sec-cm^2-ster. It should be noted that during the daytime the Rayleigh scattered signal

contribution for reasonable filter bandwidths (e.g., 10 Å) equals the 5577 signal at 90 km altitude. Our measurements are further limited by this problem. However, an excellent baffling system has been developed at the Draper Laboratory of MIT, and this system prevents Rayleigh-scattered elements from altitudes below the line of sight from contributing to the received signal.

As was previously noted, the 5577 Å signal from an aurora will usually be considerably more intense than that from the nightglow. On the basis of the dayglow results (Fig. 3.3-6a-e) and anticipated auroral emission profiles (Cunnold, 1970a), we believe it possible to make meaningful measurements of the nightglow layer of 5577 emission in the presence of weak aurora (i.e. an IBC I aurora). That is, it should be possible to make meaningful nightglow measurements of 5577 emission approximately 20 percent of the time at auroral latitudes. In addition, measurements of auroral emission profiles are not undesirable, for virtually all such measurements will be separable from the nightglow and they should contribute to an understanding of auroral emission processes.

3.3.4 Physical Processes Responsible for 5577-Å Emission

Current thinking regarding the processes responsible for atmospheric 5577-Å emission is summarized in Table 3.3-I. It may be noted that this emission must be subdivided into high and low altitudes and into day and night. The auroral 5577 emission is not included in the table. The relevant processes responsible for the excitation of the ^1S state of atomic oxygen are described in more detail below.

Dissociative recombination is responsible for $O(^1S)$ production via the reactions:

$$O_2^+ + e \longrightarrow O(^3P) + O(^1S) + 2.78 \text{ ev} \qquad (3.3\text{-}1)$$

$$O_2^+ + e \longrightarrow O(^1D) + O(^1S) + 0.95 \text{ ev} \quad . \qquad (3.3\text{-}2)$$

This process almost certainly contributes to 5577 emission at high altitudes both during the day and the night. In the nightglow, it is probably responsible for all the emission in the tropical arcs, while in the daytime this process must compete with photoelectron excitation (Wallace and McElroy, 1966), and the relative contributions of the two processes are uncertain.

Photodissociation contributes to the daytime production of $O(^1S)$ via the following reaction:

$$O_2 + h\nu \longrightarrow O(^3P) + O(^1S) \qquad \lambda \leq 1335 \text{ Å} \qquad (3.3\text{-}3)$$

$$O_2 + h\nu \longrightarrow O(^1D) + O(^1S) \qquad \lambda \leq 1102 \text{ Å} \qquad (3.3\text{-}4)$$

Wallace and McElroy (1966) point out that this process may be significant in the dayglow emission of 5577 at the 90-100 km level, but that the contribution is uncertain and that "the principal uncertainty is due to lack of information about the detailed processes responsible for the observed O_2 absorption below

1344 Å."

Photoelectrons may provide the energy of excitation in a manner similar to that of photons. McElroy (1965) and Wallace and McElroy (1966) have evaluated the rate of this reaction and have concluded that the high-altitude daytime emission of 5577 may be explained on just this basis. Recent laboratory results by Zipf (1970) on electron-impact cross sections have cast doubts on Wallace and McElroy's conclusion, however.

Chemical processes are believed to make large contributions to the production of $O(^1S)$ below 120 km. The actual process is in doubt; however, two particular possibilities are

$$O + O + O \longrightarrow O_2 + O(^1S) \quad , \tag{3.3-5}$$

and the two-step reaction,

$$O + O + M \longrightarrow O_2^* + M \tag{3.3-6}$$

$$O_2^* + O \longrightarrow O_2 + O(^1S) \quad , \tag{3.3-7}$$

where O_2^* denotes an excited state of molecular oxygen, either $^3\Delta_u^+$ or $^1{}_u^-$.

The emission of 5577 Å radiation by $O(^1S)$ oxygen atoms is limited to a certain extent (below 90-100 km) by deactivation by collisions. Laboratory measurements have indicated that most deactivation is by molecular oxygen (with a rate of $2 \times 10^{-13} cm^3/sec$), rather than molecular nitrogen or atomic oxygen.

5577-Å emission in aurora is poorly understood. The reason for this is that laboratory measurements of electron-impact cross sections have resulted in cross sections roughly an order of magnitude smaller than would be required to account for auroral emission. The most likely process is probably dissociation of molecular oxygen via electron impact. Further observations of the height profiles of 5577 and other auroral emission (e.g., nitrogen second-positive band at 3371 Å) are needed to resolve this problem.

3.3.5 Atomic-Oxygen Distribution at the 100-km Level

Atomic oxygen is produced at altitudes above 100 km by the photodissociation of molecular oxygen. The atomic oxygen is mixed downwards by eddy diffusion to form a concentration peak at the 95-km level. There, the lifetime of the oxygen atoms is several days. Below 95 km, chemical reactions are responsible for the loss of oxygen atoms. Although this theory of the atomic-oxygen distribution is generally acknowledged to be correct, details are lacking. This uncertainty is the result of both an absence of information on the eddy-diffusion coefficient or even a physical understanding of the mechanism responsible for eddy diffusion, and uncertainties concerning the rates of certain chemical reactions, particularly those involving minor atmospheric constituents.

$$O_2(^3\Sigma_u^+) \xrightarrow{A_2} O_2 + h\nu_{Herz} \quad , \tag{3.3-18}$$

where the k's are reaction rates and the A's are radiative transition probabilities. O_2* denotes the excited states $^3\Delta_u^+$, $^1\Sigma_u^-$, or even $^3\Sigma_u^+$. An energy-level diagram for molecular oxygen is shown in Fig. 3.3-8. These excited states of oxygen are partially deactivated by collisions, and these quenching processes (of rate q) complete the reaction scheme:

$$O_2(^3\Sigma_u^+) + M \xrightarrow{q_1} O_2 + M \tag{3.3-19}$$

$$O_2* + M \xrightarrow{q_1'} O_2 + M \tag{3.3-20}$$

$$O_2(^3\Sigma_u^+) + O \xrightarrow{q_2} O_2 + O \tag{3.3-21}$$

$$O_2* + O \xrightarrow{q_2'} O_2 + O \tag{3.3-22}$$

$$O(^1S) + M \xrightarrow{q_3} O + M \tag{3.3-23}$$

$$O(^1S) + O \xrightarrow{q_4} O + O \tag{3.3-24}$$

Then, the production rate for 5577 emission may be expressed

$$j_{5577} = \frac{1}{1 + \frac{q_3[M]}{A_2} + \frac{q_4[O]}{A_2}} \left\{ k_2[O]^3 + \frac{k_1'[M][O]^2}{1 + \frac{q_1'[M]}{k_2'[O]} + \frac{q_2'}{k_2'}} \right\} \quad , \tag{3.3-25}$$

while the production rate for Herzberg emission is given by

$$j_{Herz} = \frac{k_1[M][O]^2}{\left[1 + \frac{q_1[M] + q_2[O]}{A_1}\right]} \quad . \qquad (3.3\text{-}26)$$

The problem with inverting these expressions to yield atomic-oxygen concentrations is the lack of detailed knowledge concerning the reaction rates. Therefore, it is proposed that a relationship between j5577 and jHerz be obtained by eliminating the unknown [O] (the concentration of atomic oxygen) and that a curve be fitted to results obtained by simultaneous measurements of 5577 and Herzberg emission profiles. The fitting procedure is improved by the addition of simultaneous observations of neutral density ([M]). Simultaneous measurements of neutral density may be made without difficulty below 100 km at night by making limb-scan observations of the ultraviolet absorption of the light from certain stars in the Schumann-Runge absorption bands of molecular oxygen. A wavelength of roughly 1900 Å is appropriate for making observations at the 95-km level, and the data may be reduced by the inversion techniques to be used in other phases of the MIT Aeronomy Program. The curve-fitting procedure should yield values for certain reaction rates and should show, in particular, which reactions are dominant. The latter result may well be a function of altitude.

The experiment may be presented in more physical terms as follows: What is actually being proposed is that the relative shapes of the emission profiles of 5577 and Herzberg emission as a function of altitude be examined. Since there are unknown constants of proportionality involved (i.e., reaction rates), the procedure is to match up the profiles at a particular altitude (e.g., at or near the emission peaks) and then to attempt to find the power of jHerz that j^2_{5577} varies as. A sufficiently large signal-to-noise ratio must be experimentally available at altitudes other than those of the emission peaks in order to determine whether the appropriate power of jHerz is 3 (for example) or 4 or even some combination of such relationships. Gadsden and Marovich (1969) present a working example of this technique.

At the present time, according to a review by Schiff (1969), the reaction rates of processes involving the ground states of atoms or molecules, and in addition the temperature dependence of such reactions, are fairly well known from laboratory measurements. Reactions involving excited atomic or molecular species have not been so widely studied in the laboratory, although quenching rates for many processes of atmospheric interest are now believed to be reasonably well established. On the other hand, the chemistry of the latter reactions is poorly understood and their temperature dependence is unknown. It should be noted that in all cases, the ability of laboratory physicists to make accurate measurements of reaction rates greatly exceeds their ability to simulate atmospheric conditions appropriate to the 100-km level. The fact that many laboratory-measured reaction rates do not correspond to rates

deduced on the basis of atmospheric effects is usually ascribed to the inaccurate simulation of atmospheric conditions in the laboratory. The measured values of reaction rates and the upper bounds which we shall use are summarized in Table 3.3-II.

The proposed technique is called into question if the important reactions possess rate constants which are strongly temperature sensitive (i.e., rate constants which change by 50 percent for a temperature change of 10 percent). This possibility cannot be eliminated at the present time. It would be desirable, therefore, to subdivide our data according to temperature. The best estimates of temperature at the present time are contained in CIRA 1970. Unfortunately, there have been few experimental verifications of the CIRA 1970 model for the 100-km region, and the possible errors and variations about the mean value of temperature should be considered as about 10 percent at the present time. Therefore, only a coarse temperature classification makes sense. For example, the data could be subdivided according to the three categories: moderate temperatures (equatorial regions), low temperatures (high latitude, summer conditions), and high temperatures (high latitude, winter conditions). Even after such a categorization, however, very strongly temperature-dependent reaction rates would still render the data very difficult to interpret by the techniques outlined in this report. Clearly, a simultaneous measurement of temperature in the 90-100 km region would be a desirable addition to the Rayleigh-scattering techniques proposed in the MIT Aeronomy Experiment, because the hydrostatic approximation ceases to apply to this altitude range. This problem requires further study, and for the present, one is left with the assumption that strongly temperature sensitive reaction rates are not important in the production of 5577 Å or Herzberg emission.

3.3.8 Conclusions

It has been shown that simultaneous nighttime measurements of the altitude profiles of 5577 Å and the Herzberg emission of molecular oxygen should lead to the establishment of the particular chemical processes which are responsible for these emissions during the night. On the basis of this information it is then possible to deduce nighttime atomic oxygen profiles with the important limitation that an improved knowledge of laboratory reaction rates is needed before these relative concentration profiles can be fixed in absolute magnitude at a single altitude and hence at all other altitudes. We do not believe that this important restriction detracts appreciably from the proposed experiment, partly because there are no other techniques now available that can measure atmospheric atomic-oxygen concentrations. It should be emphasized that the experiment is capable of producing the shapes of atomic-oxygen profiles, and also the relative concentration and profile shapes at different latitudes and at different times. However, it is apparently necessary to make the assumption that the reaction rates which determine the emission of 5577 and Herzberg radiation are not strongly temperature sensitive. There is no evidence, on the basis of present laboratory measurements, for or against this assumption.

Hunten (1970) has suggested that atomic-oxygen profiles may simply be obtained by monitoring Herzberg emission profiles. While we would not argue with the basic idea of this proposal, we suggest that a simultaneous measurement

of 5577 Å emission would add significantly to the information that can be obtained by such an experiment. Comparison with 5577-Å profiles should serve to verify the expected reaction rates appropriate to the Herzberg emission and, more importantly, should help to establish the reactions which produce the 5577 emission. The latter is important because 5577 emission may be monitored from the ground, whereas the Herzberg emission cannot. Therefore, once the processes responsible for the 5577 emission are understood, a cheap and simple means of monitoring atmospheric atomic oxygen concentration becomes available. Furthermore, if an understanding of 5577 Å emission at night can be obtained, then an understanding of 5577 Å during the daytime becomes more likely—the further implication being that it becomes more likely that daytime profiles of atomic-oxygen concentration may be measured. In this connection, it may be noted that the Herzberg emission of molecular oxygen has never been observed in the daytime. Daytime and auroral measurements of 5577-Å emission are also desirable.

TABLE 3.3-I

POSSIBLE CONTRIBUTIONS TO THE EXCITATION OF $O(^1S)$*

Physical Process	Dayglow		Nightglow	
	>120 km	<120 km	>120 km	<120 km
Fluorescence	<20R	-	-	-
Dissociative recombination	100%	-	10-100R	-
Photodissociation	-	90%	-	<10R
Photoelectron excitation	100%	-	-	-
Chemical processes	-	100%	-	100%

*The maximum possible contributions of various physical processes to the excitation of $O(^1S)$ which is manifested by 5577 Å emission observed to arise from the altitude ranges indicated.

TABLE 3.3-II

REACTION RATES

Reaction Rate	Laboratory Measurement	Assumed Possible Range
k_1	2×10^{-37} cm^6/sec	3×10^{-33} - 10^{-37} cm^6/sec
k_2	1.8×10^{-34} cm^6/sec	10^{-32} - 10^{-35} cm^6/sec
k_1'		3×10^{-33} - 10^{-37} cm^6/sec
k_2'		10^{-11} - 10^{-16} cm^3/sec
A_1		10^{1} - 10^{-3}
A_2		1.28
q_1		10^{-11} - 10^{-15} cm^3/sec
q_1'		10^{-11} - 10^{-15} cm^3/sec
q_2		10^{-11} - 10^{-15} cm^3/sec
q_2'		10^{-11} - 10^{-15} cm^3/sec
q_3	1 - 5×10^{-13} cm^3/sec	10^{-12} - 10^{-13} cm^3/sec
q_4	10^{-13} cm^3/sec	10^{-12} - 10^{-13} cm^3/sec
$\frac{k_1'k_2'}{q_1'}$	1.8×10^{-34} cm^6/sec	10^{-32} - 10^{-36} cm^6/sec

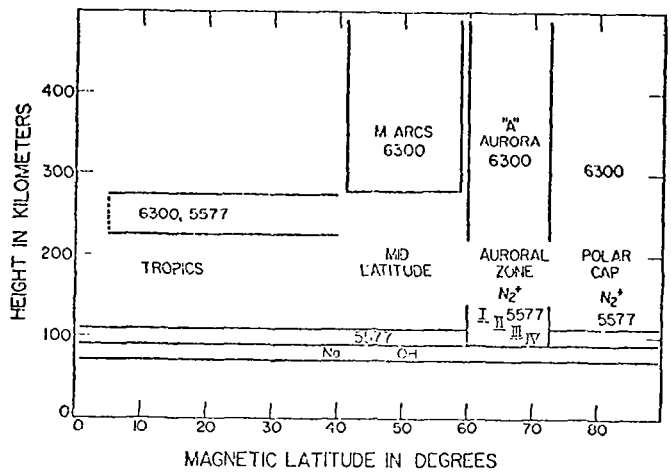

Fig. 3.3-1 Schematic representation of the principal nightglow emissions in the atmosphere as a function of height and latitude (Roach and Smith (1967)).

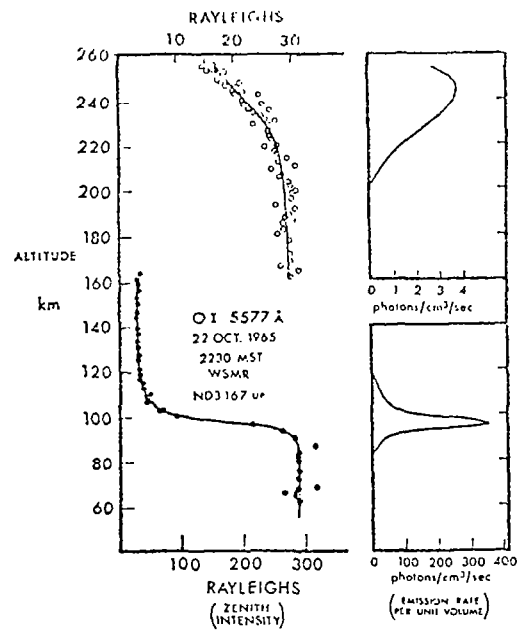

Fig. 3.3-2 5577 Å intensity profiles versus altitude. The solid lines drawn through the open circles are fifth-order least-squares fits. The derived "apparent" emission rates per unit volume are indicated to the right in the figure. The intensity scale at top applies to the F-region layer; the scale at bottom applies to the layer at 97 km (Gulledge et al (1968)).

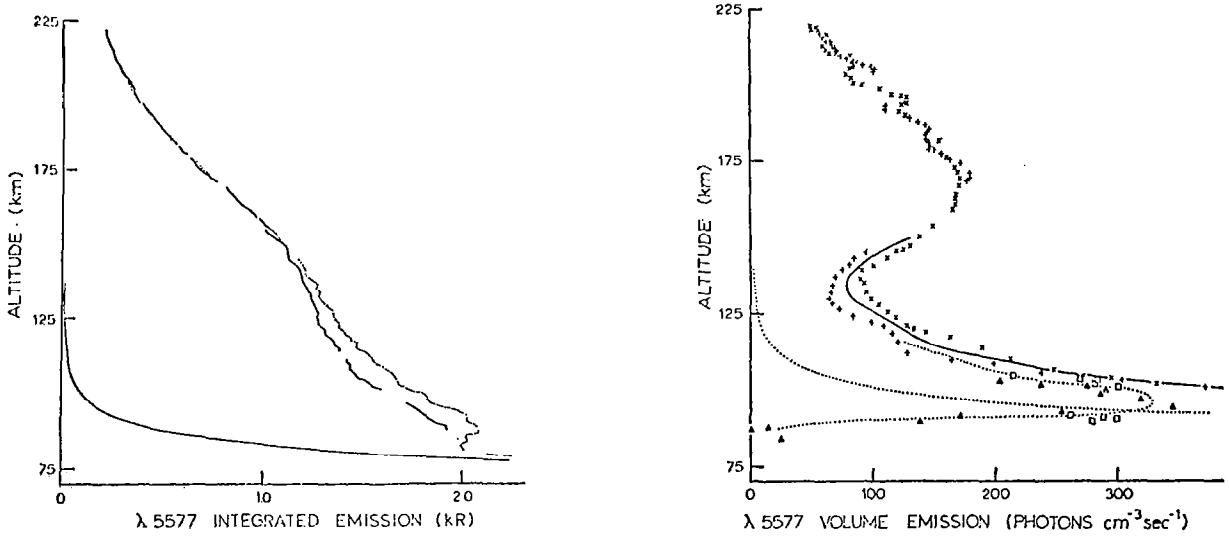

Fig. 3.3-3 Zenith intensity of the 5577 Å oxygen line in the dayglow, measured (left) in a rocket flight by Wallace and McElroy (1966). The derivative of the zenith intensity with respect to altitude (right) giving the volume emission rate. The up and down legs of the flight are separated; a dotted line shows the contribution of Rayleigh scattered sky background.

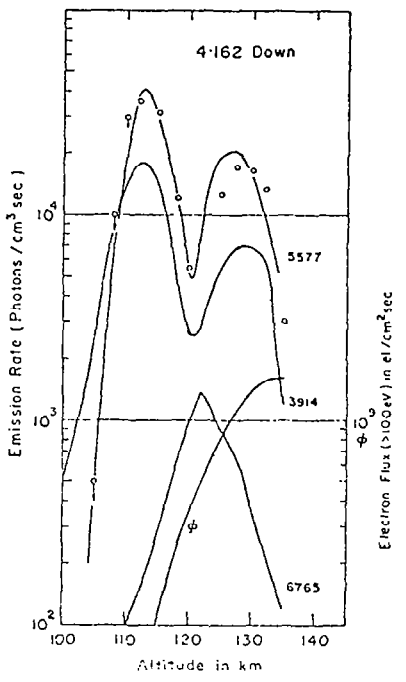

Fig. 3.3-4 Volume emission rates and electron flux ϕ (greater than 0.1 keV) for downleg in the auroral zone in 1966 (class II + aurora). Circles are the calculated rates for λ5577. Arrows show correction for quenching (Donahue et al. (1968)).

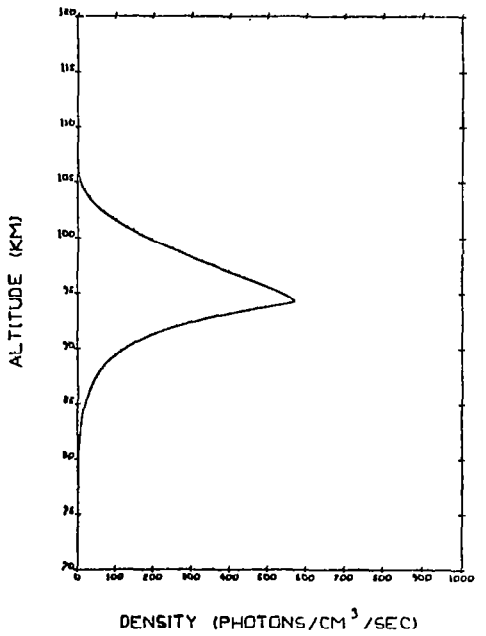

Fig. 3.3-5a Nightglow 5577 Å Emission Profile Based on Measurements by O'Brien *et al* (1965)

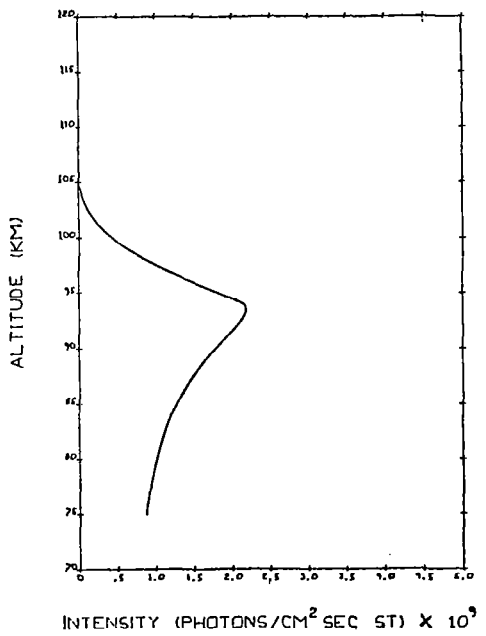

Fig. 3.3-5b Theoretical Horizon Profile of Atomic Oxygen [O^1S] Nightglow

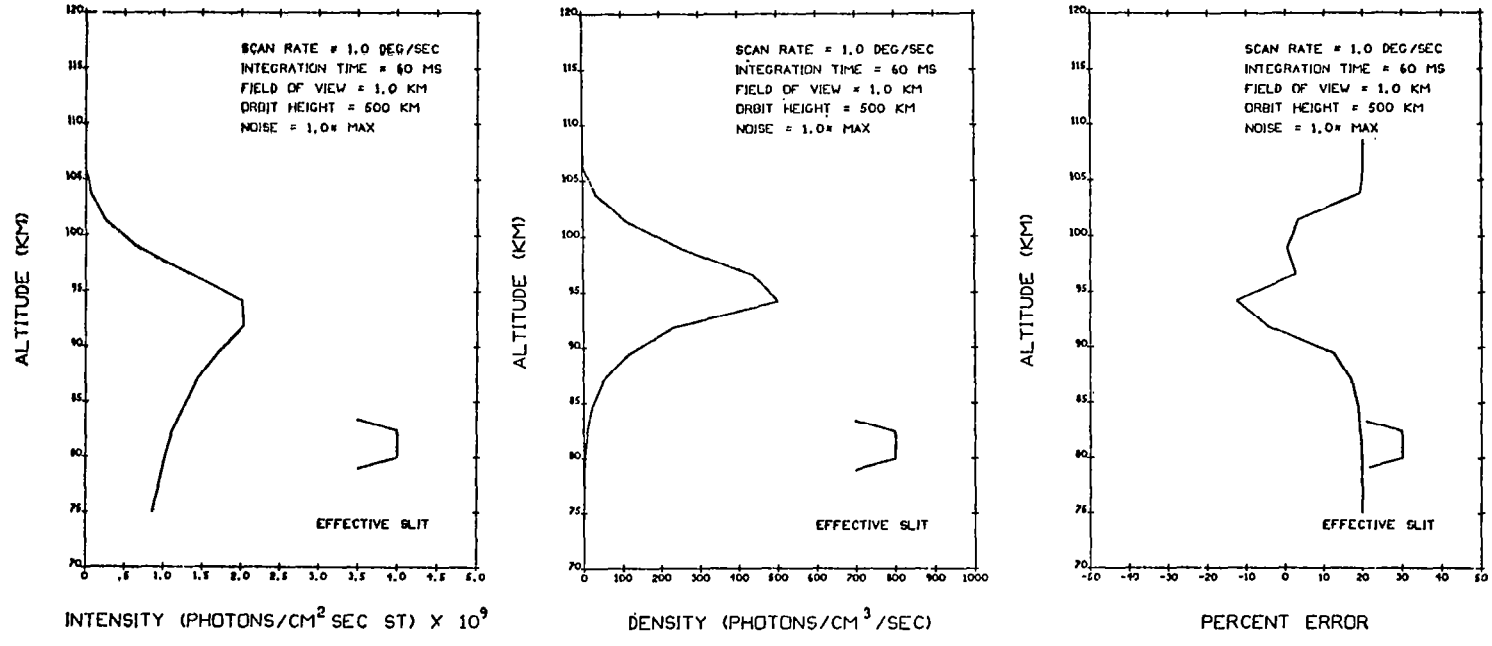

Fig. 3.3-5c Simulated Horizon Measurement of Atomic Oxygen [O^1S] Nightglow

Fig. 3.3-5d Simulated Horizon Inversion of Atomic Oxygen [O^1S] Nightglow Vertical Distribution

Fig. 3.3-5e Atomic Oxygen [O^1S] Nightglow Error Analysis of Simulated Horizon Inversion (Note: the 20% error at the top and bottom reflects the initial offset (20%) on the first estimate of the vertical distribution.)

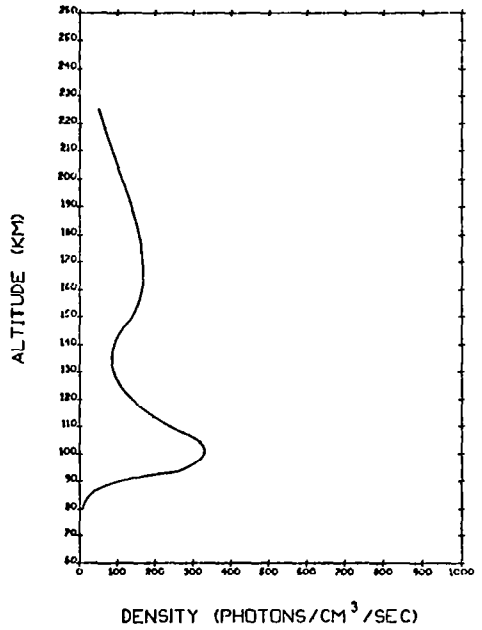

Fig. 3.3-6a Dayglow 5577 Å Emission Profile Based on Measurements by Wallace and McElroy (1966)

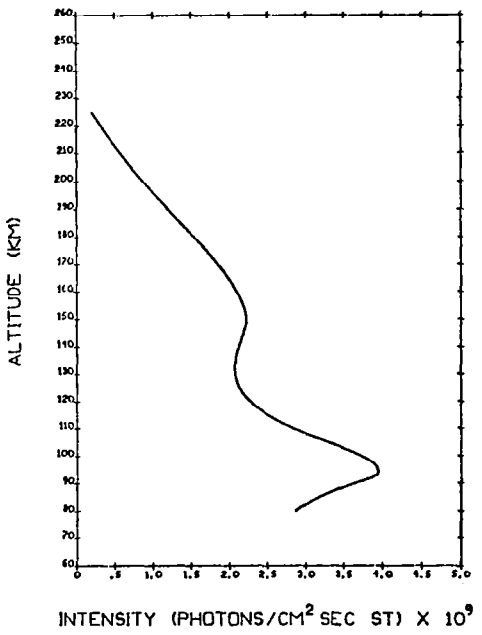

Fig. 3.3-6b Theoretical Horizon Profile of Atomic Oxygen [O^1S] Dayglow

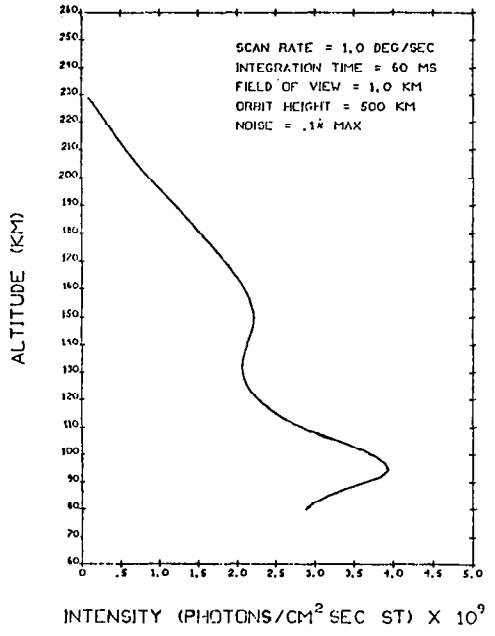

Fig. 3.3-6c Simulated Horizon Measurement of Atomic Oxygen [O^1S] Dayglow

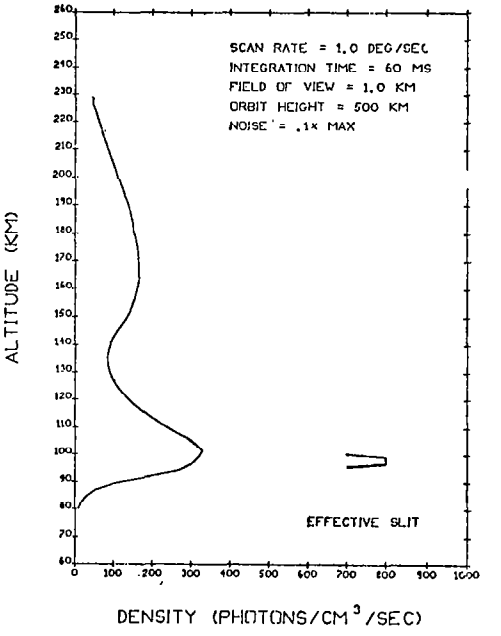

Fig. 3.3-6d Simulated Horizon Inversion of Atomic Oxygen [O^1S] Dayglow Vertical Distribution

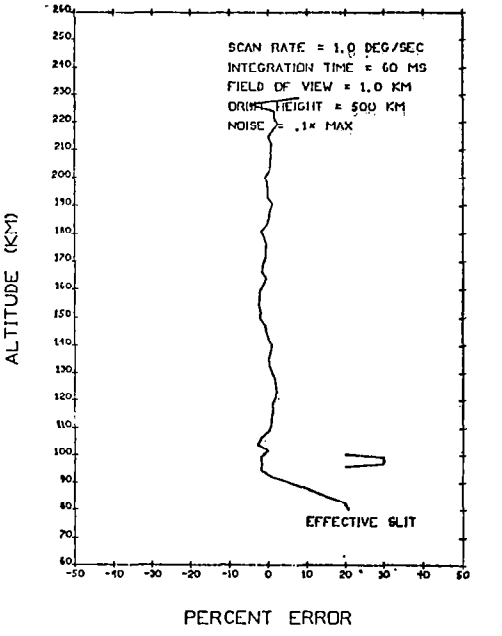

Fig. 3.3-6e Atomic Oxygen [O^1S] Dayglow Error Analysis of Simulated Horizon Inversion (Note: the 20% error at the bottom reflects the initial offset (20%) on the first estimate of the vertical distribution.)

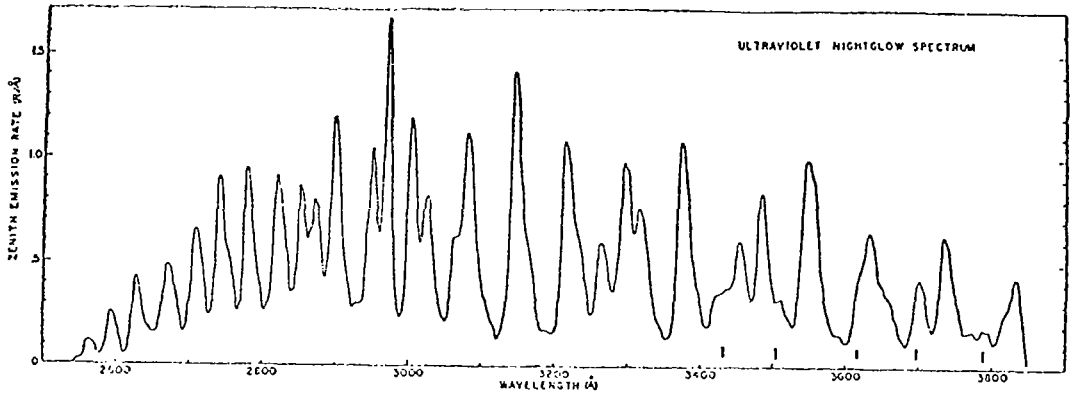

Fig. 3.3-7 The ultraviolet nightglow spectrum. The OI 2972 Å line is mixed with the Herzberg 7, 4 band at 2976 Å. The short bars mark features not belonging to the Herzberg system (Hennes, 1966).

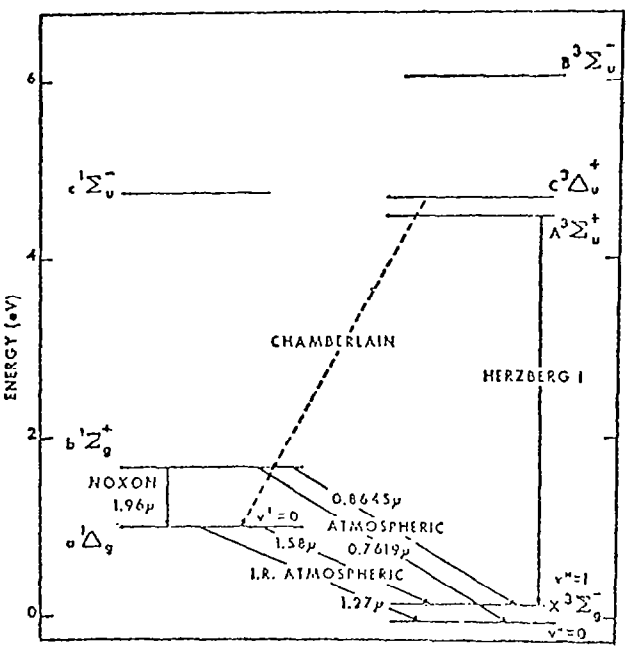

Fig. 3.3-8 Energy levels and transitions of molecular oxygen (Evans and Llewellyn, 1970).

References for Section 3.3

Cunnold, D. M., "Auroral Spectra", Internal Report No. AER 2-3, November, 1970a.

_____, "The Deduction of Atomic Oxygen Concentrations from Measurements of 5577 A and Herzberg Emission", Internal Report No. AER 2-4, April, 1971.

_____, "The Measurement of 5577 Å Radiation Profiles", Internal Report No. AER 2-1, August, 1970b.

Donahue, T. M., T. Parkinson, E. C. Zipf, J. P. Doering, W. G. Fastie, and R. E. Miller, Excitation of the auroral green line by dissociative recombination of the oxygen molecular ion: analysis of two rocket experiments, Planet. Space Sci. 16, 737-747, 1968.

Evans, W. F. J., and Llewellyn, E. J., Molecular Oxygen Emissions in the Airglow, Ann. Geophys. 26, 167-178, 1970.

Gadsden, M., and E. Marovich, 5577 Å nightglow and atmospheric movements, J. Atmos. Terrest. Phys. 31, 817-825, 1969.

Gulledge, I. S., D. M. Parker, S. G. Tilford, and J. T. Vanderslice, Intensity profiles of the 6300 Å and 5577 Å OI lines in the night airglow, J. Geophys. Res. 73, 5535-5548, 1968.

Hennes, J. P., Measurement of the ultraviolet nightglow spectrum, J. Geophys. Res., 71, 763-770, 1966.

Hunten, D. M., Summary panel discussion at Aurora and Airglow, 1970, Queens University, Kingston, Canada, August 3-14, 1970; and private communication, 1970.

McElroy, M. B., Excitation of atmospheric helium, Planet. Space Sci. 13, 403-433, 1965.

O'Brien, B. J., R. R. Allum, and H. C. Goldwire, Rocket measurements of mid-latitude airglow and particle precipitation, J. Geophys. Res., 70, 161-176, 1965.

Offerman, D., and U. von Zahn, Atomic oxygen and carbon dioxide in the lower atmosphere, J. Geophys. Res. 76, 2520-2522, 1971.

Roach, F. E., and L. L. Smith, The worldwide morphology of the atomic oxygen nightglows, Aurora and Airglow, ed. B. M. McCormac, Reinhold, New York, 29, 1967.

Schiff, H. I., Neutral reaction rates of aeronomic interest, Ann. Geophys. 25, 815-818, 1969.

Von Zahn, U., Mass spectrometric measurements of atomic oxygen in the upper atmosphere: a critical review, J. Geophys. Res. 72, 5933-5937, 1967.

Wallace, L., and M. B. McElroy, the visual dayglow, Planet. Space Sci. 14, 677-708, 1966.

Young, R. A., Chemiluminescent reactions in the airglow, Can. J. Chem. 47, 1927-1937, 1969.

Zipf, E. C., Relevant laboratory data, Paper presented at Aurora and Airglow, 1970, Queens University, Kingston, Canada, August 3-14, 1970.

3.4 OPTICAL INSTRUMENT QUALIFICATIONS

3.4.1 Introduction

The field of view and the optical off-axis attenuation characteristics of the telescope determine the obtainable altitude definition (δz) and the minimum sun angle (ψ_m) permitted for horizon profile measurements of scattered sunlight, stellar occultation, and airglow emissions.

The off-axis attenuation profile $T(\psi_s)$ for a given sun angle (ψ_s) shown in Figs. 3.4-1 and 3.4-2 corresponds to an f/8 Cassegrainian telescope (Fig. 3.4-3) with an equivalent 1.36-arc-minute circular field of view. The evaluation of δz and ψ_m presented herein is described in terms of the parameters illustrated in Fig. 3.4-4. The spectral irradiance at the telescope photodetector may be expressed as

$$I(z_t,\lambda) = \int_\Omega I_s(z_t,\lambda,\theta,\phi)\,T(\theta)\cos\theta\ d\Omega \left(\frac{\mu watts}{cm^2-\mathring{A}}\right) \qquad (3.4\text{-}1)$$

where

$$I_s(z_t,\lambda,\theta,\phi) \equiv I_s(z,\lambda) \left(\frac{\mu watts}{cm^2-\mathring{A}-ster}\right) \qquad (3.4\text{-}2)$$

is the line of sight radiance at the telescope due to scattering as described in Section 3.1.1. The measurement altitude z is here related to a reference tangent height z_t by the angle parameters θ and ϕ. θ is the off-axis angle of the scattered sunlight radiance I_S and $T(\theta)$ is the off-axis attenuation of $I_S(\theta)$.

$$z(\theta,\phi) = z_t + r\cos\phi \qquad \text{(km)} \qquad (3.4\text{-}3)$$

$$r = L\tan\theta \qquad \text{(km)} \qquad (3.4\text{-}4)$$

$$L = [(R+z_s) - (R+z_t)^2]^{\frac{1}{2}} \qquad \text{(km)} \qquad (3.4\text{-}5)$$

For a satellite altitude z_S = 500 km and an earth radius R = 6378 km, the 1.36-arc-minute field of view subtends a geometric altitude range of one km about the line of sight at the tangent point, corresponding to r = .5 km and θ = .68 arc-minutes. The altitude resolution (definition) relevant to the measurement process is defined in terms of the distribution of irradiance with θ or

r. Figure 3.4-5 shows the distribution of relative irradiance Γ with off-axis distance r.

$$\Gamma = I(z_t,\lambda,r)/I_{max}(z_t,\lambda,r=\infty) \quad . \tag{3.4-6}$$

The altitude resolution is then defined by twice the value of r, corresponding to $\Gamma = 63$ percent. Numerous evaluations of the ratio Γ have shown that it is very nearly independent of the radiance parameters z_t and λ for all wavelengths (in the range 2000 Å to 6000 Å) and all tangent heights (in the range 0 to 120 km). The irradiance altitude resolution of 1.1 km shown in Fig. 3.4-5 is therefore typical of the resolution expected for a satellite altitude of 500 km and is only 10 percent larger than that defined by the central field of view. A detailed analysis of the altitude definition is contained in Gray, et al, 1971.

3.4.2 Sun-Angle Limitations

The sun angle ψ_s is defined relative to the line of sight as shown in Fig. 3.4-4. The flux f of direct solar radiation impinging on the telescope detector is then

$$f = \Delta\lambda\ T(\psi_s)F(\lambda)A\ (\mu\text{watts}) \quad , \tag{3.4-7}$$

where

$\Delta\lambda$ is the bandpass of the spectral filter (Å);

A is the entrance aperture area of the detector (cm^2);

$F(\lambda)$ is the solar irradiance (μwatts/cm^2-Å);

$T(\psi_s)$ is the off-axis attenuation of the telescope.

The corresponding flux of scattered sunlight f_s is given by

$$f_s = \Delta\lambda\ I(z_t,\lambda,\psi_s)A\ (\mu\text{watts}) \quad , \tag{3.4-8}$$

where $I(z_t,\lambda,\psi_s)$ is the scattered sunlight irradiance at the telescope for a given measurement altitude, wavelength and sun angle (μwatts/cm^2-Å); as defined by equation (3.4-1).

The ratio of f_s on f $[f_s:f]$ defines a signal-to-noise factor

$$\epsilon \equiv \epsilon(z_t,\lambda,\psi_s) = \frac{I(z_t,\lambda,\psi_s)}{F(\lambda)T(\psi_s)} \quad , \tag{3.4-9}$$

for that part of the signal noise introduced by the direct solar radiation. Degradation of the measurement signal therefore occurs if f is greater than the equivalent noise flux f_N, due to all other sources of noise; that is, if ϵ is less than the signal-to-noise ratio f_s/f_N. For a given measurement altitude and wavelength, then, a minimum sun angle ψ_m may be defined for an arbitrary

ϵ (ϵ_0, say), such that ϵ will be greater than ϵ_0 for all sun angles greater than ψ_m. $\psi_m(\epsilon_0, z_t, \lambda)$ may be obtained from equation (3.4-9) by fixing ϵ at ϵ_0 and solving the resulting transcendental equation for the value of ψ_s that is consistent with each $I(z_t, \lambda, \psi_s)$ and $F(\lambda)$. Figure 3.4-6 is a plot of ψ_m as a function of the measurement altitude z_t for several wavelengths and values of ϵ_0. These curves were obtained by assuming a simple linear logarithmic fit to the theoretical horizon profiles. Figure 3.4-7 is a plot of ψ_m as a function of wavelength for the case where $I(z_t, \lambda, \psi_s)$ is equal to its maximum value (see Fig. 3.1-5). These curves may be used to establish confidence limits on measurement data sets obtained with sun angles in the range of 1 to 15 deg.

The horizon profiles used to generate these curves were obtained with the MIT/CSDL single-scattering radiative-transfer model. The curves in these figures pertain, therefore, to the special case of a coplanar orbit; the values of ψ_m are somewhat conservative, since the single-scattering computation yields slightly smaller line-of-sight intensities than those yielded by a multiple-scattering computation.

The minimum sun angles associated with the maximum measurement signals for occulted starlight and various airglow emissions are shown, respectively, in Fig. 3.4-8 and Table 3.4-I. The maximum signal levels were obtained from Table 2.4-I.

TABLE 3.4-I

SUN ANGLE LIMITATIONS FOR DAYTIME AIRGLOW EMISSION MEASUREMENTS

Emitter	Wavelength (Å)	ψ_m(1:1) (Deg.)	ψ_m(10:1) (Deg.)	ψ_m(10^2:1) (Deg.)	ψ_m(10^3:1) (Deg.)
Nitric Oxide [NO]	2150	4	8	12	18
Nitrogen N_2^+[1N]	3371	9	14	20	31
Nitrogen N_2[2P]	3914	10	15	21	32
Atomic Oxygen O[^{1}S]	5577	13	19	28	50

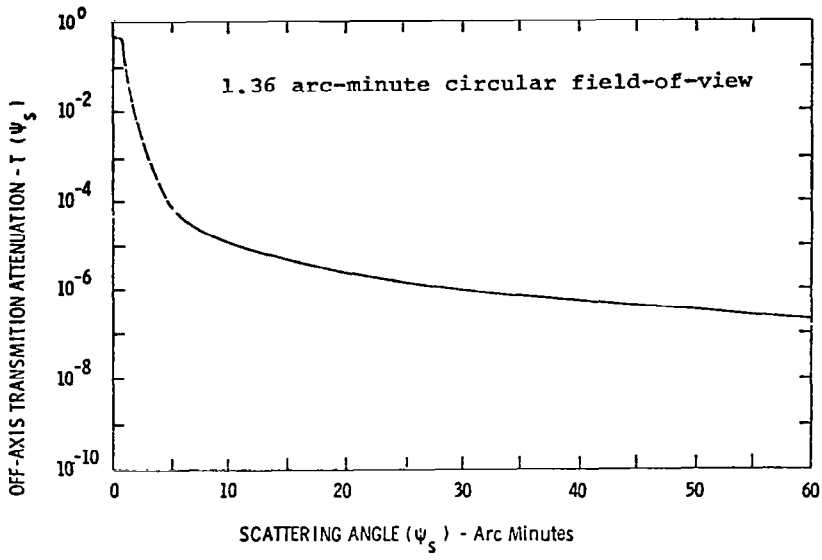

Fig. 3.4-1 The off-axis transmission attenuation $T(\psi_s)$ for a compact f/8 Cassegrainian telescope obtained with a laser source. The dashed portion of the curve represents an extrapolation of the off-axis attenuation to the on-axis transmission of 0.6.

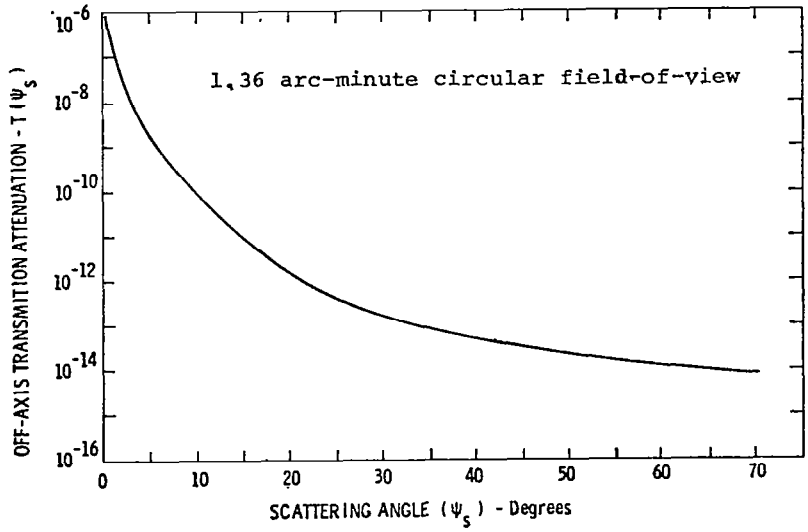

Fig. 3.4-2 The off-axis transmission attenuation $T(\psi_S)$ for a compact f/8 Cassegrainian telescope obtained with a solar simulator.

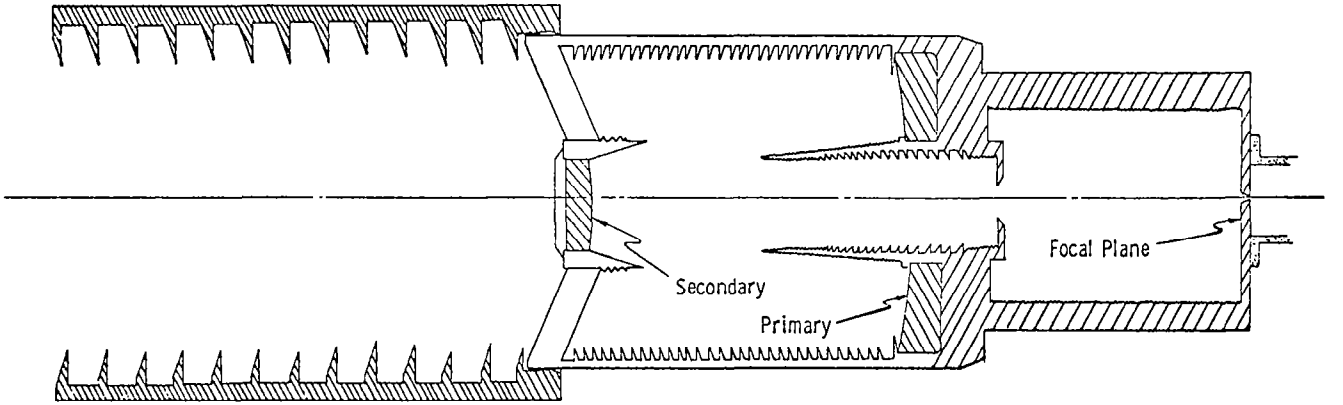

Fig. 3.4-3 Schematic of f/8 Cassegrainian Telescope and Baffle Configuration

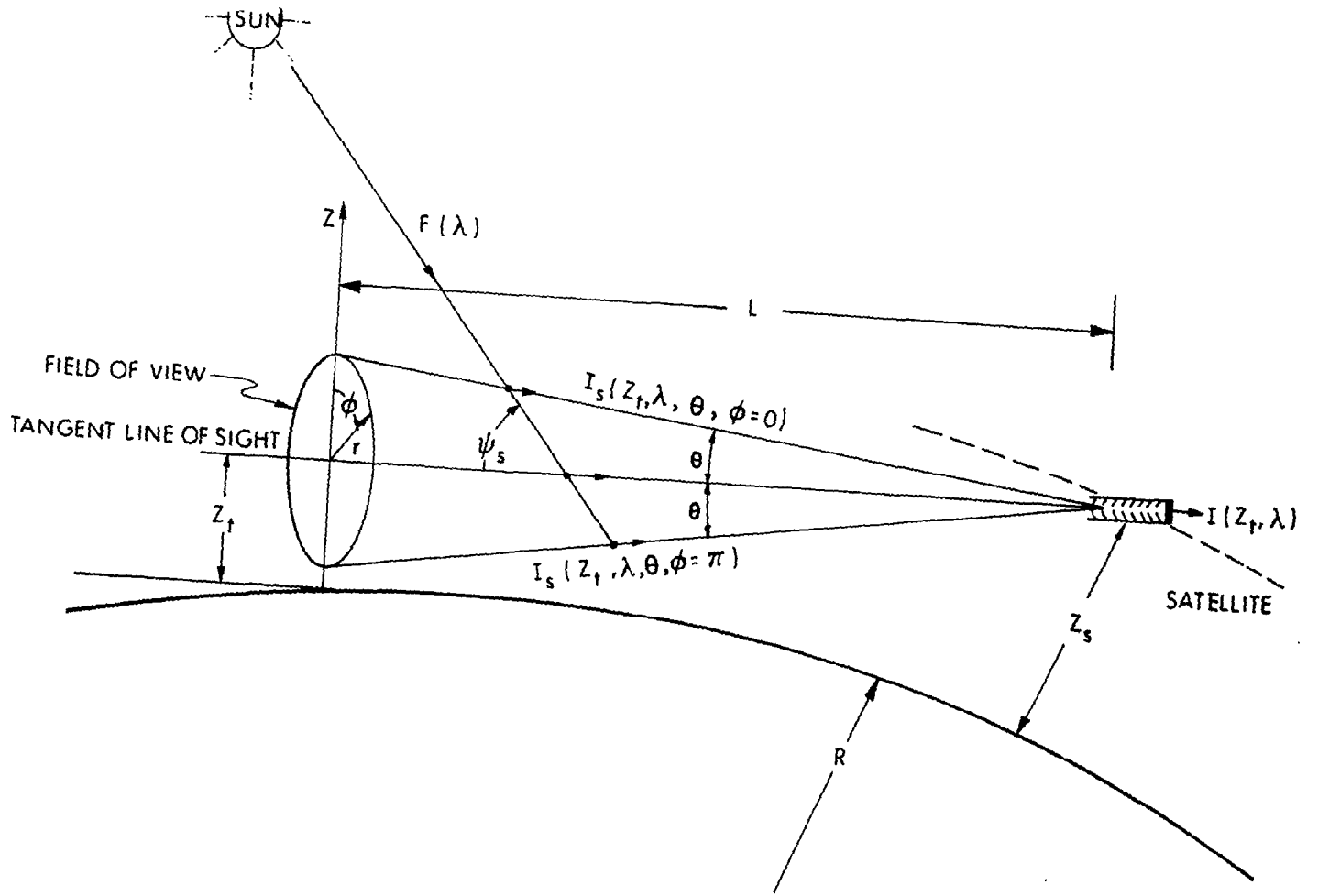

Fig. 3.4-4 The optical and geometrical parameters involved in the detection of the scattered sunlight (I_s) and the direct sunlight (F) entering the scanning telescope at angles (θ) and (ψ_s).

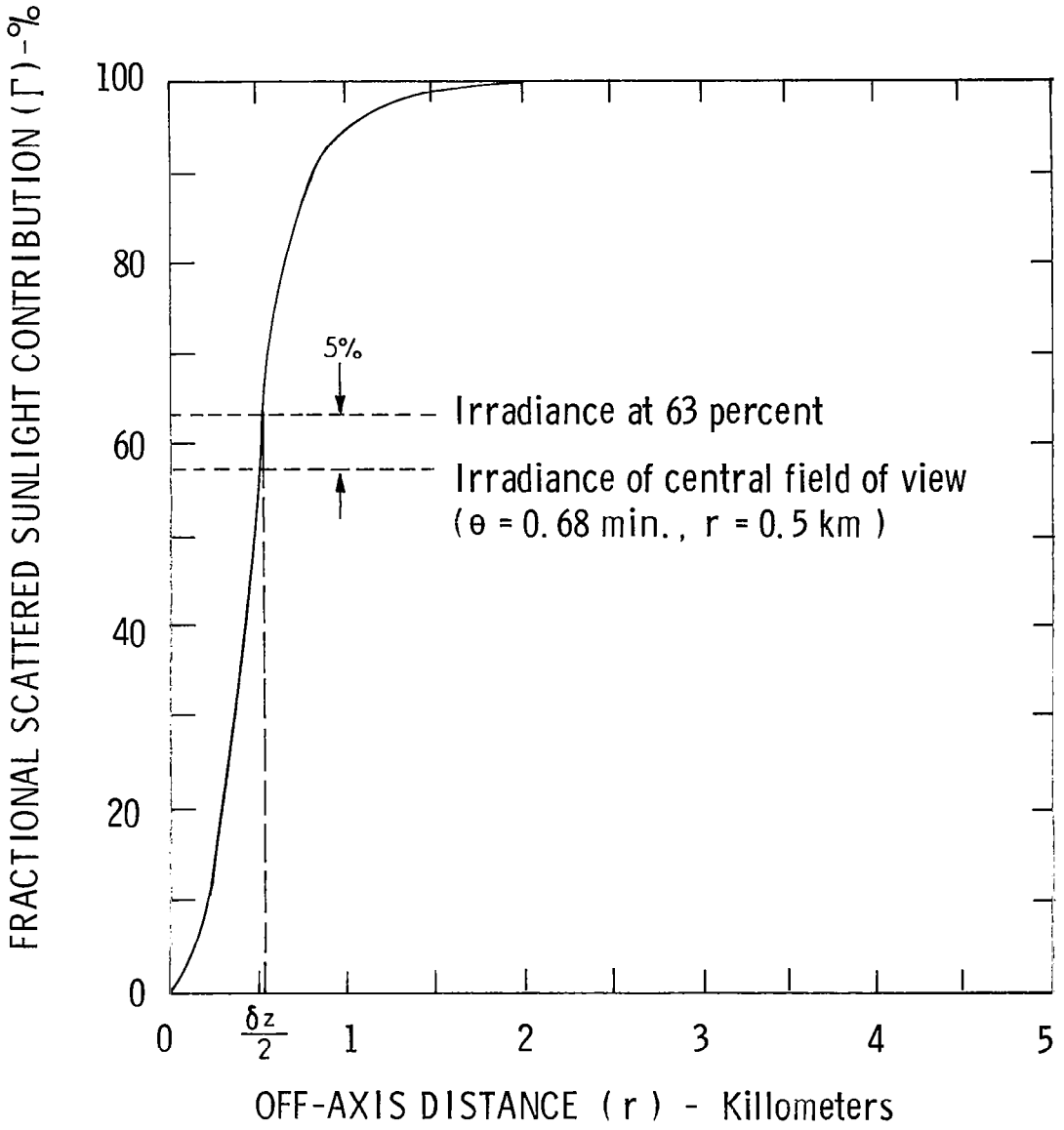

Fig. 3.4-5 The fractional contribution (Γ) of the optical telescope's total scattered sunlight vs. the off-axis distance (r) at the tangent point. The 63% criteria defines a central field of view of 1.36 arc minutes with a corresponding altitude resolution of 1.1 km.

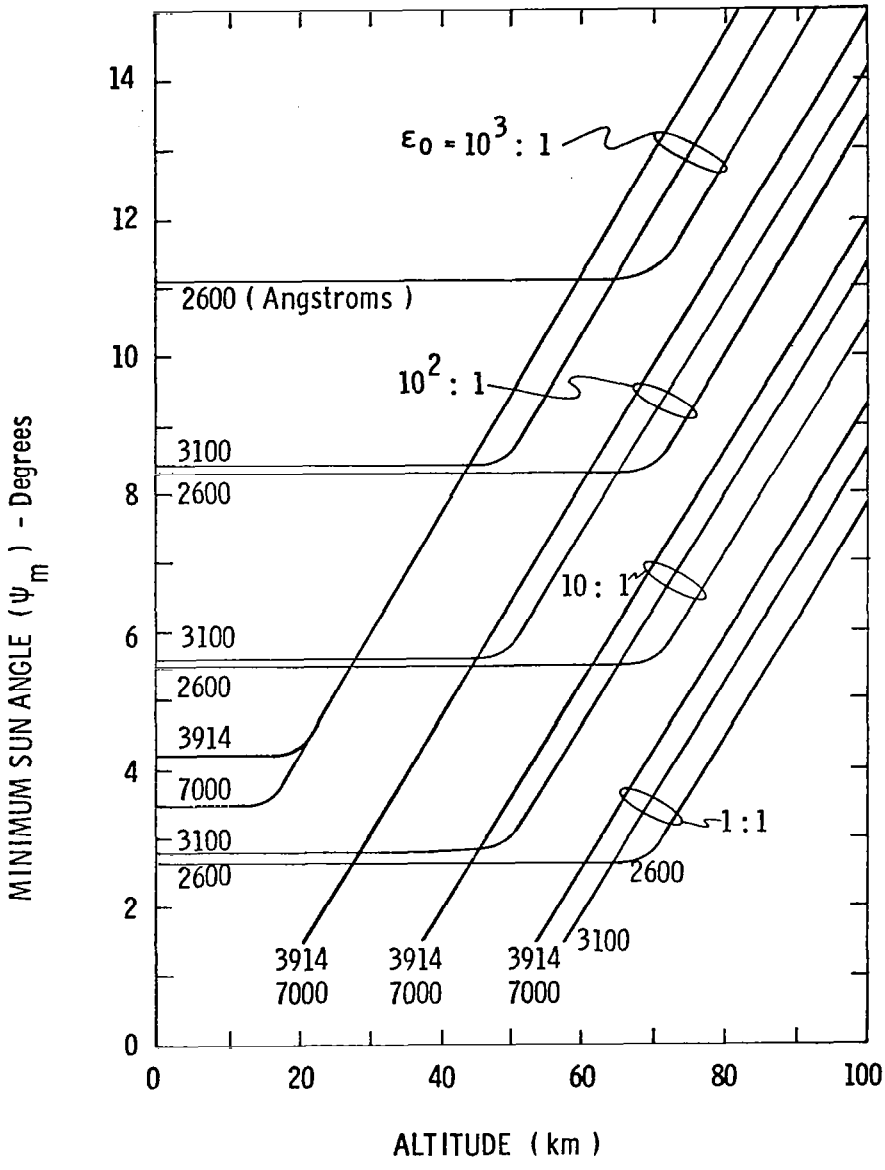

Fig. 3.4-6 The minimum sun angle (ψ_m) necessary for the measured horizon irradiances to be greater than the contribution by direct solar irradiance of the optical system. Plotted are the various irradiance ratios (ε_o) as a function of altitude for several wavelengths.

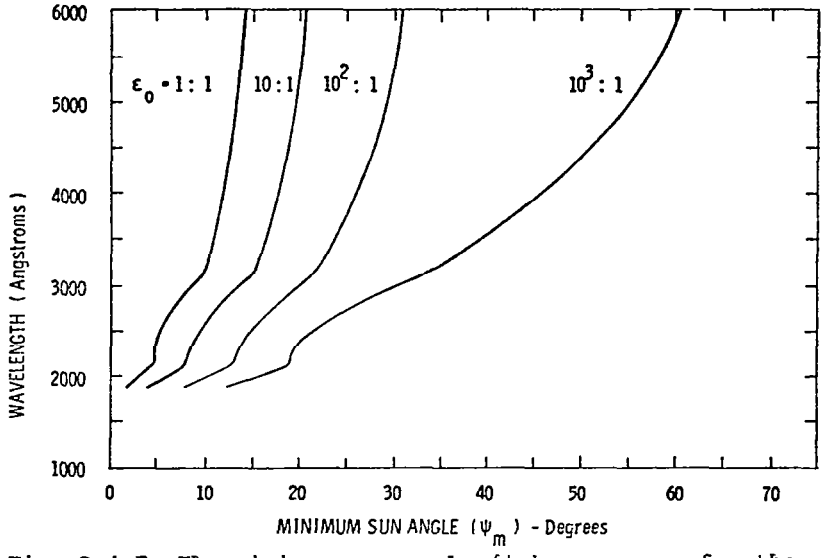

Fig. 3.4-7 The minimum sun angle (ψ_m) necessary for the maximum horizon irradiance to be greater than the contribution by direct solar irradiance at the optical system is plotted as a function of wavelength for several irradiance ratios (ε_0).

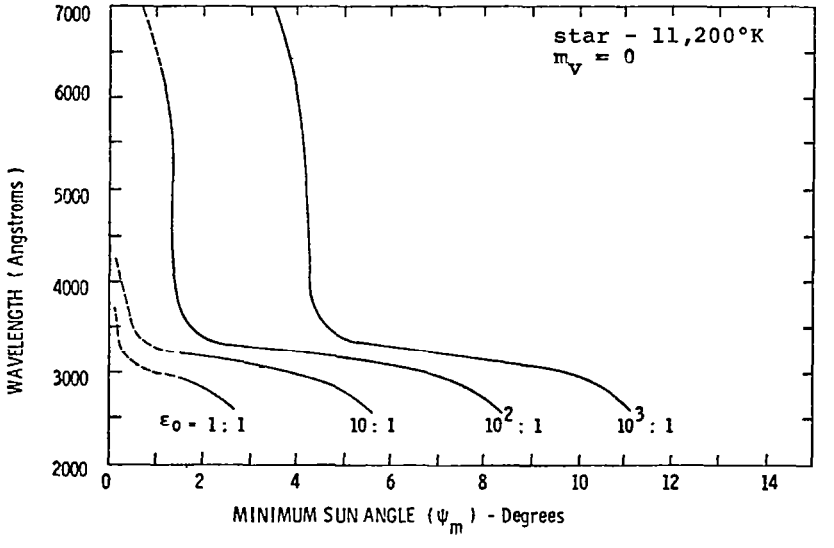

Fig. 3.4-8 The minimum sun angle (ψ_m) necessary for the maximum stellar irradiance to be greater than the contribution by direct solar irradiance at the optical system is plotted as a function of wavelength for several irradiance ratios (ε_0).

Reference for Section 3.4

Gray, C. R., Var, R. E., and Tompkins, K. L., "The Optical Altitude Resolution Obtainable with an f/8 Cassegrainian Telescope", Internal Report No. AER 9-3, May, 1971.

3.5 RADIATIVE TRANSFER MODELING

3.5.1 Introduction

In any radiative-inversion procedure, the direct modeling problem of estimating the radiation field due to scattering and absorption of radiation by the atmosphere plays an important role. The MIT limb inversion procedure requires modeling of a radiative transfer situation that is not common to other inversion situations. Unusual in this experiment are the requirements to consider both scattering and absorption of solar radiation simultaneously, to include the effects of cloud and ground reflectance, to allow for polarization effects, and to fit these calculations into the framework of a spherical geometry. Further requirements are placed on candidate radiative transfer models by other aspects of the experiment. For example, it is proposed to handle the statistics of the experiment by minimum variance, linear recursive filter techniques. This means that radiative transfer modeling errors must be small compared to uncertainties in the constituent densities so that the linear filter can be made to converge. Our desire to produce real-time data analysis requires that a transfer simulation yield acceptable accuracy with speed commensurate with the anticipated high data production rates.

Modeling radiative transfer in the earth's atmosphere is a formal mathematical and physical problem expressed by the well-known integro-differential equation of radiative transfer. This innocuous-looking equation is deceptive because analytical solution quickly becomes intractable as the complicated but real spatial distributions of atmospheric constituents are introduced into the problem. Thus, one is ultimately forced to solve the transfer equation by methods other than analytical. The computer must be programmed to generate numerical solutions.

At the outset of our radiative-transfer studies, we tried to fit our problem into the framework of previous studies. We examined several existing simulations for accuracy and speed. These investigations revealed serious problems, described in Sections 3.5.2 to 3.5.4. These had to be overcome for the Aeronomy Project—and could be overcome only with fundamental work in the mathematical aspect of modeling described in Section 3.5.5. The mathematical work that was done then permitted us to write a far more tractable and comprehensive computer algorithm, described in Section 3.5.6.

3.5.2 Simulation Techniques

For a variety of reasons, the scattering and absorption of electromagnetic radiation in the earth's atmosphere is difficult to model for horizon inversion. To begin with, the spherical geometry of the earth makes analytic solution of the equation of radiative transfer difficult. Also, the radiation originates externally from an arbitrary direction, so there is no axial symmetry to the problem. The scatterers present have arbitrary density versus altitude and are of several kinds: Rayleigh scattering by atoms, molecules, and small aerosols, as well as Mie scattering from aerosols of larger sizes. Both types of scattering are described in part by an angular redistribution phase function, which transforms input irradiance into output radiance (irradiance per solid

angle). The Rayleigh phase function is a simple, smooth function of scattering angle, but the general Mie phase function is exceedingly complicated, with a strong forward peak and much fine structure in the backward hemisphere. The Mie theory provides its functional dependence, but extensive computerized evaluation is required to put the information in usable form. Furthermore, radiative transfer involves multiple scattering. Both Rayleigh and Mie scatterers induce polarization effects that can alter the intensity output from a particular multiple scattering, so it is generally necessary to process a description of polarization state that comprises four parameters related to the well-known Stokes parameters.

3.5.3 Historical Perspective

First attempts to solve the transfer equation for horizon scan geometry were based partly on existing analytic solutions to related problems, and partly on the newly available potential of large computers. The many difficulties inherent in the problem forced the first solutions to omit the complexities of multiple scattering and polarization. To improve the accuracy of the simulation by considering these effects, a number of techniques were then tried. It was recognized that although they were powerful, existing computers nevertheless had finite limits, so that progress could only be made by formulating as much of the simulation in as analytical a form as possible. It was at first thought possible to establish analytically the radiation field in a plane parallel atmosphere and then to "bend" this atmosphere by numerical integration. However, existing analytical solutions, reviewed and extended by Chandrasekhar (1950), are limited to situations with constant mixing ratios, and phase functions that are both independent of optical depth and describable by a few terms of a Legendre series. It therefore became necessary to revert to simulations that were primarily numerical, with little analytical content.

3.5.4 Survey of Numerical Techniques

Numerical techniques for limb simulation generally share certain basic features. They usually begin with a plane-parallel configuration that is later slightly bent to conform with the earth. They treat atmospheric inhomogeneities by introducing a discrete layered structure. They convert the integral in the source term of the transfer differential equation to a sum by apportioning spatial direction to small and discrete "radiation streams" that characterize the radiances corresponding to all propagation directions whose unit vectors point within some non-zero solid angle on a unit sphere. In Monte Carlo models, of course, each photon is an individual radiation stream.

The first layer-stream simulation was developed at MIT/DL in 1968. It simulated photon-stream redistribution from layer to layer, allowing a fixed number of radiation exchanges between layers and thus modeling multiple scattering to a preselected order at all altitudes and in all directions. The geometrical framework was a flat earth, and the curvature was introduced by an integration of the radiation field over a curved path. This simulation did not handle polarization, but it was able to reproduce analytical results previously obtained for a pure Rayleigh, homogeneous atmosphere to satisfactory accuracy except at low sun angles. The main deficiencies in this program

are its inefficient treatment of multiple scattering, its lack of polarization calculations, and its inability to properly redistribute radiation at shallow incidence angles or when scattering phase functions are strongly anisotropic.

A Monte Carlo simulation, capable of producing limb profiles (but not specifically designed for that purpose) has been created by Radiation Research Associates of Fort Worth, Texas. This routine does include polarization, although the accuracy of the polarization calculations had not been verified for a general case as of this writing. With regard to limb inversion, the primary deficiency of this program is its lack of efficiency. While performing a limb radiance simulation, a June 1971 version of the code processed 10,000 photons on a CDC 6600 in a time of 20 minutes. Since a single limb scan inversion may require several limb simulations of this length at different wavelengths, the use of Monte Carlo would place a severe burden on the data processing by requiring hours of machine time for limb simulation alone.

A numerical technique that could potentially handle polarization and at the same time provide infinite-order multiple-scattering results is the so-called doubling procedure. This procedure divides the atmosphere into optically thin layers and considers the multiple scattering between adjacent pairs of layers as the sum of an infinite series, with a scattering matrix as a variable. A doubling simulation has been written at MIT/DL, but evaluation is not completed. However, because doubling requires large numbers of time-consuming matrix inversions, it is not likely that it can compete with the efficiency of the new simulation developed at MIT/DL and described in Section 3.5.6.

Another potentially useful technique is based on substituting a phase function constant in place of the usual integral in the equation of transfer for each stream. This produces linear differential equations coupled by interdependent source functions. This technique has not been fully investigated, and it is difficult to assess its potential based upon work completed thus far.

3.5.5 A New Approach to Radiative Transfer

It was felt that the Aeronomy Program required a bent plane-parallel type computerized model of radiative transfer that would be more comprehensive than any of those described above, and a model with speed sufficient to be used in real-time processing of experimental data. To enable the development of such capability, we addressed ourselves to the fundamental mathematical aspect of modeling radiative transfer (Whitney, 1971b, 1972). The mathematical ideas that were developed fall under two major headings. First, an explicit definition of superposition for forming "radiation streams" was introduced. Secondly, we took the point of view that radiative transfer could be more efficiently handled entirely in terms of 2 x 2 rather than 4 x 4 matrices.

Although streams have frequently been used in transfer modeling, the problem of explicitly forming a stream from the radiances within a solid angle seems not to have attracted previous attention. There are two significant problems that occur in connection with explicit stream formation. The first problem relates to the boundaries between different solid angles on the unit

sphere, and the second problem relates to the convention for defining linear polarization states for arbitrary propagation directions,

In treating the boundary concept, naturally one considers first the simplest kind of boundary, a distinct line. With aerosol scattering, a pathological situation is immediately apparent. The phase function is so complicated that the solid angles have to be very small. Otherwise, a change in a stream direction small compared to the average arc-distance between stream directions can substantially affect the Stokes parameters of the stream as a whole. To overcome the necessity of using very small solid angles, we defined a superposition procedure with a weighting function replacing distinct boundaries. The weighting function chosen was the square of the dot product of the nominal propagation direction $\hat{p}$ and the actual propagation direction $\hat{k}$. Some of the numerous consequences that follow from this decision are summarized in the following paragraph.

It was found for an arbitrarily complicated radiation field that the sum of any opposing streams could always be expanded in terms of at most six particular sums of opposing streams. We thus found it possible to consider a radiative transfer model with only twelve streams. The usefulness of streams generally depends on how few will suffice, and a number as small as twelve is most advantageous. We chose to distribute the twelve directions uniformly in space, as if pointing to the faces of a regular dodecahedron (see Fig. 3.5-1). We then transformed the integro-differential equation of radiative transfer to a coupled set of twelve differential equations, which is taken as the mathematical model of radiative transfer from which our computer simulation is constructed.

The mathematical model of radiative transfer described above can be characterized in summary as follows:

(1) The number of streams required is established at the minimal level of twelve, regardless of the complexity of the radiation field.

(2) With the dodecahedral arrangement, the angle between pre- and post-scattering streams can only be one of four choices: 0, $\tan^{-1}(2)$, $\tan^{-1}(-2)$, or π radians.

(3) The notion of forward scattering, usually a computational plague with aerosols, has a well-defined meaning and can be used to advantage.

(4) Only a few integrals of phase functions—and not the complicated phase functions themselves—are really needed as inputs.

Incorporating polarization in the model brings up the second major problem that occurs in connection with explicit stream formation: the choice of convention for defining linear polarization states for arbitrary propagation directions. Forming a "radiation stream" means treating different propagation directions as if they were really the same, and somehow superposing their Stokes parameters to form Stokes parameters characterizing the stream as a whole. Such superposition can be meaningful only if the convention for defining

linear polarization states for arbitrary propagation direction behaves reasonably in the region of the unit sphere that is superposed. That is, the convention should be continuous and vary uniformly from point to point on the sphere. It was found that no convention in the literature provided these properties. See, for instance, Fig. 3.5-2 which shows the conversion used by Chandrasekhar and many others. To satisfy the requirement for uniform variation, we defined a new convention which depends on the direction $\hat{p}$ of the particular stream being formed; that is, a floating convention. The linear reference directions for an arbitrary propagation direction $\hat{k}$ are obtained by rotating the vertical $\hat{z}$ axis into the nearer of + and - $\hat{p}$, then into the nearer of + and - $\hat{k}$, thus aligning the xy plane, and its linear polarization conventions, with the plane perpendicular to propagation direction $\hat{k}$ in a way that is everywhere consistent with the alignment to the plane perpendicular to $\hat{p}$ (see Fig. 3.5-3).

Application of the quadratic stream definition and the floating polarization reference to the description of scattering operators leads to the other major mathematical concept that was developed—namely, that radiative transfer could be handled entirely in terms of 2 x 2 rather than 4 x 4 matrices. Every scattering event constitues a linear transformation on the four Stokes parameters describing a radiation stream. If the Stokes parameters are arranged in a 4 x 1 column vector, then the transformation is by a 4 x 4 matrix. On the other hand, if the Stokes parameters are arranged in a 2 x 2 matrix of the form

$$S = \begin{bmatrix} S_0 - S_3 & S_1 - S_2 \\ S_1 + S_2 & S_0 + S_3 \end{bmatrix} , \qquad (3.5\text{-}1)$$

then the transformation is

$$S' = V\, S\, V^{\dagger} , \qquad (3.5\text{-}2)$$

where V is a complex 2 x 2 matrix (Whitney, 1971a). The radiative transfer model calls for stream-like integrals of these single scattering operators. It is generally true that the result of such an integration cannot be represented by simple pre- and post-multiplication on the 2 x 2 S matrix. Nevertheless, the resultant operation has only eight independent parameters, the same as an arbitrary complex 2 x 2 V matrix. In this operational sense, it is equivalent to a 2 x 2 operator.

One usually sees 4 x 4 transformation matrices in radiative transfer theory because so many computerized models work on the principle of forming an explicit overall matrix operation for transmission through or reflection from an entire layer of atmosphere. Such operators are constructed by superposing the operators for different sequences of scatters that occur in parallel. The 4 x 4 matrix operators readily superpose, and the resultant operation almost always requires the full sixteen independent parameters allowed by the 4 x 4 formalism. In the MIT model, we allow layer-operators

to be developed not explicitly, but only implicitly, as a sequence of instructions in a computer program. The program operates on the input polarization state and then superposes outputs, instead of superposing operators and then operating on the polarization state. Thus we are free to omit 4 x 4 matrices, which are not as computationally efficient as 2 x 2 transformations. By applying 2 x 2 operators, savings in storage space and computation time are achieved.

3.5.6 Computational Techniques

The computational techniques that follow from the mathematical radiative transfer model and 2 x 2 matrix point of view can be summarized as follows.

We take advantage of the dodecahedral arrangement of streams to eliminate the time-consuming calculation of cosines and inverse cosines that occur in the usual radiative-transfer models. The only angles that ever occur, either for scattering or for slant of propagation through the plane atmosphere, are 0, $\tan^{-1}(2)$, $\tan^{-1}(-2)$, and π radians. The necessary functions of these angles are precalculated and called where needed through the use of integer subscripts.

The well-defined notion of forward scattering provided by the mathematical model is used to eliminate a major cause of computing time consumption. Many computerized models use iteration on scattering order that can be interminably delayed by the strong forward peak on aerosol phase functions. Our program handles forward scattering by adjusting its optical depths, and generates the rest of multiple scattering with a tree structure that includes only nonforward scattering. The program does not iterate on scattering order, but prunes its "tree" according to a numerical criterion. That is, it jumps to the end of its loops when the projected output becomes smaller than a preset value.

The requirement for integrals of phase functions instead of the phase functions themselves is currently being met with a Simpson's rule integrator. When perfected, the integrator will be used to provide inputs analogous to those used in other radiative transfer models, so that results from our model and other models can be compared.

The omission of 4 x 4 matrices in the theory permits various savings. For each possible single scatter, we do not store sixteen real numbers for an explicit 4 x 4 matrix. Rather, we synthesize the operation implicitly using eight independent parameters for the phase function and two linear polarization references for the input and output streams. A single scatter thus requires sixteen multiplications and eight additions, as compared to sixty-eight multiplications and one hundred eighteen additions to form, and operate with, an explicit 4 x 4 matrix.

3.5.7 Results

Figure 3.5-4 shows the total radiance of a typical horizon scan plotted by our program, along with data points provided by a Monte Carlo simulation. There is good agreement between results from the two methods. However,

the two programs require greatly different amounts of computer time. Ours took on the order of a minute and a half, while the Monte Carlo simulation required twenty minutes on a faster machine.

3.5.8 Continuing Work

The original choice of a quadratic weighting function in the definition of a stream was not arbitrary, but was intended to match the quadratic nature of the Stokes parameters (noted by Wiener (1929), Wolf (1954), and others). It is suspected that the quadratic function has physical significance yet to be uncovered. Supporting this view are some general relations concerning phase functions that follow from the choice of a quadratic weighting function. We found that for any kind of particle, the sum of streams scattered in opposite directions, $P_{\hat{p}}$, satisfies a simple formula. With light incident on the scatterer from direction $\hat{z}$, and $\hat{p}$ in the z-x plane at angle ψ from $\hat{z}$,

$$P_{\hat{p}} = \cos^2\psi P_{\hat{z}} + \sin^2\psi P_{\hat{x}} \quad . \tag{3.5-3}$$

In the special case of particles not much larger than the incident wavelength, the phase function sum $P(\psi) + P(\pi-\psi)$ itself satisfies the above formula. Furthermore, the fact that phase functions integrate to unity implies that the phase function passes through $(2\pi)^{-1}$ at $\psi = \tan^{-1}\sqrt{2}$, or approximately 55°. This result qualitatively explains an empirical rule that was noted by Deirmendjian (1964).

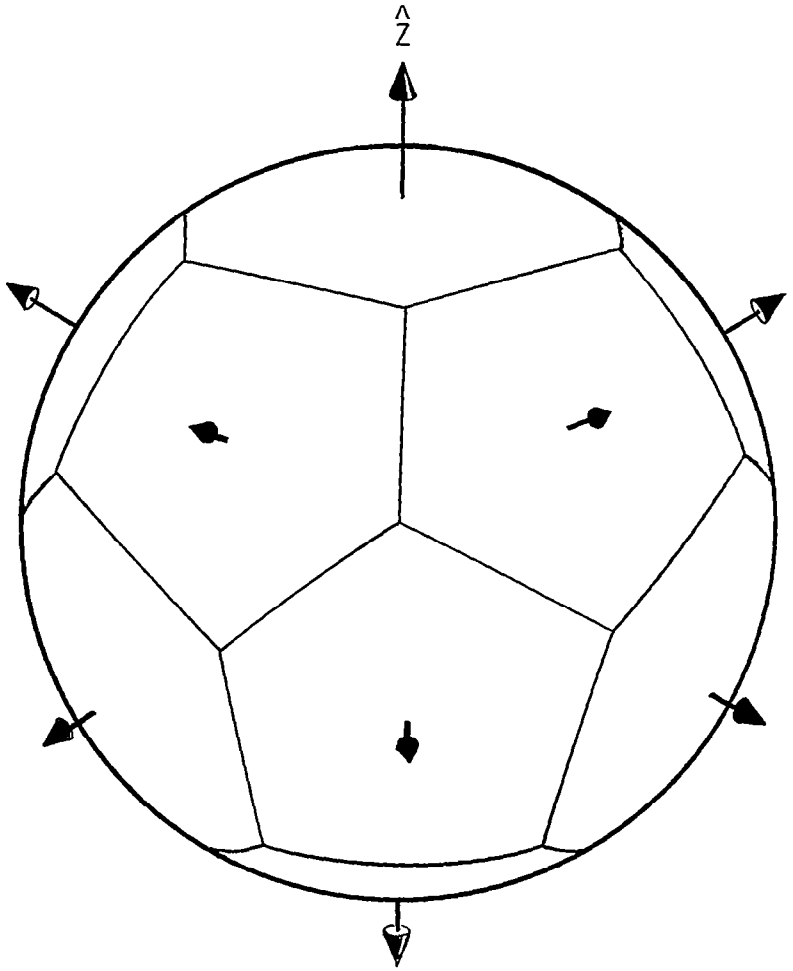

Fig. 3.5-1 Twelve Propagation Directions used in CSDL Discretized Radiative Transfer Model

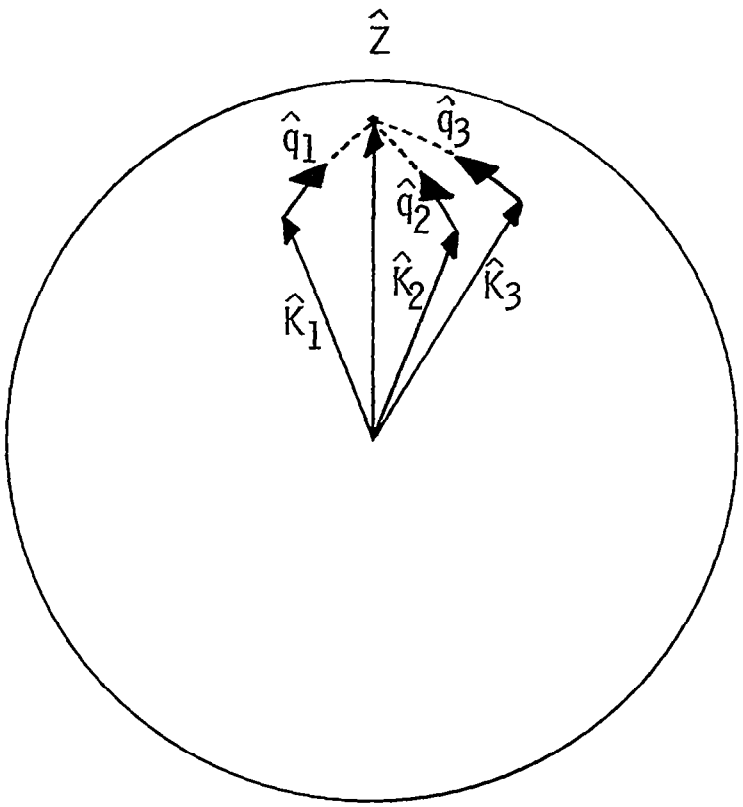

Fig. 3.5-2 Usual Polarization Reference $\hat{\underset{\sim}{q}}_1$ for Three Propagation Directions $\hat{\underset{\sim}{k}}$ in the Vicinity of $\hat{\underset{\sim}{z}}$.

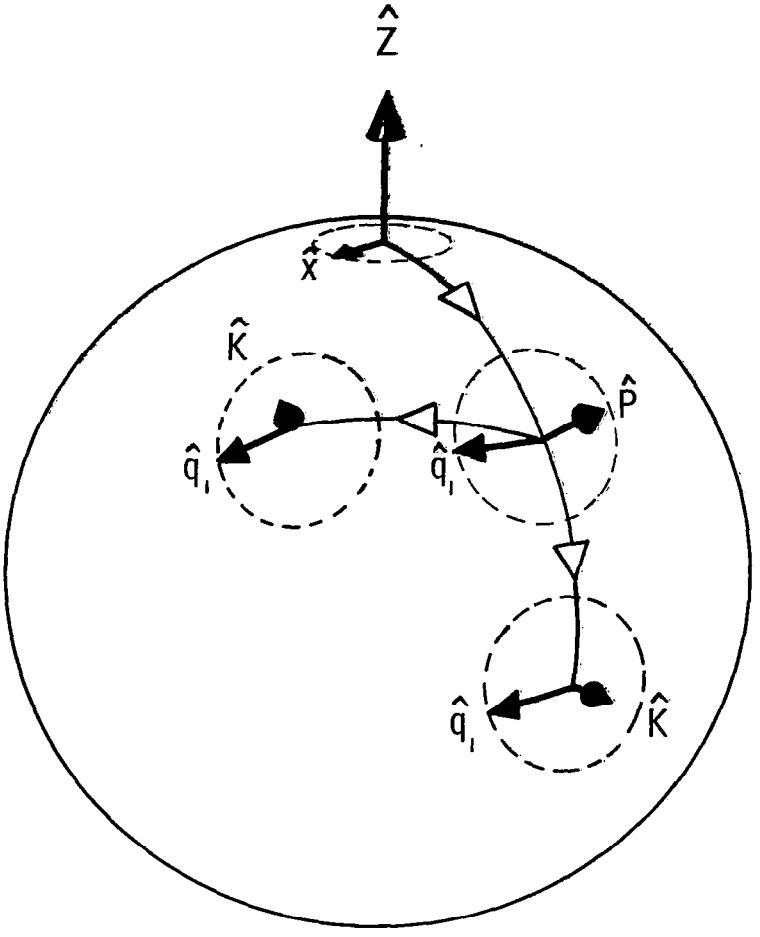

Fig. 3.5-3 Floating Polarization Reference Relative to a Nominal Propagation Direction $\hat{p}$.

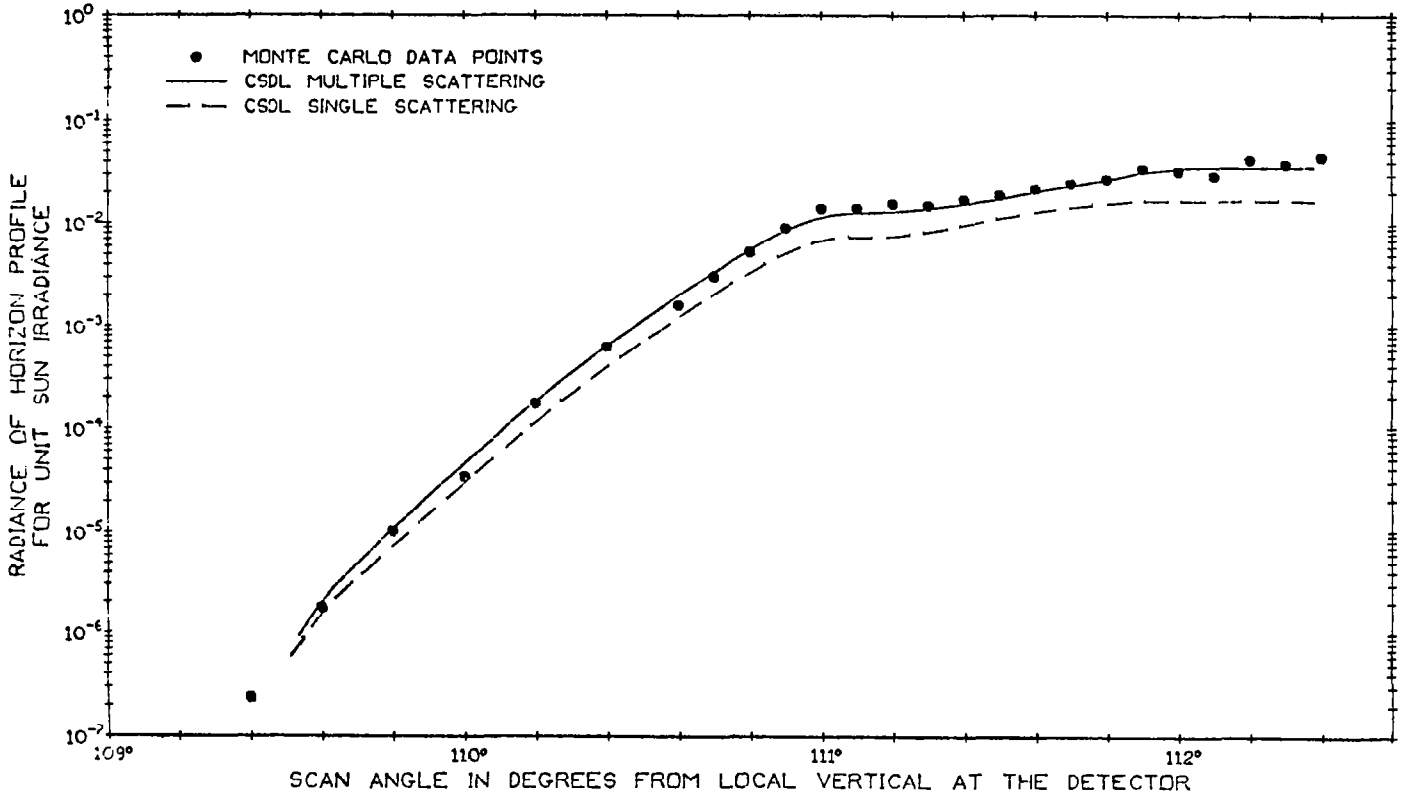

Fig. 3.5-4 Horizon Profile Scattered by a Typical Atmosphere to a Spacecraft at 500 km.

References for Section 3.5

Chandrasekhar, S., Radiative Transfer (Oxford University Press, 1950).

Deirmendjian, D., Applied Optics 3, 187 (1964).

Wiener, N., J. Franklin Inst. 207, 525 (1929).

Whitney, C., "Implications of a Quadratic Stream Definition in Radiative Transfer Theory", Internal Report No. AER 7-4, February, 1972.

_____, "Pauli-Algebraic Operators in Polarization Optics", J. Opt. Soc. Am. 61, 9, 1207-1213 (1971a).

_____, "Pauli-Algebraic Representations of Fields, Polarization States, and Radiative Transfer Phenomena", Internal Report No AER 7-2, January, 1971b.

Wolf, E., Nuovo Cimento 12, 884 (1954).

3.6 FILTERING AND ESTIMATION

3.6.1 Introduction

Optical probing of the earth's atmosphere permits inference of its constituent density and temperature profiles. Ideally, this could be done by obtaining a sufficient number of intensity measurements along various lines of sight and inverting them. However, the nonlinear dependence of intensity on density through the equation of radiative transfer, and the noise inevitably associated with measurement, make the specification of the inversion procedure a nontrivial problem. This section describes a procedure which will estimate a set of parameters, specifically the constituent densities, given a set of noisy measurements which are nonlinearly dependent upon the parameters sought. The method uses a technique initially proposed by Stratonovich (1959) and popularized for the linear case by Kalman and Bucy (1961). It is a recursive technique for minimum mean-square estimation.

3.6.2 The State Equation and Measurements

It is assumed that a finite set of parameters is to be estimated from measurements taken over some interval of time. These parameters comprise an n x 1 state vector x. The measurement is time-varying, and satisfies the equation

$$z(t) = g(x,t) + \omega(t) \quad . \tag{3.6-1}$$

Here z(t) is an m x 1 vector which represents the actual measurement. It is the sum of an n x 1 nonlinear time-varying vector function of the state plus white Gaussian noise. The measurement is made over some interval $[t_0, t_1]$.

The randomness associated with this model results from three conditions. The first is the initial uncertainty about x_0. The x_0 is generally assumed to be a Gaussian random variable with known mean and covariance. Second, the process which generates x(t) is a Gaussian random process with known statistics. Finally, the measurement is randomly disturbed by white noise. This is a fairly accurate representation for measurements under most operating conditions.

3.6.3 The Estimation Problem

The x(t) is to be estimated from observations of z(s) where s varies from t_0 to t. This type of estimation is also called filtering. To estimate x(t) given z(s), it is necessary to find the functional which relates z(s) to the desired estimate. The statistical nature of the problem dictates the structure to be used in the analysis. Since the estimate of x(t), called $\hat{x}(t)$, depends on z(s), and since both x(t) and z(s) are random, a meaningful deterministic measure of performance is a measure of the size of the error, $\tilde{x}(t)$.

$$\tilde{x}(t) = x(t) - \hat{x}(t) \quad . \tag{3.6-2}$$

Thus the structure of $\hat{x}(t)$ must be chosen to minimize some functional of $\tilde{x}(t)$. The most commonly used functional is the mean-square error, specifically,

$$P(t) = E\left[\tilde{x}(t)\tilde{x}^T(t)\right] \quad , \tag{3.6-3}$$

where $E[\ ]$ is the expectation operator and T denotes transpose. It can be shown that the $\hat{x}(t)$ that minimizes equation (3.6-3) is the conditional expectation

$$\hat{x}(t) = E\left[x(t) \middle| O_{t_0},t\right] \quad , \tag{3.6-4}$$

where O_{t_0},t is the minimum σ-field generated by the measurement process z(s). If it is possible to obtain equation (3.6-4), then this will yield the minimum mean-square error (MMSE) estimate of the random process x(t), given measurements z(s) where s goes from t_0 to t.

To obtain equation (3.6-4), it is sufficient to have the conditional probability density of x(t) given O_{t_0},t, namely, $P_x(u,t\ O_{t_0},t)$. With this, x(t) can be obtained by integration. There are other methods for obtaining estimates of x(t). A second and useful one is the maximum a posteriori (MAP) estimate of x(t), obtained by finding the x(t) which maximizes the a posteriori density $P_x(u,t\,|O_{t_0},t)$. Analyses using this technique are discussed in McGarty (1970a, b). It can be shown that linearized MAP estimators yield estimates similar in structure to those obtained by linearized MMSE techniques. Both are recursive and have identical filter structure.

3.6.4 Recursive Filters—Linearization Techniques

To obtain the MMSE estimate, it has been found convenient to first obtain the equation of propagation for the conditional density and then integrate that equation. The equation of propagation for the conditional density, called the Kushner-Stratonovich Equation (KSE), was first properly proposed by Kushner (1964) and has since then received considerable analytical attention. At the present time, there is no closed form solution to the Kushner-Stratonovich equation. Most approximate solutions require linearizations of the nonlinearities by means of a Taylor series expansion or some other suitable expansion.

For the case of a first-order inversion where latitudinal and longitudinal variations are not considered, the only non-linearity is the measurement g(x,t). The extensions of the KSE to the inversion problem are discussed in McGarty (1970c) and McGarty and Tompkins (1971). Once linearization is obtained for the second-order case, equations for the estimate and the covariance are obtained:

$$d\hat{x}(t)/dt = P(t)B^T(\hat{x},t)R^{-1}(t)\left[z(t) - g(x,t)\right] \tag{3.6-5}$$

and

$$\frac{dP(t)}{dt} = - P(t)B^T(t)R^{-1}(t)B(t)P(t)$$

$$+ \sum_{i=1}^{m} P(t)F_i(\hat{x},t)P(t)\gamma_i^T R^{-1}(t)[z(t) - g(\hat{x},t)] \quad , \quad (3.6\text{-}6)$$

where R(t) is determined by $\delta(t-s)R(t) = E[\omega(t)\omega^T(s)]$, B is an m x n matrix whose entries are the partial derivatives of the measurement nonlinearities with respect to the appropriate densities, and F_i is an n x n matrix of second partial derivatives with respect to the densities of the i^{th} component of g(x,t). The m x 1 vector γ_i has a 1 in the i^{th} position and zeros elsewhere. Equation (3.6-6) is the classical Riccati equation.

The approach just outlined to solving the filtering problem is quasi-exact due to the linearization. A less exact but quite frequently just as useful approach results if linearization is applied on the system and measurement equations first, and then the KSE are used. In that case, equation (3.6-5) remains the same, but equation (3.6-6) reduces to

$$dP(t)/dt = - P(t)B^T(t)R^{-1}(t)B(t)P(t) \quad . \quad (3.6\text{-}7)$$

Linearizing first removes the terms containing second derivatives. The set composed of equations (3.6-5) and (3.6-7) are called the linearized Kalman-Bucy equations (LKBE).

Quite frequently, the data are not provided in a continuous fashion, but discretely in time. In that case, the LKBE reduce to:

$$\hat{x}(k+1) = \hat{x}(k) + P(k+1)B^T(k+1)R^{-1}(k+1)[z(k+1) - g(\bar{x},k+1)] \quad (3.6\text{-}8)$$

and

$$P(k+1) = P(k) - P(k)B^T(k+1)[B(k+1)P(k+1)B^T(k+1) + R(k+1)]^{-1} B(k+1)P(k+1) \quad , \quad (3.6\text{-}9)$$

where $\hat{x}(k)$ is the estimate at sample time k and z(k) is the data value at time k. Similar interpretations hold for the remaining variables. Thus, equations (3.6-8) and (3.6-9) completely characterize the filter to be used in the first-order inversion routine.

Certain problems arise with linearized filters, the most serious of which is stability. This problem can usually be eliminated either by redefining the state variable or by using an alternate characterization of the filtering equations. The use of suboptimum filtering schemes also helps to maintain stable filters. Techniques used to assure stable operation for occultation inversion are discussed in Merritt (1972) and, for scattered sunlight inversion,

in Merritt (1971).

Another problem is that of incomplete state information. This is usually most evident in the lack of cross correlations that exists in the initial covariance matrix. Generally, the variance of each constituent is reasonably guessed, but the correlation between the densities at two different altitudes is not known. Thus, it is standard practice to use zero correlations. However, neutral density correlations have been obtained and are presented in McGarty and Vernam (1971) for four locations. This added information tends to improve the performance of the estimation schemes.

One of the factors limiting the present inversion routine is the a priori assumption that there are no longitudinal or latitudinal variations. These can be accounted for only when some reasonable knowledge of their structure is obtained. An attempt was made to obtain some information about these variations for neutral density, but with little success. Due to the lack of sufficient data at the present time, further attempts will likely be no more successful. Yet once the present first-order system begins to function, its output can be used to obtain information on spatial variability. With this information, spectral techniques can be used to augment the first-order state equations to include these effects (McGarty, 1970a, b).

3.6.5 Photon-Limited Filters

As finer spectral resolution is required for occultation, the amount of light intensity decreases to the point where the signal received by a photomultiplier is no longer continuous, but discrete. The discrete process is a result of the individual incident photons releasing electrons on the surface of the photocathode. The statistics of this process are adequately described by Poisson arrival times with the arrival rate of the process proportional to the intensity of light. In this case, the state is thus to be estimated by using measurements of a Poisson process whose arrival rate is the sum of one rate dependent upon the state and one rate dependent upon background noise. This differs significantly from the problem associated with a continuous measurement, where the measurement itself depends upon the sum of a nonlinear function of the state plus noise.

The measurement is a Poisson process $N(t)$, where $N(t_0)$ is zero and $N(t)$ is the number of events occurring in $[t_0,t]$. The arrival rate of the process $N(t)$ is $\lambda(x,t)$ and is given by

$$\lambda(x,t) = g(\underline{x},t) + \lambda_n(t) \quad , \tag{3.6-10}$$

where $g(\underline{x},t)$ is linearly proportional to the intensity of light observed at a satellite from a star during occultation. $\lambda_n(t)$ is due to background noise.

The estimation problem can be phrased as follows. Given $N(t)$, obtain an estimate of $x(t)$ such that it is optimum according to some criterion. Again, the MMSE criterion is chosen, and the optimum estimate is the conditional mean. The propagation equation for the conditional density of a process of this form has been recently obtained by Snyder (1970). The measurement

has been generalized so that N(t) is an m x 1 vector measurement where m different wavelengths have been measured. Thus $\lambda(x,t)$ is also an m x 1 vector. For this case, the linearized estimation equations become

$$\frac{d\hat{x}(t)}{dt} = \sum_{i=1}^{m} P(t)B(t)\gamma_i\lambda_i^{-1}\gamma_i\left(\frac{dN(t)}{dt} - \lambda(\hat{x},t)\right) \qquad (3.6\text{-}11)$$

and

$$\frac{dP(t)}{dt} = -\sum_{i=1}^{m} P(t)E_i(t)P(t) \quad , \qquad (3.6\text{-}12)$$

where B(t) is an n x m matrix of first partial derivatives of the arrival rate with respect to the state vector, λ_i is the i^{th} arrival rate, γ_i is as before, and $E_i(t)$ is an n x n matrix of second partial derivatives of the i^{th} arrival rate with respect to the state vector components. It is most interesting to note the similarity of equations (3.6-11) and (3.6-12) with equations (3.6-5) and (3.6-6), respectively.

3.6.6 Conclusions

This section has presented the basis and structure of the nonlinear recursive filtering schemes that have been employed for the constituent density inversion. These techniques are the most complete techniques presently available for such types of estimation and have been found to far surpass the *ad hoc* techniques used by former investigators. This is due mainly to the adherence to the fundamental issue of estimators and letting them govern the ultimate structure of the estimator rather than imposing some *a priori* structure and then attempting an optimization.

The performance of the estimator is best measured by P(k), the covariance matrix associated with the estimate. It can be analytically shown that P(k) goes to zero as k increases. Furthermore, it decreases quite rapidly for the finite interval case discussed in Sections 3.1 and 3.2. The only disadvantage with the recursive form of estimator is that as P(k) goes to zero, it weights the new data less and less, so that no account is taken for drastic changes. This is avoided in practice by providing adequate reinitializations.

References for Section 3.6

Kalman, R. E., and Bucy, R. S., New Results in Linear Filtering and Prediction Theory, Trans. ASME, Ser. D., J. Basic Engineering 83, 95-108 (1961).

Kushner, H. H., On the Differential Equations Satisfied by Conditional Probability Densities of Markov Processes, SIAM J. Control 2, 106-119 (1964).

McGarty, T. P., "A MMSE Estimator for the Density Inversion Problem", Internal Report No. AER 8-3, August, 1970c.

_____, "On the Constituent Density Inversion Problem-An MAP Estimator Approach", Internal Report No. AER 8-1, August, 1970a, (rev. October, 1970).

_____, "On the Star Occultation Inversion Problem-Perturbational and Recursive Estimator Structures", Internal Report No. AER 8-2, August, 1970b.

McGarty, T. P., and Tompkins, K. L., "The Estimation of Constituent Density States by an Occultation Experiment-A Quasi-Exact Solution to the Kushner-Stratonovich Equation," Internal Report No. AER 8-6, February 1971.

McGarty, T. P., and Vernam, P. C., "Altitudinal, Locational, and Temporal Correlations of Neutral Atmospheric Density," Internal Report No. AER 4-2, January 1971.

Merritt, D. C., "The Estimation of Atmospheric Constituent Densities Through the Inversion of Scattered Sunlight Measurements", Internal Report No. AER 8-7, August, 1971.

_____, "The Estimation of Atmospheric Constituent Densities Through the Inversion of Stellar Occultation Measurements", Internal Report No. AER 8-8, January, 1972.

Snyder, D. L., Detection of Nonhomogeneous Poisson Processes Having Stochastic Intensity Functions, Monograph No. 129, Biomedical Computer Lab., Wash. U., St. Louis, Mo., April, 1970.

Stratonovich, R. L., On the Theory of Optimal Nonlinear Filtration of Random Functions, Theor. Probability Appl. 4, 223-225 (1959).

3.7 AEROSOLS

3.7.1 Introduction

Because of its sensitivity to large optical depths in the horizontal rather than vertical direction—a situation characteristic of fine aerosol layers—the MIT Aeronomy Experiment is capable of locating these layers accurately and at high altitudes. Above the tropopause, where finely structured layers are often observed, aerosols become difficult to detect by ground-based measurements.

The MIT horizon-scan experiment can potentially provide, in addition to precise altitude locations of layers, information about the physical properties of the aerosols within a layer. Properties such as size distribution, total density and index of refraction can be inferred from scattered-sunlight measurements at different wavelengths and scattering angles and by using polarizing filters. Optical techniques such as these have been proposed as the optimal procedures for determining the physical properties of aerosols, because the difficulties of direct sampling can thus be avoided. (See, for example, Eiden (1971).)

Aerosol studies sponsored by the Aeronomy Program were pursued in four areas, each of which is closely related to the underlying problem of inferring aerosol physical properties from the optical measurements provided by the proposed photometer. The first area of study was concerned with a survey of experimental results (Salah, 1971b). These were examined with the aim of determining gross distributional characteristics and establishing a reference model for the inversion studies. The reference model thus derived (Malchow, 1971) is felt to be more representative of general aerosol distributional characteristics than any specific choice of measurements.

The second area of study was concerned with an examination of the optical properties of macroscopic aerosol distributions. These investigations were aimed at determining the potential of the proposed experiment to relate optical measurements to physical characteristics—and at determining if any unique relationships indeed exist between physical and optical aerosol characteristics.

In the third part of the studies, the inversion procedure was applied to a set of vertical, scattered-light measurements. Although the aim here was to check out the inversion process on a set of real measurements, aerosols were part of the state vector, and some insight into their invertibility was obtained.

Finally, an attempt was made to compare some recently obtained measurements of aerosol absorption in the visible spectral region to the stratospheric heating that was observed following the Mt. Agung volcanic eruption.

3.7.2 Survey Summary

The survey is concerned with those measurable properties that determine the scattered-light contribution from aerosols. Commonly measured quantities include the ratio, at a given altitude, of aerosol to Rayleigh scattering; the aerosol extinction cross section; the extinction wavelength dependence; the direct sample size distribution; and the angular scattering function. These measured quantities, combined with appropriate assumptions, are used generally to infer the defining aerosol physical characteristics—namely, size distribution, number density, and index of refraction. This section surveys the measurements that have been made to either infer or directly determine these physical characteristics. The distributional nature of these quantities is considered with the intention of discerning the global patterns.

3.7.2.1 Size Distribution

Various measurements and theories have produced a variety of distribution forms and particle size limits. Distribution types commonly found in the literature include power law, bimodal, and Gaussian logarithmic forms. The power law size distribution in the form $m(r) = cr^{-\alpha}$, where r is particle radius, is ubiquitous. Values of the exponent α range from 1.5 (Rosen, 1968) to 7 at 51 km altitude (Elliot, 1970). More common values seen in the literature are in the 3-to-4 range, as found, for example, by Newkirk (1964), Rosen (1968) (under certain conditions), Mossop (1965), Carnuth (1970) and Pueshel (1967). It has been suggested (Newkirk, 1964) that aerosol layers actually represent the addition of large numbers of small particles to a normal background of larger particles. If this is true, one would expect to see an increase in the effective α within layers, and such an effect has been observed by Rosen (1968).

Friend (1966) and Quenzel (1970) have proposed that the log-normal distribution is more representative of true populations. Others, notably Mossop (1965), Sherwood (1967) and Pilipowskyj (1968) have found that the correct distribution form is bimodal, with one peak in the 0.01μ region and the second peak near 0.2μ. Storebø (1970) has derived such a distribution on a theoretical basis. Mean particle radius estimates for stratospheric aerosols have been made by Bigg (1970), who found $\bar{r} = 0.1$ to 0.4μ, and Mossop (1965), who found $\bar{r} = 0.1\mu$.

The diversity of these results indicates a need for extensive further study of size distributions. Each of these measured distributions may have been representative of the aerosol population at the particular time and location of the measurement. It is important to the inversion process to be able to estimate the integral of some optical property over a particle-size distribution function. Furthermore, this has to be accomplished in terms of a selected set of parameters which describe the distribution. To successfully carry out an aerosol inversion on size distribution, therefore, one must initially know the correct distribution form. Data currently in the literature do not suggest that size distributions are sufficiently well known to perform significantly accurate size distribution inversions.

3.7.2.2 Number Densities

Near-surface aerosols have a wide range of densities related to geographic location. Because the surface distributions are highly localized, and because the MIT Aeronomy Experiment is not designed for low-altitude aerosol sensing, little effort was expended to survey these particles. Concentrations are usually assumed to diminish exponentially for the first several kilometers, and ground-level densities are, on the average, in the range of 100 to 500 particles/cm^3. The greatest experimental attention has been focused on densities within stratospheric layers. Within the layer associated with the tropopause, number densities of the order of a few particles/cm^3 have been generally found for mid-latitudes. Newkirk (1964) found 2/cm^3 over Colorado, Kent (1967) measured 3/cm^3 over Jamaica, Rosen (1968) obtained 8/cm^3 over Minneapolis and found 3/cm^3 in 1966. Bigg (1970) saw densities in the range 2 to 8/cm^3 in Australia. In the high-altitude layers associated with noctilucent clouds, Volz (1962) found densities as low as 10^{-5}/cm^3.

Since scattered-light intensity is proportional to the number density (given a fixed-size distribution), it is important to have estimates of the density, as well as the size distribution. However, the two characteristics are not necessarily independent. The theoretical work of Storebø (1970) shows a coupling between size distributions and number density. As the density increases, so does the mean radius.

The survey results show that the stratospheric aerosol layers have a latitude-dependent number density. Volz (1962) and Pilipowskyj (1968) have both assigned several times as many particles/unit volume to equatorial air masses as to midlatitude air masses. This phenomenon has been quantified by the measurements of Rosen (1968), which showed 25 particles/cm^3 over Panama, 8/cm^3 over Minneapolis, and 2/cm^3 over Ft. Churchill. Chang (1968) has shown, by analyzing the data of Elterman (1966), that total density at midlatitudes depends upon the source of the local air mass. The tropics are concluded to be a primary aerosol source region.

3.7.2.3 Altitude of Stratospheric Layers

The altitude of the tropopause decreases with latitude, and the altitude of the associated aerosol layers drops accordingly. Figure 3.7-1 shows the layer altitude locations as determined by several investigators. It can be seen from the figure that there is a gradual decrease in layer altitude from the equator northward, although the range of altitudes observed at any given latitude extends over several kilometers.

3.7.2.4 Index of Refraction

In the visible and near IR range, most investigators have assumed that aerosols are nonabsorptive and have real indices in the range 1.33 to 1.5. The value 1.5 is assumed often in the literature—for example, in the work of Grams (1967), Melfi (1969), and Volz (1969). The value 1.33, related to water spheres, has been used by Newkirk (1964). Hygroscopic sulfate has an index

of 1.42, and this substance has been found in direct samples by Bigg (1970) and Mossop (1965). Based on these findings, the value 1.4 is also often assumed (for example, Rosen (1968)). It will be important to the inversion process to have more accurate estimates of the real part of the index than merely the range 1.3 to 1.5 because this value is related to the total aerosol concentration. Newkirk (1964) stated that a change of n from 1.3 to 1.5 results in an alteration of the measured concentration by 20 percent.

Perhaps even more important to inversion is an accurate initial estimate of the complex part of the index. This value has a strong effect on the forward-to-backward scattering ratio, and, if aerosol sightings at different sun angles are to be used to deduce the size-distribution parameters, the angular scattering pattern must be known. Since water is transparent in the visible region of the spectrum, it has generally been assumed that the absorptive part of the index is zero for all aerosols except those that appear obviously colored. However, since the aerosols seem to have a more complex composition of hygroscopic sulfates, one might expect that the absorptive index might not be exactly zero. Recent measurements by Bullrich (1969) have in fact found a nonzero absorptive index in the visible region. A near-linear wavelength-dependent absorptive index was found, ranging from approximately 0.033 at 4000 Å to 0.055 at 9200 Å. These values, which some investigators consider to be too high, will require verification by other samples collected under a wide range of locations.

3.7.2.5 Aerosol-Rayleigh Scattering Ratios

A useful technique for locating aerosol layers is the laser method of sensing enhanced scattering. The enhancement is a reflected signal level higher than that expected from a pure Rayleigh atmosphere. This technique has not yielded information about aerosol physical properties, because there is insufficient information contained in the backscattering cross section to specify, for example, a size distribution. Nevertheless, it is interesting to compare results obtained by this technique at different times and locations to observe aerosol layer altitudes and relative scattering strength. The altitude of the layer associated with the tropopause has been observed extensively with lasers, and this data source has in fact shown the dependence of the stratospheric layer on the tropopausal height. Most measurements show enhanced scattering at approximately twice the Rayleigh level. Salah (1971a) surveys laser results and discusses the limitations of the method. The many laser measurements have shown the temporal variations in aerosol scattering following the Mt. Agung eruption. They have also shown the latitude dependence of the stratospheric layer density and the relationship between aerosols and the source of air masses. However, excessive reliance cannot be placed on individual measurements because it is assumed that a ratio of unity of aerosol/Rayleigh scattering exists at 30 km. This is not necessarily the case; for example, Bigg (1970) found 2 to 8 particles/cm^3 within the altitude range of 27 to 37 km.

3.7.3 Invertible Properties

Invertible aerosol physical properties are those which cause measurable optical effects. They include index of refraction, which is related to composition; number density; and size distribution, which is related to the source activity and the age of the aerosol mass. Measurable optical properties include scattering ratios at different sun angles, total intensity, wavelength dependence, and polarization. Scattered intensity ratios for single scattering at pairs of different sun angles are strongly dependent upon the index of refraction. For example, Fig. 3.7-2 shows two angular scattering functions, one with index n = 1.5 and the other with index n = 1.35 - .04i. The curves are representative of a power-law size distribution, with exponent $\alpha = 4$. The forward to backward scattering ratios are 3.1×10^3 for n = 1.5 and 1.69×10^4 for the complex index (1.35 - .04i) case. A reduction of the forward-scattered intensity would occur in the absorbing case which—for these specific indices—would make the radiation propagated forward roughly equal in both cases; but the backscatter in the absorbing case remains significantly lower by a factor of four. Similar differences are seen at other angles, for example, the absorbing case has 11 for the ratios of the scattering at 45° to that at 135°, and the nonabsorbing has 8.5. These results would be somewhat altered by the spherical geometry of a limb scan, but the qualitative effects would persist.

The effects of changes in size distribution upon the scattering at different angles can be seen in Figs. 3.7-3 and 3.7-4. The curves are constructed with varying values of the parameter α in the distribution $dN/dr = cr^{-\alpha}$.

The use of more than one wavelength will aid in the separation of size distribution from other effects. For example, Figure 3.7-5 shows the normalized wavelength dependence of scattering cross section on size-distribution parameter α. Other distributions described by other parameters or sets of parameters will result in different forms for the wavelength dependence. In fact, with the power law distribution used here, the wavelength dependence is also a function of the integration limit. Distributions with large α are sensitive to the small particle limit and small α distributions to the large particle limit.

Polarization measurements provide information similar to that provided by angular scattering functions, i.e., there are variations in polarization related to changes in size distribution parameters, scattering angle and wavelength. With respect to the size distribution parameter α, the results shown in Fig. 3.7-6 are obtained. Here, polarization at a scattering angle of 150° and a wavelength of 8000 Å is plotted versus the distribution parameter α. It can be seen that there is a gradual decrease over the range of the parameter. At 90° scattering angle, however, the effect is reversed, and polarization increases rapidly for the smaller particles (larger $|\alpha|$). Polarization also depends strongly on the index of refraction. Figure 3.7-7 is a plot of angular scattering function for two different indices of refraction. It can be seen that over most of the angular range, the radiation from absorbing particles is more strongly polarized.

In summary, aerosols have several optical effects on scattered light that are related to their physical properties. These aerosol effects are not all independent, which complicates the inversion procedure. The relationship between physical and optical aerosol parameters is most usefully defined by a system using as few special parameters as possible so that the physical characteristics of interest can be extracted with limited information input. The spherical geometry inherent in the MIT Aeronomy Experiment complicates the effects illustrated above but does not alter their qualitative application. Therefore, it is expected that by adding a proper set of size distribution parameters to the state vector used in the inversion process, one can determine the properties of the aerosols. Increases in the received signal will be related to concentration and will locate layers, the wavelength dependence of the aerosol signal component will aid in establishing a distribution parameter like the exponent of the power law, and the scattering at different sun angles will be an indicator of the absorptive properties. Polarization measurements will provide another independent input to the distribution and absorption determination.

3.7.4 An Example of Aerosol Inversion

A portion of the downlooking ultraviolet data gathered by Heath (1970) was inverted to build familiarity with the working aspects of recursive inversion. An excess of scattered UV was suspected by Elliot (1970) to be caused by an aerosol layer in the vicinity of 60-km altitude. Allowances for such a layer were made in the filter state vector with extinction coefficient and size-distribution parameter α added as state elements. The resulting inversion showed that an extinction coefficient on the order of 0.002 was probable, and that the size-distribution parameter that minimized the data variance was $\alpha \simeq 7$. The invertibility of this layer confirmed the utility of the technique, even under adverse conditions, for inverting aerosol layers. Altitude resolution was not good, which one might expect for a downlooking experiment. Also, the ultraviolet is not the best wavelength region for aerosol analysis (see Section 3.1).

3.7.5 Aerosol Heating

A cursory investigation into aerosol heating was conducted to determine if any information about stratospheric aerosol size distributions could be related to the stratospheric heating rates observed following the Mt. Agung eruption. The analysis assumed power law size distributions with distribution parameter $\alpha = 2$, 4, and the particle number densities given by Melfi (1969). The complex part of the index of refraction as measured by Bullrich (1969) was used. Results were inconclusive. They showed that heating rate would vary from about 0.001 deg/day to about 1 deg/day, depending upon the chosen size-distribution parameter. This was because a shift to larger α caused more particles of the fixed n to be shifted to the small end of the distribution, where they produce a smaller absorption cross section for the aggregate. If α was chosen to be 2, the resulting heating rate was 6×10^{-3} deg/day at 18 km. If α was chosen to be 4, the rate was 0.75 deg/day. One could conclude that any of a number of possibilities could explain these results:

a) the smaller α value is realistic,

b) the particle density is wrong and some other α applies,

c) the absorptive index of refraction was incorrect.

These various causes and effects are clearly interrelated. With the proper choices, almost any heating can be derived. One must conclude, therefore, that measurements of aerosol heating are by themselves a poor starting point for aerosol physical-property determinations.

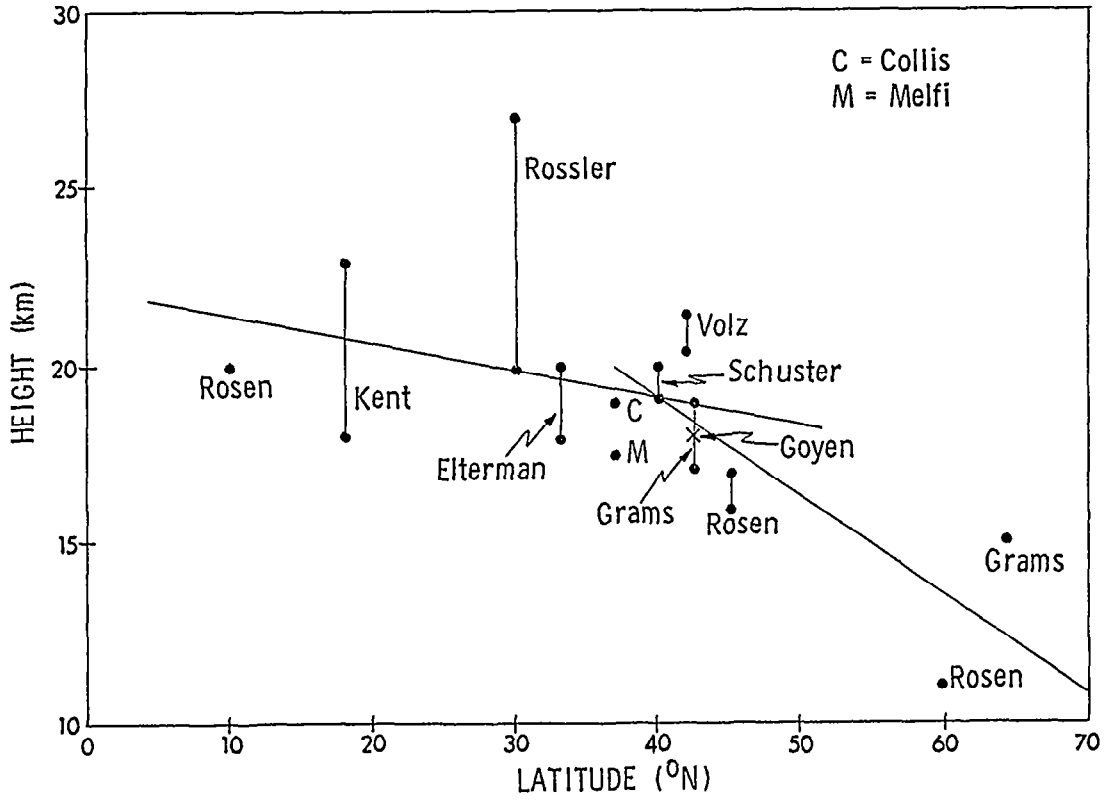

Fig. 3.7-1 Height variation of tropopausal aerosol layer with latitude.

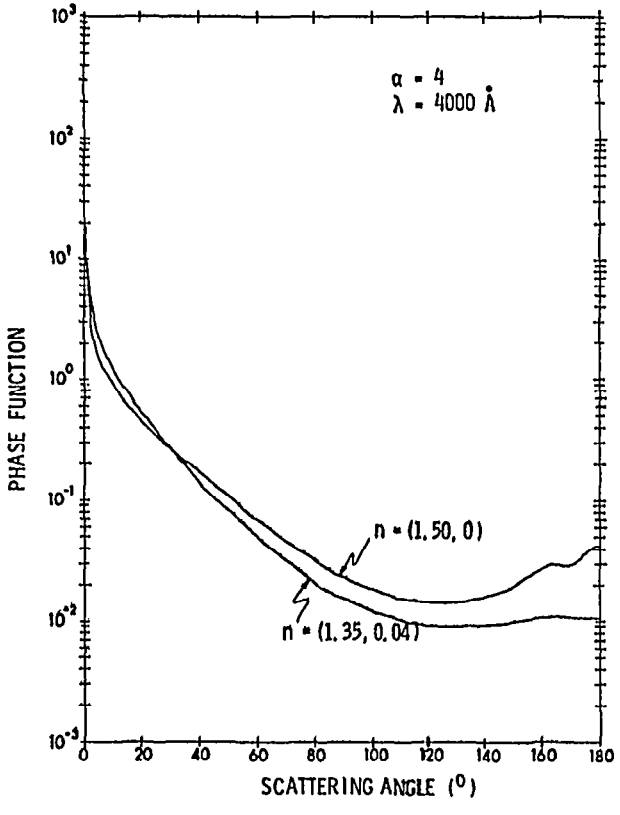

Fig. 3.7-2 Aerosol scattering pattern for two indices.

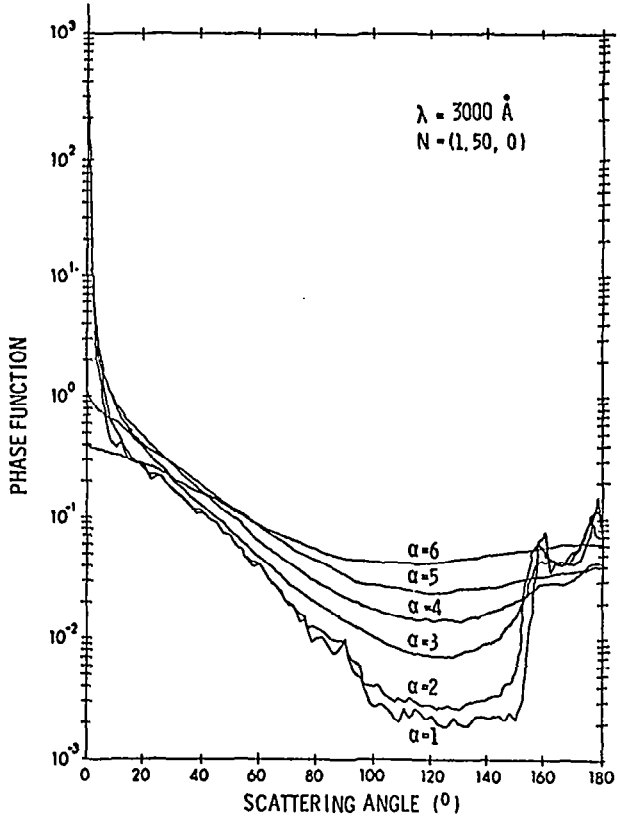

Fig. 3.7-3 A set of angular scattering curves for different size distribution parameter values. Nonabsorptive index.

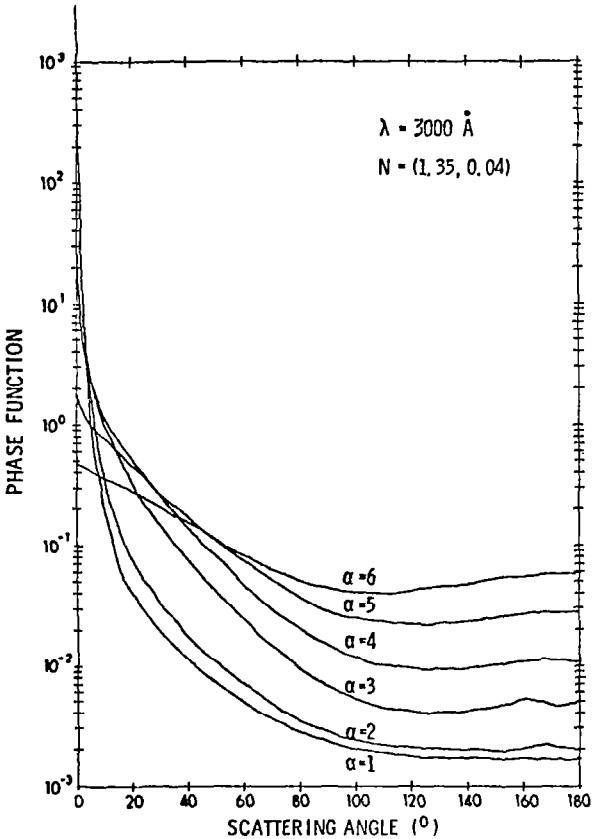

Fig. 3.7-4 Set of angular scattering curves for size distribution parameter variations. Absorptive index.

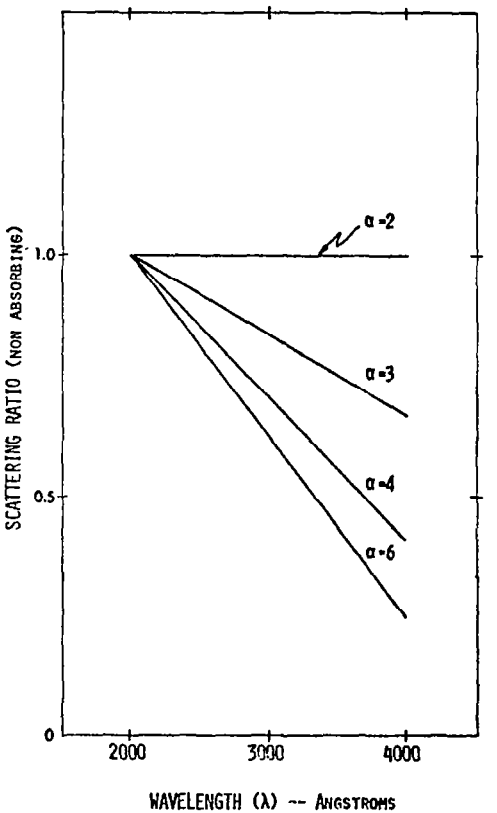

Fig. 3.7-5 Ratio of scattering cross-section at wavelength (λ) to cross-section at 2000 Å for various size distribution parameters. Nonabsorbing particles.

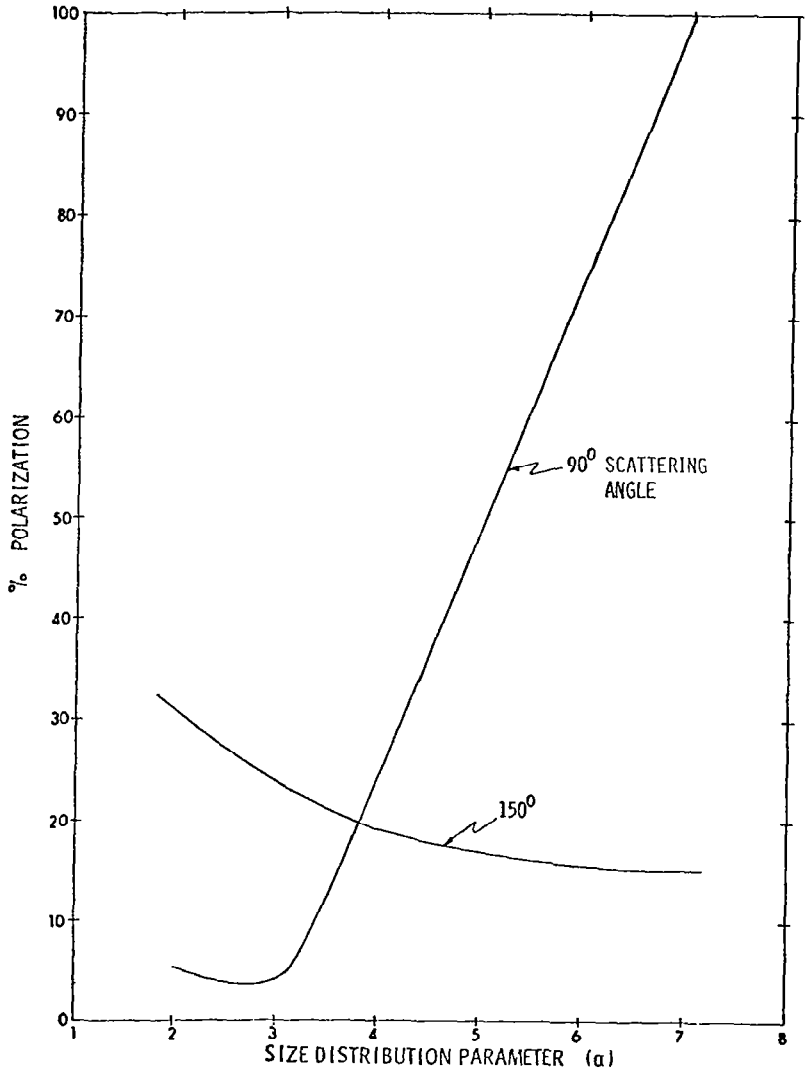

Fig. 3.7-6 Variations in polarization at two scattering angles with changes in size distribution.

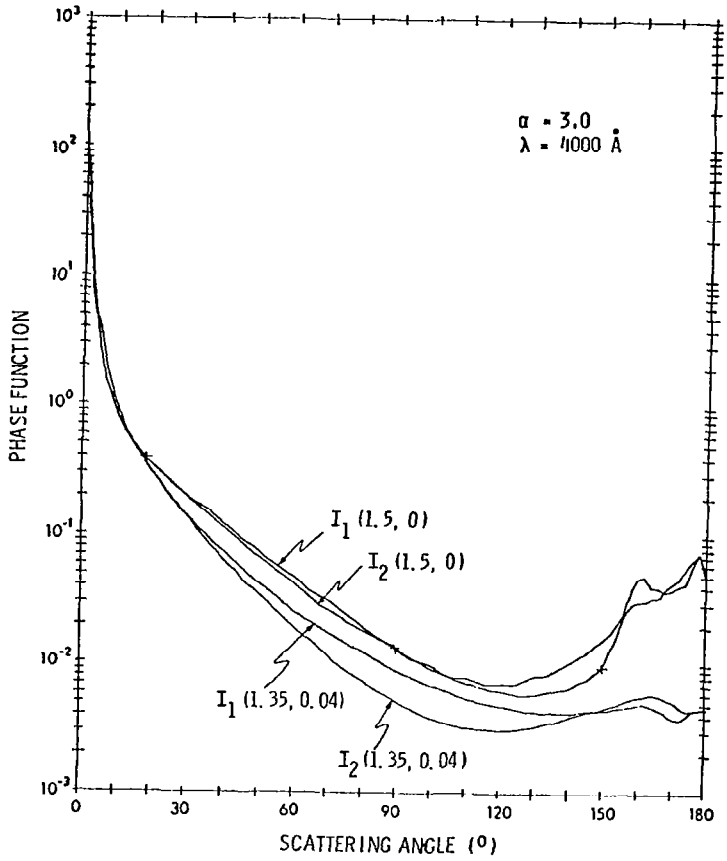

Fig. 3.7-7 Polarization intensity components I_1 and I_2 for two different indices.

References for Section 3.7

Bigg, E. K., Ono, A., and Thompson, W. J., Tellus, Vol. 12, No. 5, 1970.

Bullrich, K., et al, AFCRL Report No. 69-0266, 1969.

Carnuth, W., Journal of Geophysical Research, Vol. 75, No. 15, May 1970.

Chang, D. T., Wexler, R., AFCRL Report No. 68-0360, Sept. 1968.

Eiden, R., Applied Optics, Vol. 10, No. 4, pp. 749, April 1971.

Elliot, D. D., COSPAR Paper No. f.7, 1970.

Elterman, L., "An Atlas of Aerosol Attenuation and Extinction Profiles for the Troposphere and Stratosphere," Air Force Cambridge Research Laboratories, 66-828, December 1966.

Friend, J. P. Tellus, Vol. 18. No. 2, 1966.

Grams, G., Fiocco, G., Journal of Geophysical Research, Vol. 72, No. 14, July 1967.

Heath, D. F., Nimbus 4-BUV data, 12 April 1970.

Kent, G. S., Clemesha, B. R., and Wright, R. W., Journal of Atmospheric and Terrestrial Physics, Vol. 29, pp. 169, 1967.

Malchow, H. L., MIT Aeronomy Program Internal Report No. AER-7-1, Jan. 1971.

Melfi, S. H., Stickle, J. W., NASA Technical Note No. D-5558, Dec. 1969.

Mossop, S. C., Geochimica et Cosmochimica Acta, Vol. 29, pp. 201, 1965.

Newkirk, G., Eddy, J. A., Journal of the Atmospheric Sciences, Vol. 21, Jan. 1964.

Pilipowskyj, S., Weinman, J. A., Journal of Geophysical Research, Vol. 73, No. 24, Dec. 1968.

Pueshel, F. R., Noll, K. E., Journal of Applied Meteorology, Vol. 6, December 1967.

Quenzel, H., Journal of Geophysical Research, Vol. 75, May 1970.

Rosen, J., Journal of Geophysical Research, Vol. 73, No. 2, Jan. 1968.

Salah, J. E., MIT Aeronomy Program Internal Report No. AER 6-1, Jan. 1971a.

Salah, J. E., MIT Aeronomy Program Internal Report No. AER 6-2, Jan. 1971b.

Sherwood, R. D., Friend, J. P., Project Strap Final Report, No. NYOO-3615-1, Jan. 1967.

Storebø, P. B., Journal of Geophysical Research, Vol. 75, No. 15, May 1970.

Volz, F. E., Goody, R. M., Journal of the Atmospheric Sciences, Vol. 19 September 1962.

Volz, F. E., Applied Optics, Vol. 8, p. 2505, 1969.

3.8 OZONE—ITS THEORY AND MEASUREMENT

3.8.1 Introduction

Ozone is a trace constituent of the upper atmosphere. Even at the level of its maximum concentration, there are only six ozone molecules for one million other air molecules. Despite its scarcity, ozone acts as a major heat source and plays a dominant role in determining the characteristics of the mesosphere and stratosphere. The atmospheric motion patterns in the region between 30 and 80 km can be seriously altered by ozone absorption and radiation. Adequate theoretical description of the upward propagation of planetary waves, the behavior of the stratospheric circumpolar wind system, the better understanding of the sudden stratospheric warming and the tidal theory—these all depend on a knowledge of the distribution of ozone. Ozone can be used as a tracer to study atmospheric general circulations in the lower stratosphere and upper troposphere, and it is considered to be an important meteorological parameter. Furthermore, ozone strongly influences the distribution of many trace constituents through chemical reactions in the mesosphere, thereby affecting airglow emission and the D-region chemistry. However, due to lack of world-wide observation, especially at high altitudes, many problems remain to be solved. For example, photochemical calculations predict a very large diurnal variation of ozone in the upper mesosphere, but this has never been verified by observation.

This section summarizes the observational picture of the ozone distribution by reviewing the various ozone theories and analyzing all available data at hand. Finally, the physical causes of the discrepancies between observed and predicted ozone quantities and between theories proposed by various authors are discussed. Conclusions are advanced based on our studies. These investigations pave the way for developing our own theoretical model in the near future.

3.8.2 Global Distribution of Total Ozone

Based on the IGY-IGC data (MacDowell, 1960; Dutsch, 1969) and our analyses of the World Meteorological Organization data from 1960 to 1968 of the more than 112 stations in the northern hemisphere, it was found that the total ozone at all northern hemisphere latitudes exhibits an approximately sinusoidal variation with time of year (Griggs, 1966). Since most data are confined to the northern hemisphere, we shall refer throughout this discussion to the morphology of the northern hemisphere ozone, except where otherwise indicated. The maximum total ozone occurs in spring, and the minimum in autumn. In the tropics, seasonal changes are minor. The magnitude of total ozone in the northern hemisphere increases from the equator to a maximum at about 60°N during most of the year but to a peak closer to the pole in the spring. The distribution patterns of total ozone are different between the two hemispheres, as shown in Fig. 3.8-1. In general, between the equator and about 55° the seasonal and latitudinal variations are similar in the two hemispheres. The ozone content in the middle latitudes of the southern hemisphere is higher than in the corresponding latitudes in the northern hemisphere during late summer, autumn and winter, but poleward of 55°, the maximum total ozone in the southern hemisphere during the spring months is

smaller than in the northern hemisphere. (Wu, 1970b, discusses these comparisons.) The mean values over each hemisphere are nearly the same. London and Bojkov (1968) analyzed the variations of monthly average total ozone for both hemispheres for the nine-year period 1957-1966, and found an apparent biennial variation in the southern—but not in the northern—hemisphere.

The total ozone has longitudinal variations. Figures 3.8-2 to 3.8-5 show the quarterly average of total ozone distributions from 1960 to 1968 in the northern hemisphere. From these maps, it is seen in general that the largest amounts of total ozone are over northern North America, eastern Asia and central Europe at all seasons. Ozone varies seasonally, as previously indicated.

The amplitude of the day-to-day variations is largest from January to April and gradually decreases to a minimum in late summer and fall. The short-term variation values were associated with low surface-pressure areas and low ozone with high surface-pressure areas; in addition, low ozone values were closely correlated with the warm sector, and high ozone values occurred behind the cold fronts.

3.8.3 Vertical Distribution of Ozone

The ozone peak is located at the highest level (25 km) over the tropics, and the altitude of the peak gradually diminishes with distance from the equator. The rate of decrease with latitude is most pronounced in the spring. Below the sloping surface produced by the altitudes of the maximum ozone concentration, there exists a positive latitudinal gradient of ozone in the poleward direction throughout the year, but strongest in early spring. Above the surface formed by the maximum, the poleward gradient is negative, reaching a maximum in fall between 20-24 km and at higher altitudes in early winter. The seasonal variation of the peak height parallels that of the tropopause. The half width of the vertical profile at the peak level increases with latitude; coincidentally, the center of gravity falls to lower altitudes.

The changes in the vertical distribution of ozone concentration at any latitude in the northern hemisphere occur mainly below about 33 km (Ramanathan and Kulkarni, 1960; Bojkov, 1969). It is noted that no adequate data of vertical ozone distributions are available in the southern hemisphere to make a similar study. Total ozone above 30 km varies little either for short (day-to-day) or long (season) periods (Dütsch, 1969). Figures 3.8-6 and 3.8-7 show the three-year average vertical-ozone distributions at different latitudes over North America. The main features of these figures are (1) the ozone-concentration peak is at about 25 km near the equator and decreases to about 14 to 17 km at 76°N; (2) at the Canal Zone (9°N) and Grand Turk (21.5°N) stations, the total amounts of ozone do not vary much with season, while the other stations in the high latitudes possess ozone maxima in winter and spring. The mean meridional distributions of ozone for four seasons are shown in Figs. 3.8-8 to 3.8-11.

In view of the great importance of the vertical distribution of ozone to our model use, a detailed description of ozone variation in different height regions will be presented in the following sections.

3.8.3.1 Ozone in the Troposphere

The ozone content in the troposphere is about 9 percent of the total ozone and does not vary much geographically and seasonally (Junge, 1962). Since the region in which we are interested is well above the tropopause, it is not necessary to discuss the troposphere in detail.

3.8.3.2 Ozone in the Lower Stratosphere (15-25 Km)

About 35 percent of the total ozone is found in this region. Brewer and Milford (1960) reported that a minimum ozone concentration always occurs near 16 km at Tromso, Norway and Liverpool, England. Above the tropopause and below 25 km, the ozone content has the largest variability, and this region is primarily responsible for the observed total ozone variation. From spring to fall, ozone content in this region decreases markedly and it begins to build up with the onset of winter. Since the relaxation time is on the order of a year, the ozone in this region is strongly affected by the atmospheric circulation process.

3.8.3.3 Ozone in the Middle Stratosphere (25-35 Km)

This region contains about 35 percent of the total ozone. The variability is less than in the lower stratosphere. The relaxation time is at least one order of magnitude less than in the lower stratosphere. Bojkov (1969) referred to this region as a transition layer.

3.8.3.4 Ozone in the Upper Stratosphere (35-50 Km)

About 20 percent of the total ozone is found in this region. Because 35 km is about the balloon ceiling, the data in this region are obtained from rocket and satellite experiments. The measurements of ozone in this region are rather few, compared with those in the lower and middle stratosphere. No statistical values can be given here. However, since the ozone-relaxation time in this region is very short, the photoequilibrium condition holds quite well. Theoretically, the daily or seasonal variations of the ozone content are small. Figure 3.8-12 shows eleven observational profiles measured by rockets and satellites. This figure gives at least some idea of ozone distributions in the upper atmosphere, despite the lack of statistically significant data in this region. Generally speaking, ozone decreases exponentially with height above 30 km. The magnitude of ozone concentration is higher in summer than in winter.

3.8.3.5 Ozone in the Mesosphere (Above 50 Km)

About one percent of the total ozone is found above 50 km. Nagata et al (1968) reported that a successive small minimum and a secondary maximum of ozone concentration were detected in the altitude range between 55 and 65 km during daytime by their rocket experiments. However, no further observational data support their findings. Ozone concentration is thought to decrease exponentially with height. Figure 3.8-12 shows ozone vertical distributions in the 20-80-km range. The diurnal variation is quite large in

this region. However, it is not known exactly how ozone concentration varies during the night since only a few observations at night are available.

3.8.4 Ozone Theories

The formation of ozone involves a two-step process: first, the photodissociation of molecular oxygen into two oxygen atoms; and second, the combination of one of these oxygen atoms with a molecule of oxygen in a three-body collision. After ozone has been formed, it can be destroyed by photodissociation and by chemical reduction. A brief description of the historical development of ozone theory follows.

3.8.4.1 Oxygen Atmosphere

The first theoretical model developed by Chapman (1930) included only O, O_2, O_3 and neutral atmospheric constituents, as shown in equations (1) through (5) of Fig. 3.8-13. Later, Craig (1950), Hunt (1965), London (1967) and others made calculations based upon a somewhat similar approach. Unfortunately, the calculated values based on such a dry-atmosphere (or pure-oxygen) model result in considerably more ozone than is observed. For example, Hunt's (1965) model gave the total ozone content about three times larger than the observed value.

3.8.4.2 Oxygen-Hydrogen Atmosphere

Hampson (1964) has suggested that in the presence of water vapor, ozone can be destroyed by reaction with OH and HO_2 radicals through equations (7) and (8) of Fig. 3.8-13. These hydroxyl and hydroperoxyl radicals are created by the reaction of $O(^1D)$ with H_2O through equations (6) and (9). Hunt (1966a, 1966b) extended such concepts and showed that a reduction of a factor of 3 in the total-zone content could be achieved by employing a hydrogen-oxygen (or wet) atmosphere. However, this result is highly questionable, since it was based upon values of reaction-rate constants which are substantially greater than those used in other and more recent theories.

3.8.4.3 Oxygen-Hydrogen-Nitrogen Atmosphere

Equation (10) of Fig. 3.8-13 shows that ozone will be destroyed by nitric oxide. Therefore, if the nitrogen molecule is included in the model calculation, a different value of ozone concentration should result. Keneshea (1967), Sekihara (1968), Nicolet (1970) and Shimazaki and Laird (1970) all have pointed out the importance of including nitrogen gas. For example, the calculations made by Shimazaki and Laird (1970) have shown clearly that both O and O_3 are greatly reduced if an O-H-N atmospheric model is used. Nicolet (1970) concluded that there is no important difference between a pure oxygen and a hydrogen-oxygen atmosphere in the stratosphere, and that the effects of the radicals of hydroxyl and hydroperoxyl are important only in the mesosphere. Since the ozone content above 50 km altitude is only about one percent of the total-ozone amount, the factor of 3 reduction in total ozone from Hampson-Hunt's theory is questionable, at least based on Nicolet's argument. In fact, Konashenok (1968), Dütsch (1968, 1969) and Dütsch and Ginsburg (1969) also expressed

opinions opposite to those of Hunt. Most recently, Johnston (1971) has stressed the importance of including NO in the ozone chemistry, and he showed by a modeling calculations that ozone is seriously reduced when NO joins the chemical reactions.

3.8.4.4 Charged Atmosphere

Above about 70 km, the reactions between the negative ion of O_2^- with both O and O_3, as shown in equations (11) and (12) of Fig. 3.8-13 should be taken into consideration. This phase of the atmosphere has been recognized recently by Keneshea (1967), Sekihara (1968) and Doherty (1968, 1970), and no model calculations have yet been made.

Both photoequilibrium and dynamic models have been examined for the first three phases of the atmosphere, but none for the last phase. The number of photochemical equations used in formulating the model varies from 4 or 5 by Chapman (1930), Craig (1965) and others, to 18 by Crutzen (1969), 28 by Hunt (1969), 36 by Hesstvedt (1968) and 38 by Bowman et al (1970) and Shimazaki and Laird (1970). Generally speaking, the results from the O-H-N atmosphere are closer to the observed ozone than those from the pure oxygen atmosphere (Hunt, 1966a, b; Crutzen, 1969; Nicolet, 1970), and the dynamic model is superior to the static model in view of better agreement with reality (Hesstvedt, 1968; Shimazaki and Laird, 1970; Bowman et al, 1970; Prabhakara, 1963; Byron-Scott, 1967; Hunt, 1969; Rao, 1970). However, upon examining the numerical values calculated by the various authors, one is surprised at their great variety, even though the same phase of the atmosphere and similar models have been used.

3.8.5 Discrepancies and Causes

The predicted value of ozone concentration and its distribution from theory do not fit the observations. From photochemical equilibrium theory, we expect a latitudinal gradient of the ozone concentrations, with maximum values in the tropics and minimum values at high latitudes; the seasonal variation should be such that the maximum ozone should occur in summer and the minimum in winter; and, as far as the vertical distribution is concerned, the peak value should exist higher than 25 km. However, world-wide experimental observations reveal that the latitudinal gradient of the total ozone amount was the reverse of that predicted photochemically, and the annual variation exhibits a maximum in spring and minimum in autumn; furthermore, the peak ozone concentration occurs at about 25 km.

Although the spring anomaly of the latitudinal distribution of total ozone has been qualitatively explained by the theory of horizontal eddy transport (Newell, 1963, 1964; Prabhakara, 1963; Byron-Scott, 1967; Hunt, 1969; Rao, 1970), other discrepancies between predicted and observed ozone nevertheless remain. Furthermore, no unique theory has thus far been propounded by theoreticians. We have extensively studied these problems during the past year. In Wu (1970a, 1971), we described the basic ozone theory, reviewed the ozone problems, and examined several major factors relevant to the disputed ozone theories. These major factors include (1) chemical reaction rates, (2) minor constituents, (3) solar intensity, (4) absorption cross section, (5)

temperature, and (6) charged gases. From these studies, we have concluded that the differing results given by various authors relate mainly to the chemical reaction rates and minor constituents. For the chemical reaction rates we have calculated the square root of the ratio of k_3 to k_4 (the reaction rates of equations (3) and (4)) which has been presented in ten papers and is plotted in Fig. 3.8-14. In the photoequilibrium state, $\sqrt{k_3/k_4}$ is proportional to the ozone concentration. We have found that the ratio ranges from 1.5 to more than 75. Distributions of the minor constituents are very poorly known. Water vapor has been measured from the ground only up to about 30 km (Mastenbrook, 1968), with but one observation so far at the tropopause (about 50 km), that by Scholtz et al (1970). There have been only a few observations of methane and carbon monoxide below the lower stratosphere (Bainbridge and Heidt, 1966; Seiler and Junge, 1969). No information exists on nitric oxide at all in the region below about 70 km. The situation for atomic oxygen is even worse—so far there has been only one observation (Henderson, 1971) in the whole stratosphere, the mesosphere and lower thermosphere. The other trace substances (OH, H, N_2, N_2O, etc.) all lack measurements. In such a poor situation, it is impossible to trace interactions with ozone and to obtain a unique ozone theory.

In Wu (1970c), we examined the absorption coefficients of ozone and compared all available laboratory data. We found that Vigroux's (1953) values are less, by a maximum of about 20 percent, than those of Ny and Choong (1932), and that Inn and Tanaka's (1953, 1959) values are intermediate between those of Vigroux and Ny and Choong. It is noted that a 34-percent difference in total ozone can result from using the laboratory data of Vigroux or Ny and Choong. The solar intensity is another factor which we reviewed (Wu, 1970d). In this report, we collected and compared the most recent solar-flux data, and selected one set of data for model use.

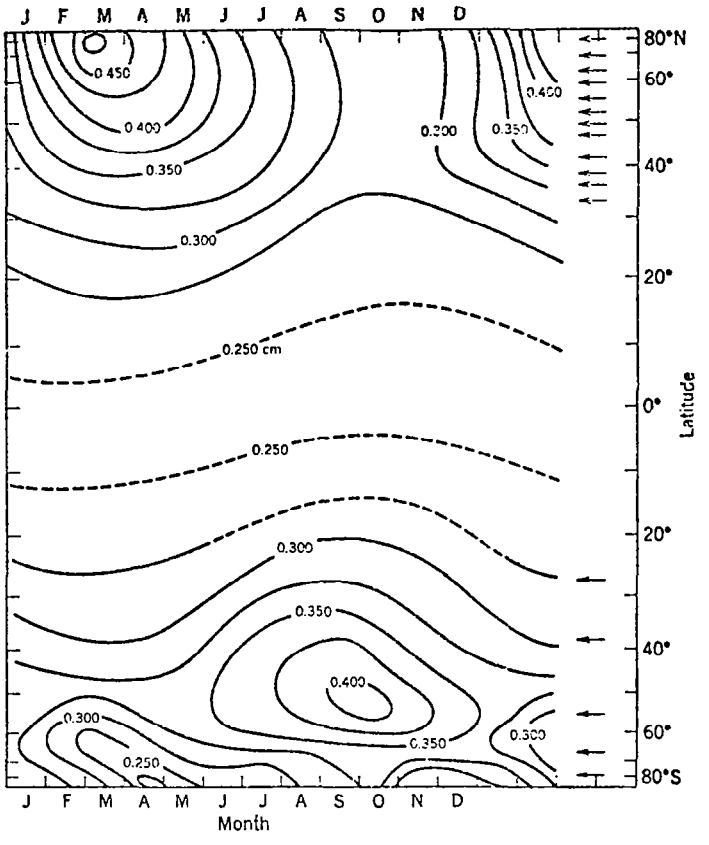

Figure 3.8-1 Total ozone distribution above ground during the IGY (after MacDowall, 1960).

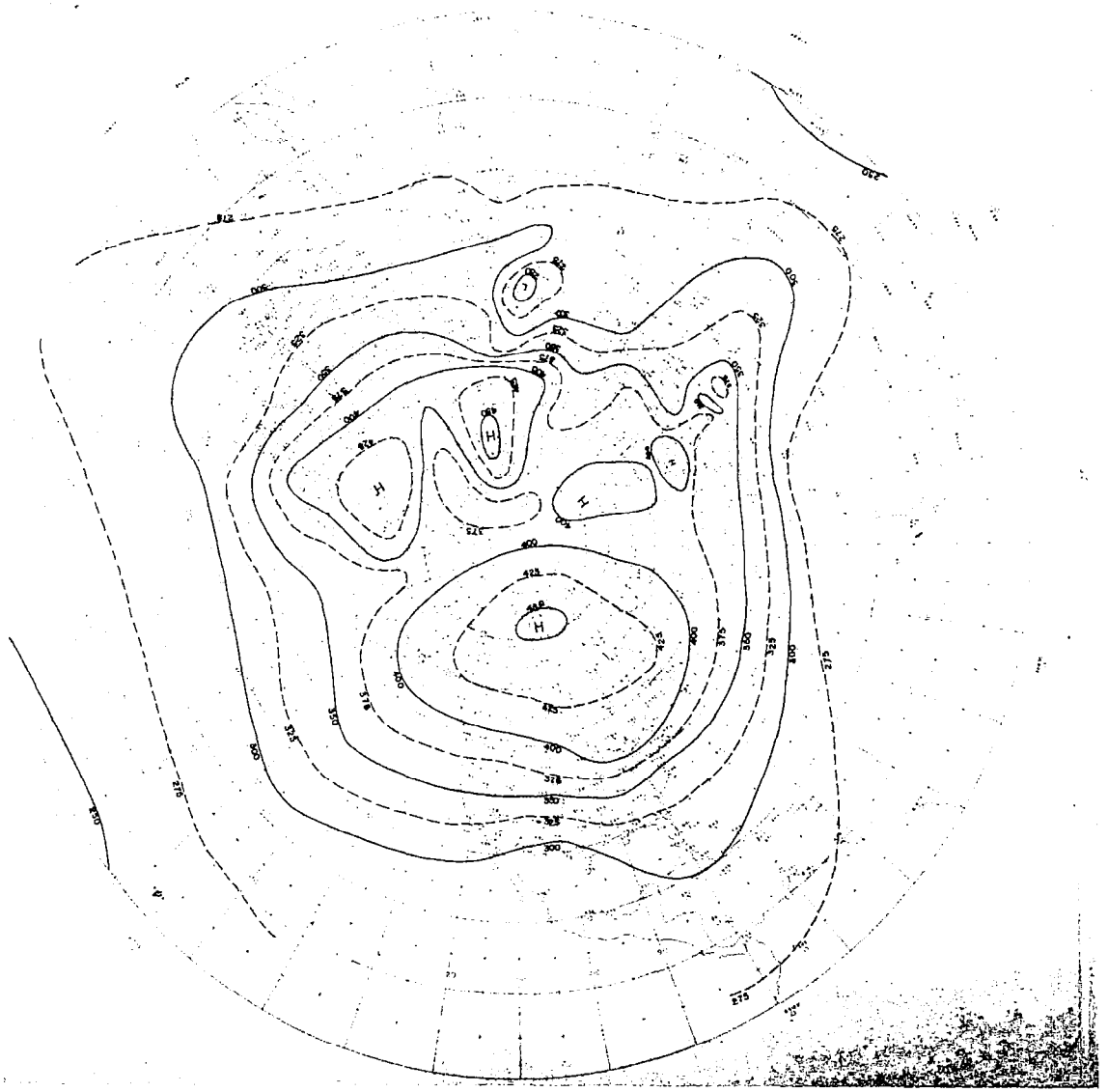

Fig. 3.8-2 World wide distribution of three-month (Mar-May) average of total ozone in northern hemisphere during 1960-1968. (Wu, 1970b)

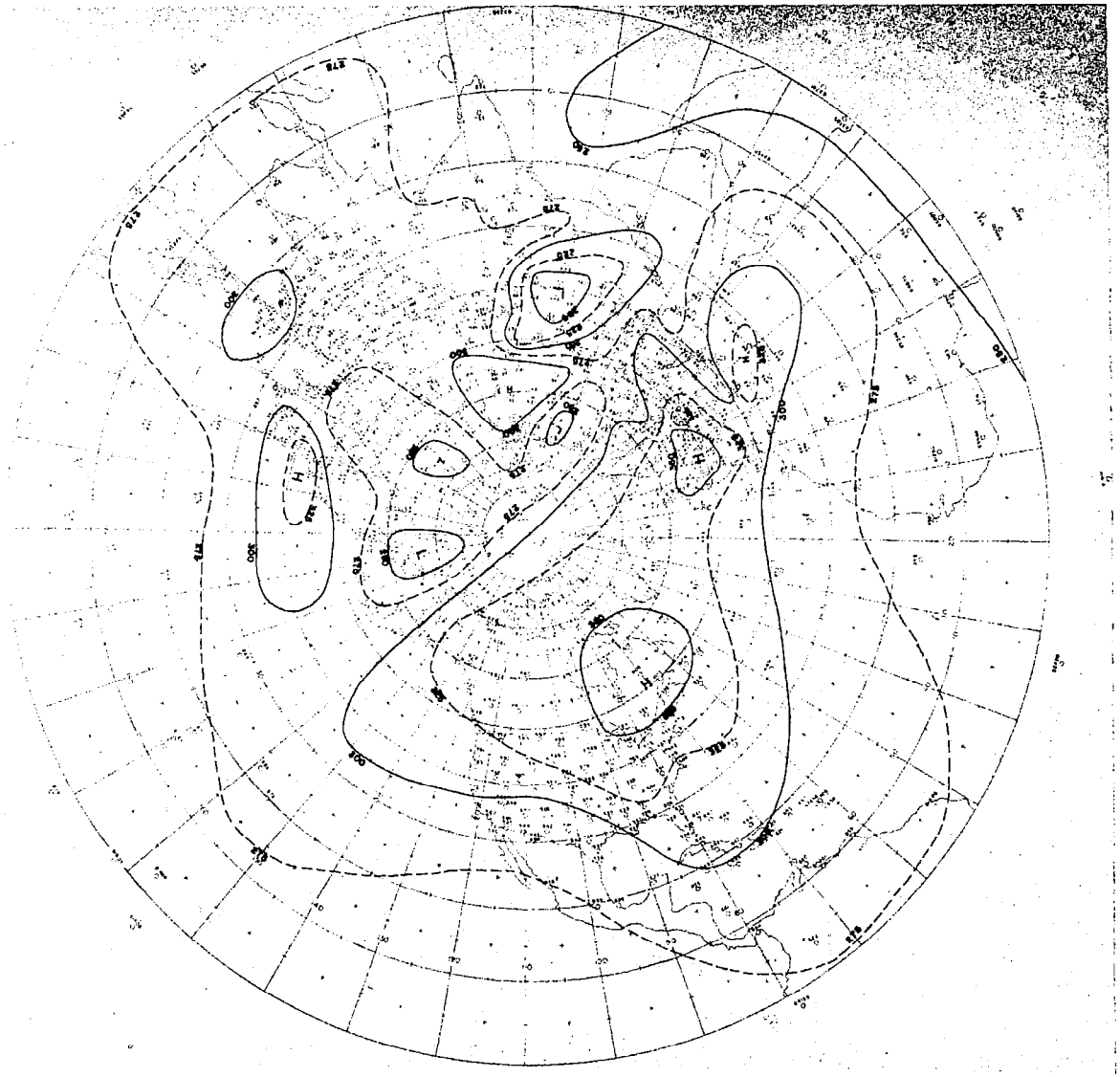

Fig. 3.8-3 World wide distribution of three-month (Jun-Aug) average of total ozone in northern hemisphere during 1960-1968. (Wu, 1970b)

Fig. 3.8-4 World wide distribution of three-month (Sep-Nov) average of total ozone in northern hemisphere during 1960-1968. (Wu, 1970b)

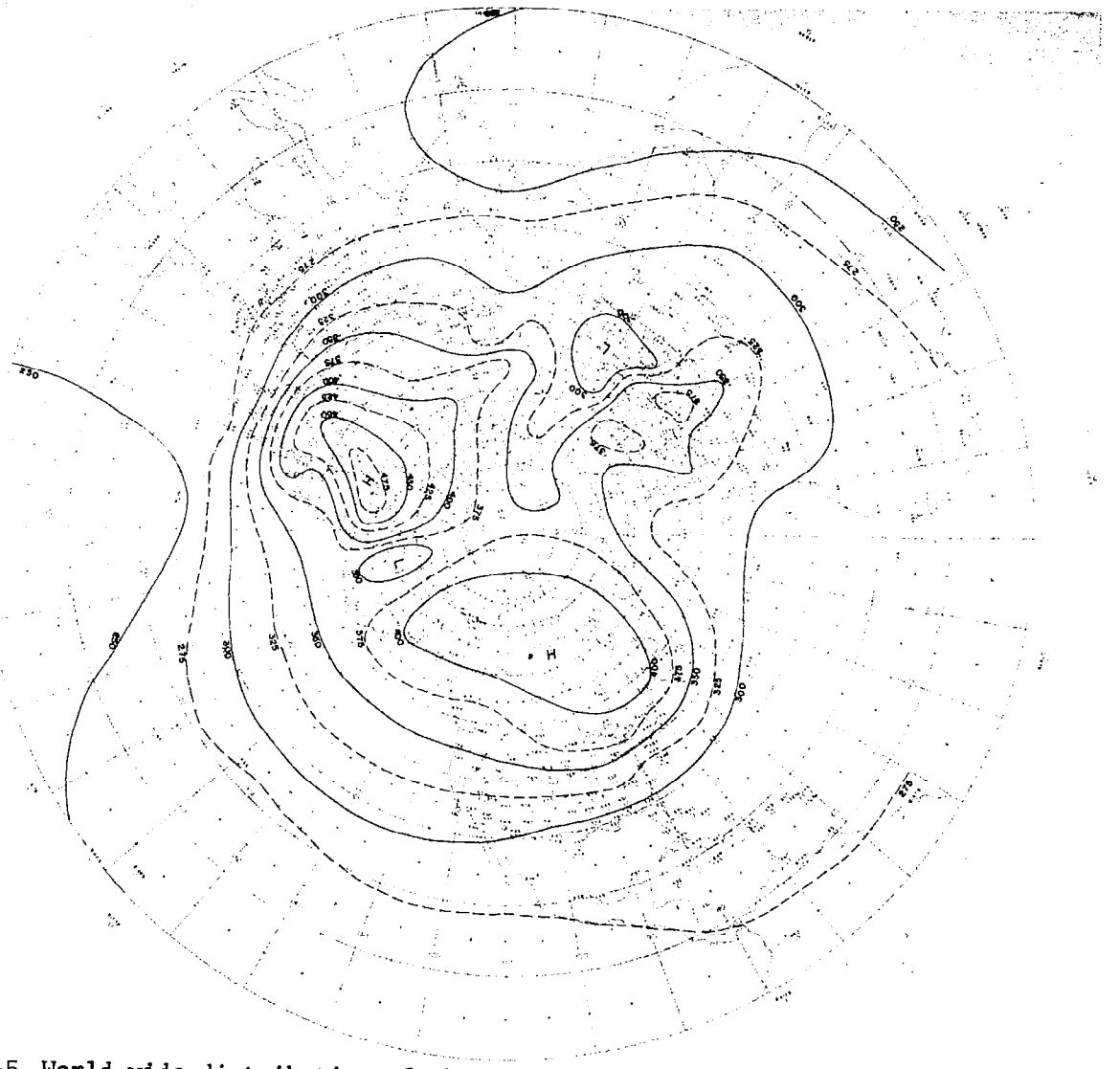

Fig. 3.8-5 World wide distribution of three-month (Dec-Feb) average of total ozone in northern hemisphere during 1960-1968. (Wu, 1970b)

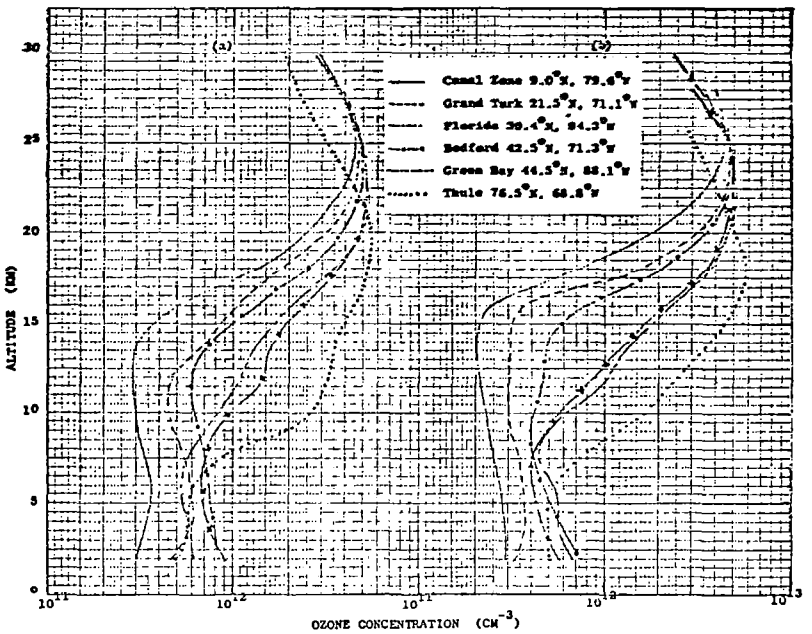

Fig. 3.8-6 The three-year (1963-65) average vertical ozone distributions at different latitudes. (a) In summer, (b) in fall.

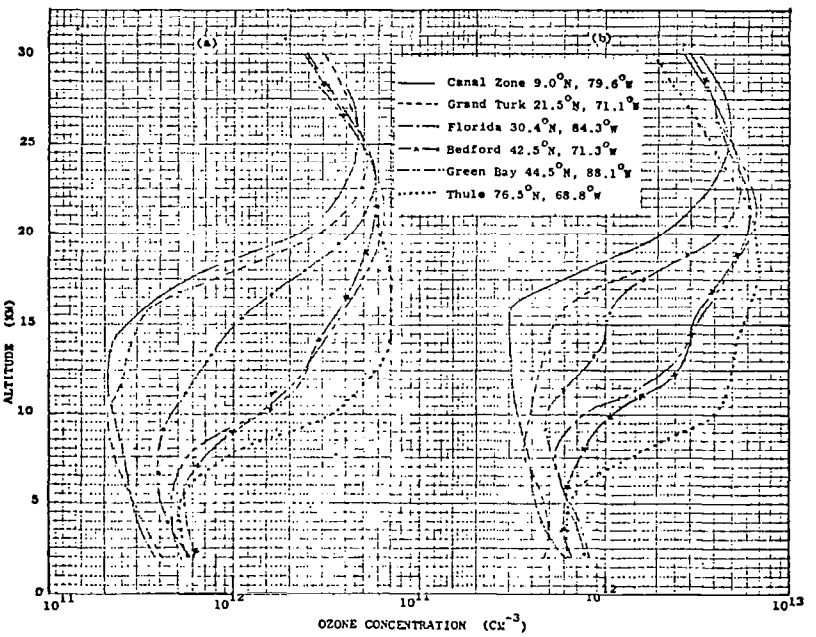

Fig. 3.8-7 The three-year (1963-65) average vertical ozone distributions at different latitudes. (a) In winter, (b) in spring. (After Hering and Borden, 1967)

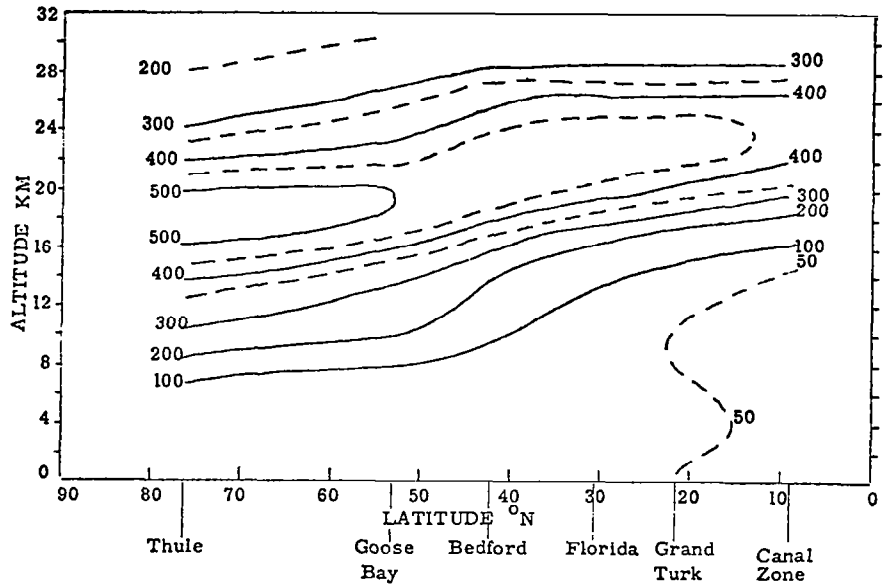

Fig. 3.8-8 Mean ozone density (10^{10} cm^{-3}) for summer, after Hering and Borden, 1967.

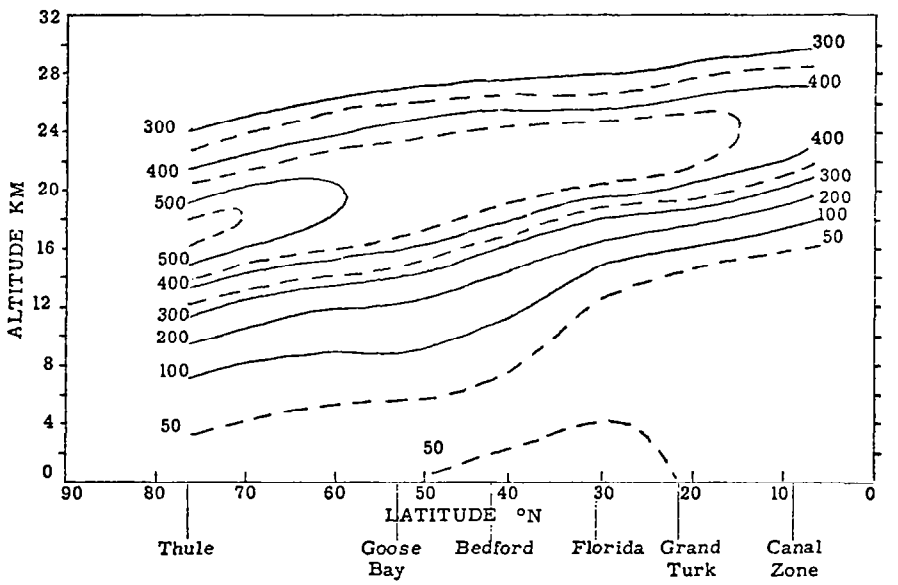

Fig. 3.8-9 Mean ozone density (10^{10} cm^{-3}) for fall, after Hering and Borden, 1967.

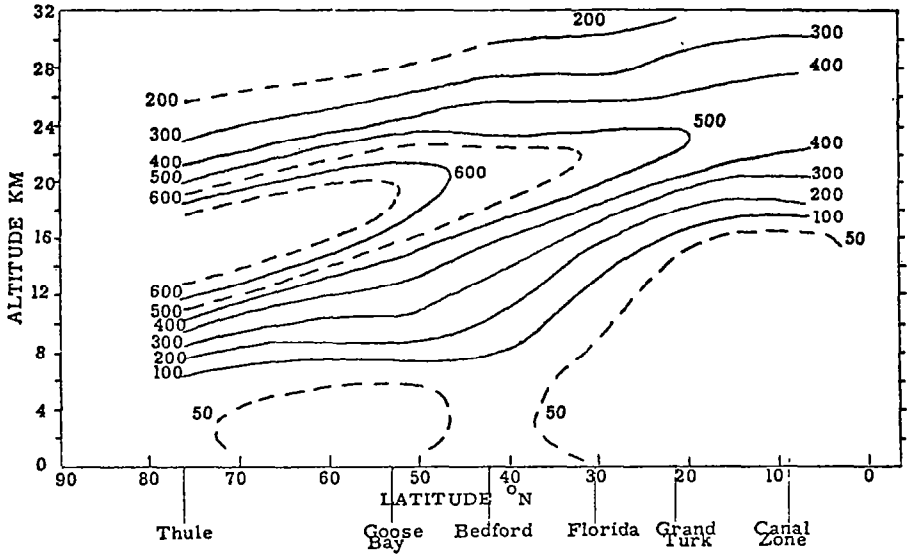

Fig. 3.8-10 Mean ozone density (10^{10} cm^{-3}) for winter, after Hering and Borden, 1967.

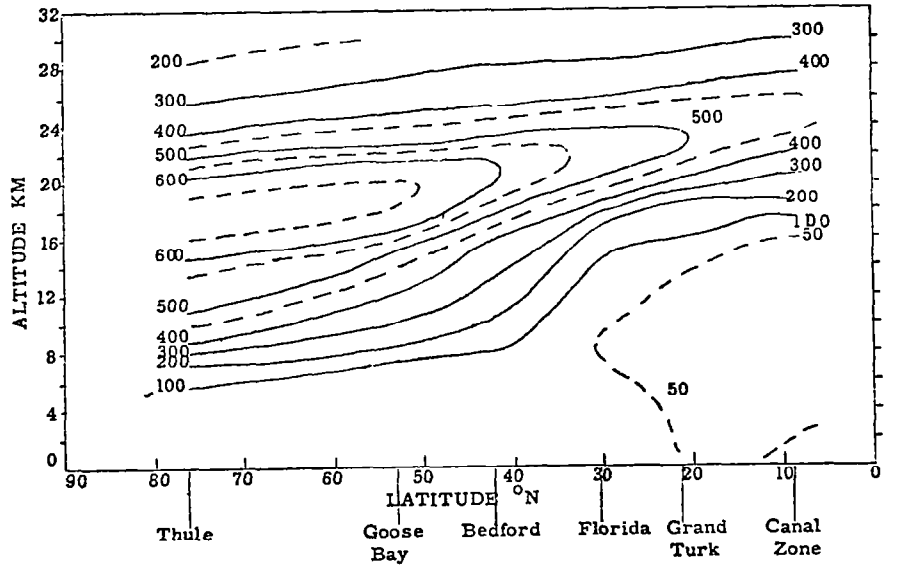

Fig. 3.8-11 Mean ozone density (10^{10} cm^{-3}) for spring, after Hering and Borden, 1967.

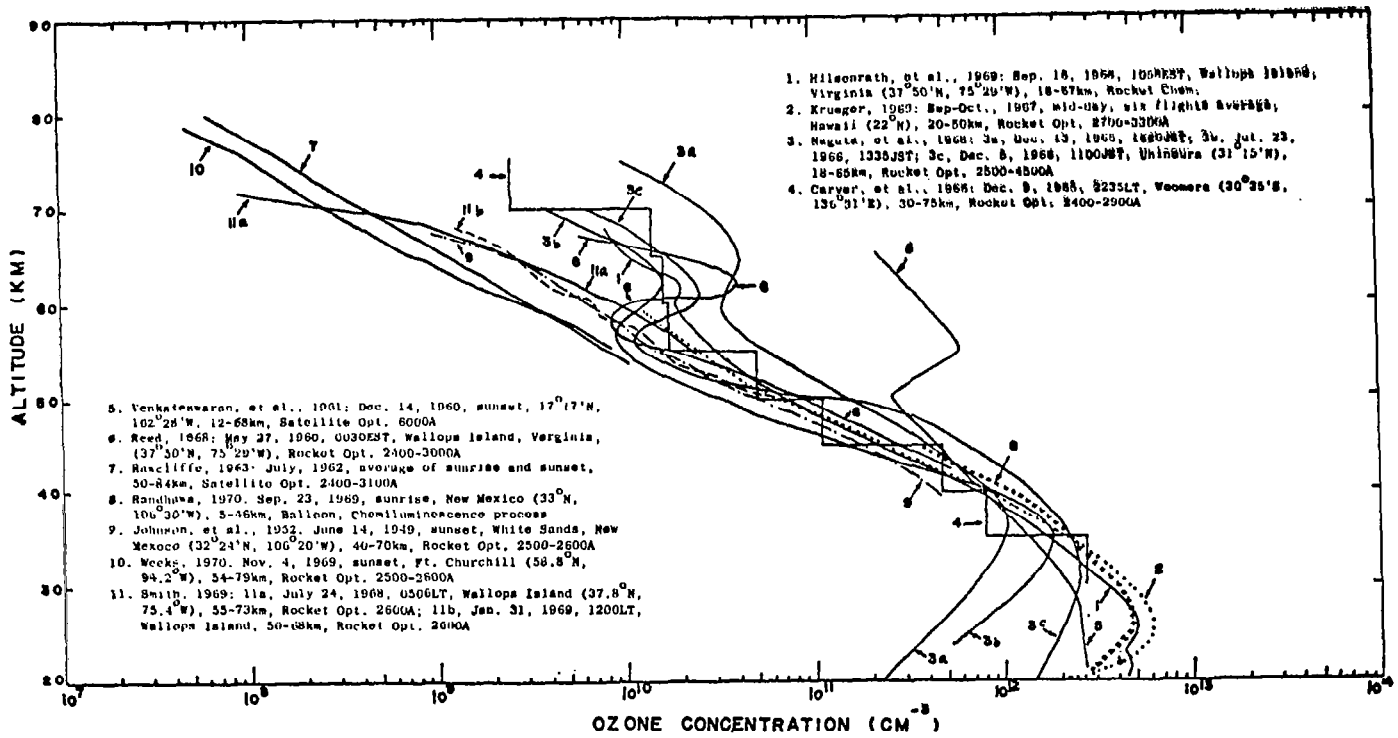

Fig. 3.8-12 Observations on ozone distributions obtained by various workers with rocket and satellite-borne instruments.

(1) $O_2 + h\nu \rightarrow 2O$ $\lambda < 2424$ Å

(2) $O_3 + h\nu \rightarrow O + O_2$ $\lambda < 11800$ Å

(3) $O + O_2 + M \rightarrow O_3 + M$ k_3

(4) $O + O_3 \rightarrow 2O_2$ k_4

(5) $O + O + M \rightarrow O_2 + M$ k_5

(6) $O(^1D) + H_2O \rightarrow 2OH$

(7) $OH + O_3 \rightarrow O_2H + O_2$

(8) $O_2H + O_3 \rightarrow OH + 2O_2$

(9) $OH + O_2H \rightarrow H_2O + O_2$

(10) $NO + O_3 \rightarrow NO_2 + O_2$

(11) $O_2^- + O \rightarrow O_3 + e$

(12) $O_2^- + O_3 \rightarrow O_3^- + O_2$

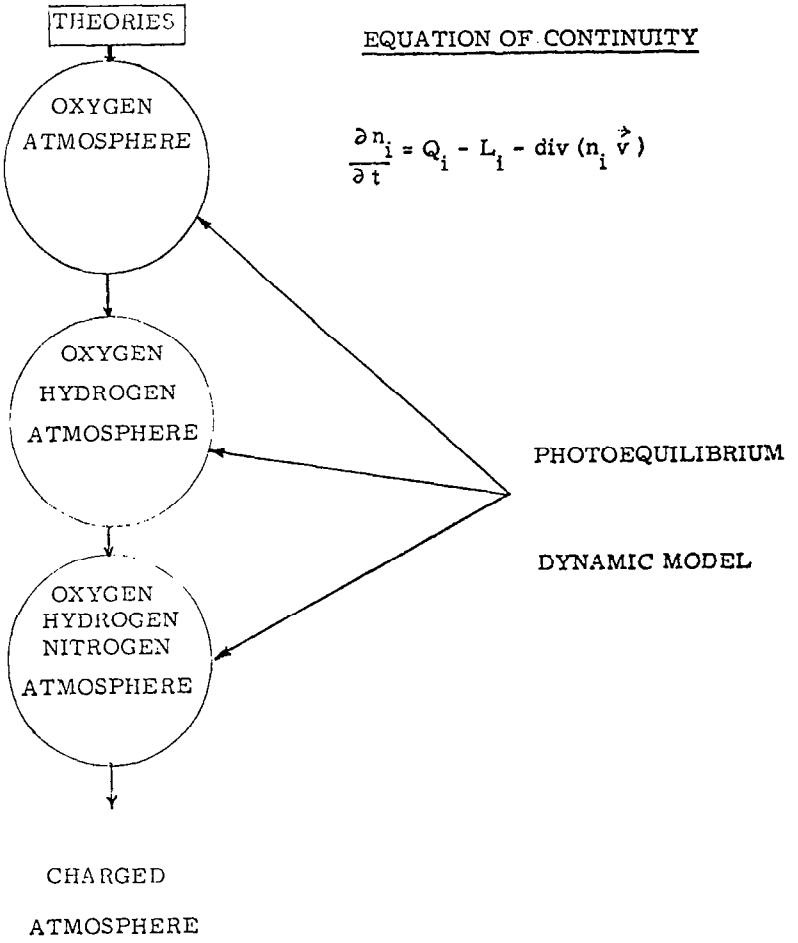

Fig. 3.8-13 Development Diagram of Ozone Theory

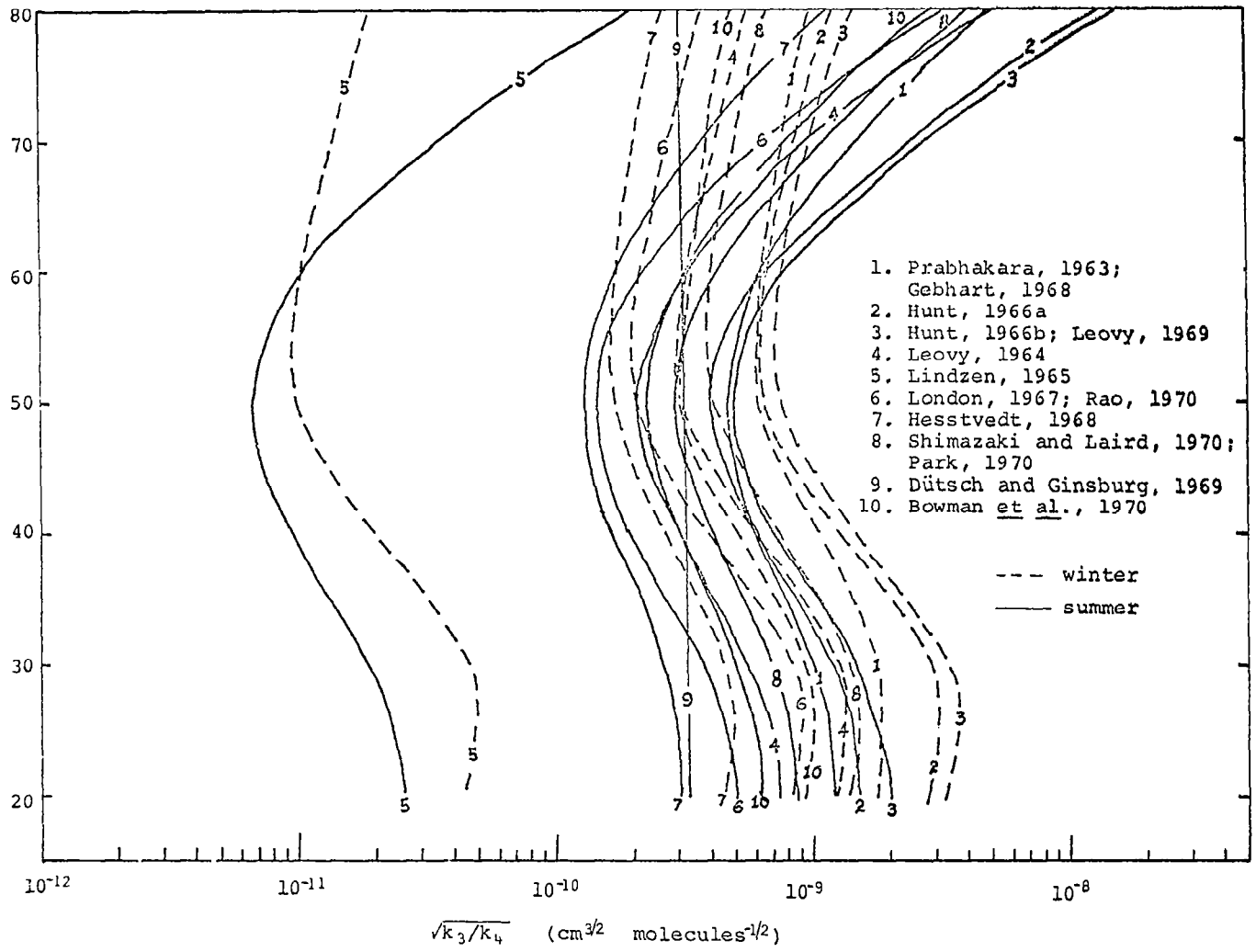

Fig. 3.8-14 Vertical profiles of $\sqrt{k_3/k_4}$ used by various authors. The CIRA temperature models were used.

References for Section 3.8

Bainbridge, A. E., and L. E. Heidt, 1966: Measurements of Methane in the Troposphere and Lower Stratosphere. Tellus XVIII, 221-224.

Bojkov, R. D., 1969: Ozone distribution over Mediterranean, Central, and Southeast Europe during the IQSY (1964-1965). Pure and App. Geophys., 74, 165-185.

Bowman, M. R., L. Thomas, and J. E. Geisler, 1970: The effect of diffusion process on the hydrogen and oxygen constituents in the mesosphere and lower thermosphere. J. Atmos. Terr. Phys., 32, 1661-1674.

Brewer, A. W., and J. R. Milford, 1960: The Oxford-Kew ozone sonde. Proc. Royal Soc., A, 256, 470-495.

Byron-Scott, R., 1967: A stratospheric general circulation experiment incorporating diabetic heating and ozone photochemistry. Publication in Meteor. No. 87, Dept. of Meteor., McGill Univ., Montreal, 201p.

Chapman, S., 1930: A theory of upper-atmospheric ozone. Mem. Roy., Meteor. Soc., 3, 103-125.

Craig, R. A., 1950: The observations and photochemistry of atmospheric ozone and their meteorological significance. Meteor. Monogr. 1, No. 2, 1-50.

Craig, R. A., 1965: The upper atmosphere, meteorology and physics, Chapter 5, International Geophysics Series, Vol. 8, Academic Press, N. Y. and London.

Crutzen, P. J., 1969: Determination of parameters appearing in "dry" and the "wet" photochemical theories for ozone in the stratosphere. Tellus, XXI. 3, 368-388.

Doherty, R. H., 1968: Importance of associative detachment and dissociative attachment in the lower ionosphere as shown by LF radio measurements. J. Geophys. Res., 73 (7), 2429-2440.

_____, 1970: Changes in D-region chemistry constituent with radio observation. J. Atmos. Terr. Phys., 32, 1511-1533.

Dütsch, H. U., 1968: The photochemistry of stratospheric ozone. Quart. J. R. Met. Soc., 94 (402), 483-497.

_____, 1969: Atmospheric ozone and ultraviolet radiation, "Climate of the Free Atmosphere," World Survey of Climatology, 4, 383-432, H. E. Landsber, ed. in chief, Elsevier Publ. Co., Amsterdam-London-N. Y.

Dutsch, H. U., and T. Ginsburg, 1969: Parametric studies of ozone photochemistry. Pure and Appl. Geophys., 72, 204-213.

Shimazaki, T., and A. R. Laird, 1970: A model calculation of the diurnal variation in minor neutral constituents in the mesosphere and lower thermosphere including transport effects. J. Geophys. Res., 75 (16), 797-799.

Vigroux, E., 1953: Contribution à l'étude experimentale de l'absorption de l'ozone. Ann. Phys. 8 (6), 709-762.

Wu, M. F., 1970a: A Review of Ozone Problems. Internal Report No. AER 1-1, July, 1970.

_____, 1970b: Ozone Distribution and Variability. Internal Report No. AER 1-2, August, 1970.

_____, 1970c: The Absorptions Coefficients of Ozone. Internal Report No. AER 1-3, October, 1970.

_____, 1970d: The Solar Spectrum from 2000 to 4000 Å. Internal Report No. AER 1-4, December, 1970.

_____, 1971: An Examination of Major Factors Relevant to Ozone Theory. Internal Report No. AER 1-5, April, 1971.

4.0 INTERNAL REPORTS

The MIT Aeronomy Program Internal Reports are listed below according to AER Number, Title and Author(s).

REPORT NO.	TITLE	AUTHOR(S)
AER 1-1	A Review of Ozone Problems	M. F. Wu
AER 1-2	Ozone Distribution and Variability	M. F. Wu
AER 1-3	The Absorptions Coefficients of Ozone	M. F. Wu
AER 1-4	The Solar Spectrum from 2000 to 4000 Å	M. F. Wu
AER 1-5	An Examination of Major Factors Relevant to Ozone Theory	M. F. Wu
AER 2-1	The Measurement of 5577 Å Radiation Profiles	D. M. Cunnold
AER 2-2	The Dayglow Spectrum	D. M. Cunnold
AER 2-3	Auroral Spectra	D. M. Cunnold
AER 2-4	The Deduction of Atomic Oxygen Concentrations from Measurements of 5577 Å and Herzberg Emission	D. M. Cunnold
AER 3-1	The Emission from the $^1\Delta_g$ State of O_2 and its Application as a Technique to Measure Ozone Concentration	D. M. Cunnold
AER 4-1	The Deduction of Temperature from Atmospheric Density Measurements	D. M. Cunnold
AER 4-2	Altitudinal, Locational, and Temporal Correlations of Neutral Atmospheric Density	T. P. McGarty P. C. Vernam
AER 6-1	On Laser Probing of Atmospheric Aerosols	J. E. Salah
AER 6-2	On the Nature and Distribution of Atmospheric Aerosols	J. E. Salah
AER 7-1	Standard Models of Atmospheric Constituents and Radiative Phenomena for Inversion Simulation	H. L. Malchow

AER 7-2	Pauli Algebraic Representations of Fields, Polarization States, and Radiative Transfer Phenomena	C. K. Whitney
AER 7-3	A Hybrid Algorithm for Computing Scattered Sunlight Horizon Profiles	R. E. Var
AER 7-4	Implications of a Quadratic Stream Definition in Radiative Transfer Theory	C. K. Whitney
AER 8-1	On the Constituent Density Inversion Problem—An MAP Estimator Approach	T. P. McGarty
AER 8-2	On the Star Occultation Inversion Problem—Perturbational and Recursive Estimator Structures	T. P. McGarty
AER 8-3	A MMSE Estimator for the Density Inversion Problem	T. P. McGarty
AER 8-4	An Inversion Procedure for a Photon Limited Environment—Star Occultation	T. P. McGarty
AER 8-5	A Simulation of Airglow Limb Measurement and Data Inversion	D. C. Merritt
AER 8-6	The Estimation of Constituent Density States by an Occultation Experiment—A Quasi-Exact Solution to the Kushner-Stratonovich Equation	T. P. McGarty K. L. Tompkins
AER 8-7	The Estimation of Atmospheric Constituent Densities Through the Inversion of Scattered Sunlight Measurements	D. C. Merritt
AER 8-8	The Estimation of Atmospheric Constituent Densities Through the Inversion of Stellar Occultation Measurements	D. C. Merritt
AER 9-1	The Effects of Spacecraft Motion and Position on the Accuracy of the Inversion Profiles	T. P. McGarty
AER 9-2	Constituent Detectivity of the Aeronomy Limb-Scanning Experiment	D. M. Cunnold C. R. Gray
AER 9-3	The Optical Altitude Resolution Obtainable with an f/8 Cassegrainian Telescope	C. R. Gray R. E. Var K. L. Tompkins
AER 10-1	Star Availability	P. C. Vernam
AER 10-2	Orbit Fraction	P. C. Vernam

AER 10-3	Data Management Requirements	C. R. Gray
AER 11-1	Nightglow and Star Profiles as Applied to the Star Occultation Problem	T. P. McGarty K. L. Tompkins
AER 11-2	The Application of a Linear Recursive Filter to Nadir Ultraviolet Inversion	D. C. Merritt
AER 11-3	MUSE Anomalies and Atmospheric Scattering Layer Computations	D. M. Cunnold
AER 12-1	Aeronomy Development Plan	C. R. Gray

Massachusetts Institute of Technology
77 Massachusetts Avenue
Cambridge, Massachusetts 02139